March 2019

DIRECT PATTERNING OF NATURE-INSPIRED SURFACES FOR BIOINTERFACIAL APPLICATIONS

Feyza Dundar

DIRECT PATTERNING OF NATURE-INSPIRED SURFACES FOR BIOINTERFACIAL APPLICATIONS

A Dissertation Presented

by

FEYZA DUNDAR

Submitted to the Graduate School of the
University of Massachusetts Amherst in partial fulfillment
of the requirements for the degree of

DOCTOR OF PHILOSOPHY

February 2019

Polymer Science and Engineering

DIRECT PATTERNING OF NATURE-INSPIRED SURFACES FOR BIOINTERFACIAL APPLICATIONS

A Dissertation Presented

by

FEYZA DUNDAR

Approved as to style and content by:

_____
James J. Watkins, Chair

_____
Samuel Gido, Member

_____
Jessica D. Schiffman, Member

_____
E. Bryan Coughlin, Department Head
Polymer Science and Engineering

DEDICATION

To my dear family.

ACKNOWLEDGMENTS

I would like to acknowledge numerous people that made this thesis possible. Thanks to my advisor Professor James J. Watkins. Thanks to his endless support, patience, guidance, and great mentorship. Thanks to him for giving great opportunities to grow me as a scientist and person. Thanks to my committee members Professor Jessica Shiffman and Professor Sam Gido for their support and guidance. I am grateful to Prof. Schiffman for the great collaboration and her insightful comments.

I would like to thank to past and present Watkins Group members, Dr. Rohit Kothari, Dr. Ying Lin, Dr. Yuying Tang, Irene Howell, Aditi Naik, Benjamin Yavitt, Yiliang Zhou, Wenhao Li for their insightful discussions and motivating me through my PhD. Especially I would like to thanks to Irene Howell and Aditi Naik for being great friends and helped me through all the struggles in the past couple of years.

Thanks to my collaborators, Dr. Kristopher W. Kolewe, Irene Kurtz, Dr. Ilja Czolkos, Dr. Alicia Johansson, Theodor Nielsen. Thanks to PSE class 2012. Thanks to PSE faculty and stuff. I would like to thank to John Berg for being a great mentor during my NSF I-Corps experience. I cannot express enough thanks to him for his support, vision, and guidance.

Thanks to my friends, especially Dr. Safia Ghaneim, Soeun Kim, Dr. Shruti Rattan, Tetsu Ouch, Irene Howell, Aditi Naik, Michael Leaf, Hyeyoung Kim, Laura Lanier, Dr. Piril Ertem, Dr. Vijesh Tanna, Benjamin Yavitt for making me feel surrounded with love, and making graduate school enjoyable.

Last but not the least I am grateful to my husband, mom, dad, sisters, parents-in-law, and grandparents for all their love and support. I owe my deepest gratitude to my

family for supporting me every way possible. Without their love and support this thesis would not be possible.

ABSTRACT

DIRECT IMPRINTING OF NATURE-INSPIRED SURFACES FOR BIOINTERFACIAL APPLICATIONS

FEBRUARY 2019

FEYZA DUNDAR

B.S., KOC UNIVERSITY

M.S., UNIVERSITY OF MASSACHUSETTS AMHERST

Ph.D., UNIVERSITY OF MASSACHUSETTS AMHERST

Directed by: Professor James J. Watkins

There are three major challenges for the design of patterned surfaces for biointerfacial applications: (i) durability of antibacterial/antifouling mechanisms, (ii) mechanical durability, and (iii) lifetime of the master mold for mass production of patterned surfaces. In this dissertation, we describe our contribution for the development of each of these challenges.

The bioinspired surface, Sharklet AF™, has been shown to reduce bacterial attachment via a biocide-free structure-property relationship effectively. Unfortunately, the effectiveness of polymer-based sharkskin surfaces is challenged over the long term by both eventual bacteria accumulation and a lack of mechanical durability. To address these common modes of failure, hard, multifunctional, antifouling, and antibacterial shark-skin patterned surfaces were fabricated via a solvent-assisted imprint patterning technique. A UV-crosslinkable adhesive material was loaded with titanium dioxide (TiO_2) nanoparticles (NPs) from which shark skin microstructures were imprinted on a polyethylene terephthalate substrate. Furthermore, hard, multifunctional, antifouling, and antibacterial shark skin patterned surfaces were fabricated using inks comprised of zirconium dioxide

(ZrO_2) NPs and TiO_2 NPs. The ZrO_2 NPs provide an extremely hard and durable matrix in the final structure, while the TiO_2 NPs provide active antibacterial functionality in the presence of UV light via photooxidation. The dynamic water contact angle, mechanical, antibacterial, and antifouling characteristics of the shark skin patterned surfaces were investigated as a function of TiO_2 content. We then demonstrated the multifunctional shark skin system's suitability for use as an antifouling biosensor.

Lastly, we described the design of a durable, hard master mold for pattern transfer. The lifetime of many of the current molds is limited by a lack of mechanical durability as well as cost. In this study, ZrO_2 NPs were imprinted on a variety of substrates using a solvent-assisted patterning technique and subsequently annealed to increase the mechanical durability of the mold. Polymer replications were demonstrated using the hard ZrO_2 mold with thermal and UV nanoimprinting lithography techniques, and injection molding. After up to 115,000 injection molding cycles, there was no delamination or breakage in the ZrO_2 mold. The high hardness and durability, as demonstrated through the many replication cycles, suggests that the ZrO_2 mold has excellent potential for use in the mass production of patterned polymer replicas. We also explored the nanopatterning of stainless steel using the ZrO_2 mold. The solution-processability and simple patterning technique of ZrO_2 NPs enable large-area and cost-effective fabrication of the hard molds which can be used for the variety of nano and micro-replication technologies.

TABLE OF CONTENTS

Page

ACKNOWLEDGMENTS v

ABSTRACT vii

LIST OF TABLES xii

LIST OF FIGURES xiii

CHAPTER

1. INTRODUCTION 1

    1.1 Overview of Antifouling and Antibacterial Surfaces 1
    1.2 Overview of Patterning Techniques 4
    1.3 Materials of Interest 6
    1.4 References 7

2. BIOINSPIRED PHOTOCATALYTIC SHARK-SKIN SURFACES WITH ANTIBACTERIAL AND ANTIFOULING ACTIVITY VIA NANOIMPRINT LITHOGRAPHY 11

    2.1 Introduction 11
    2.2 Experimental Section 13

        2.2.1 Materials 13
        2.2.2 Solvent Exchange of TiO_2 Nanoparticle (NP) Dispersion 14
        2.2.3 PDMS Mold Fabrication 14
        2.2.4 Shark Skin Pattern Fabrication Using Solvent-Assisted NIL 15
        2.2.5 Materials Characterization 16
        2.2.6 Antifouling Performance 17
        2.2.7 Antibacterial Activity 18

    2.3 Results and Discussion 18

        2.3.1 Polymer and Ceramic Composite Shark Skin Pattern Fabrication 18
        2.3.2 Characterization of the Composites 22
        2.3.3 Characterization of Shark Skin Patterned Surfaces 25
        2.3.4 Antifouling Activity of Shark Skin Patterned Surfaces 28
        2.3.5 Antibacterial Activity of TiO_2 NP Composites 31

    2.4 Conclusions 33
    2.5 References 33

3. DIRECT PATTERNING OF BIOINSPIRED, PHOTOCATALYTIC, DURABLE, CERAMIC SURFACES WITH ANTIFOULING AND ANTIBACTERIAL ACTIVITY 39

3.1 Introduction 39
3.2 Experimental section 41

3.2.1 Materials 41
3.2.2 Methods 42
3.2.3 Characterization and Evolution of Shark Skin Microstructures 43

3.3 Results and Discussion 45

3.3.1 Fabrication of ZrO_2/TiO_2 Shark Skin Patterned Surfaces 45
3.3.2 Antifouling and Antibacterial Activity 51
3.3.3 Parylene HT-Coated Shark-Skin-Patterned Surfaces 53

3.4 Conclusions 55
3.5 References 55

4. NANOCERIA-BASED SHARK-SKIN PATTERNS WITH BIOSENSING AND ANTIFOULING ACTIVITIES 60

4.1 Introduction 60
4.2 Experimental Section 62

4.2.1 Materials 62
4.2.2 Methods 63
4.2.3 Characterization 64

4.3 Results and Discussion 66

4.3.1 CeO_2 Shark-Skin and p(HEMA-co-EGDA) Coating 66
4.3.2 Electrochemical Activities 68
4.3.3 Antifouling Activities 71

4.4 Conclusions 73
4.5 References 73

5. LOW-COST, DURABLE MASTER MOLDS FOR THERMAL-NIL, UV-NIL, AND INJECTION MOLDING 77

5.1 Introduction 77
5.2 Experimental Section 79

5.2.1 Materials 79
5.2.2 Methods 80
5.2.3 Characterization of ZrO_2 Dispersion, Mold and Polymer Replicas 82

5.3 Results and Discussion 83

5.3.1 Fabrication of the ZrO_2 Master Mold 83
5.3.2 Thermal Imprint using ZrO_2 Mold 87
5.3.3 UV-NIL using ZrO_2 Mold 93
5.3.4 Injection Molding using ZrO_2 Mold 96

5.4 Conclusions 98
5.5 References 99

6. NANOPATTERNING OF STEEL VIA HARD ZIRCONIA MOLD 102

6.1 Introduction 102
6.2 Experimental Section 104

6.2.1 Materials 104
6.2.2 Methods 105
6.2.3 Characterization 106

6.3 Results and Discussion 106
6.4 Conclusions 112
6.5 References 112

7. INNOVATION CORPS PROJECT 115

7.1 Project Aim 115
7.2 Major Activities and Results 115

8. FUTURE WORK 120

BIBLIOGRAPHY 122

LIST OF TABLES

Table **Page**

2.1. Nanomechanical analysis of composite materials. 25

3.1. Wetting analysis of ZrO_2/TiO_2 smooth and shark-skin-patterned surfaces 50

5.1. Nanomechanical analysis of ZrO_2 as a function of annealed temperature. 86

LIST OF FIGURES

Figure **Page**

1.1. Scheme of the reaction mechanism of a TiO_2 photocatalyst upon light exposure..... 6

2.1. Schematic representation of the fabrication process of shark skin patterns using a PDMS soft stamp on flexible PET substrates. 20

2.2. Optical profilometry images and dimensions 21

2.3. TGA of NOA, TiO_2-10, TiO_2-50, and TiO_2-C..... 22

2.4. TEM images of low and high magnifications..... 24

2.5. SEM images and dimensions of shark skin patterns with different composites..... 26

2.6. (a, b) Digital photos of NOA, TiO_2-10, TiO_2-50, and TiO_2-C shark skin patterns 26

2.7. SEM micrographs of NOA* (100% NOA) shark skin surfaces 27

2.8. Water contact angle analysis of shark skin patterned surfaces. 28

2.9. The 24 h area coverage of surface-adhered E. coli on smooth films (S) versus patterned surfaces (P) of NOA, TiO_2-10, TiO_2-50, and TiO_2-C..... 29

2.10. The total area coverage of surface-adhered E. coli on smooth (S) and patterned (P) NOA surfaces, as well as on PET controls. 30

2.11. Fluorescent micrographs show that E. coli adhered between the patterned features..... 31

2.12. Loss of (a) E. coli and (b) S. aureus viability after 1 h of UV exposure to planar TiO_2-10, TiO_2-50, and TiO_2-C films. 32

3.2. (a) Schematic representation of the fabrication process of ZrO2/TiO2 shark-skin-patterns using soft PDMS stamp, SEM micrographs of ZrO2/TiO2 shark-skin-patterned surfaces 47

3.3. Optical profilometry images and height profile of (a) the ZrO_2/TiO_2 before annealing and (b) the ZrO_2/TiO_2 after annealing, (c) Parylene HT coated ZrO_2/TiO_2. 48

3.4. Nanoindentation analysis of PDMS[37], ZrO2/TiO2 film before and after annealing at 300°C, 500°C, 750°C, and 1000°C. 49

3.5. Representative micrographs of E. coli attached to after a 24 hr incubation period on a flat ZrO2/TiO2 surface (ZrO2 S), shark skin patterned ZrO2/TiO2 surfaces (ZrO2 P)..... 52

3.6. Loss of E. coli viability after 1 hr UV-exposure to films containing TiO_2..... 52

3.7. SEM micrographs of Parylene HT coated ZrO_2/TiO_2 shark-skin-patterned surfaces (a) top view, (b) cross section, (c) Representative micrographs of *E. coli* attached to after a 24 hr incubation period on a smooth Parylene HT coated ZrO_2/TiO_2 surface (S), Parylene HT coated shark-skin-patterned ZrO_2/TiO_2 surfaces (P). 54

4.1. Schematic representation of the fabrication process of shark skin patterns using a PDMS soft stamp on gold coated Si wafers..... 67

4.2. (a) DLS measurement of CeO_2 NP size distribution, digital image of the CeO_2 ink. SEM micrographs of (b) cross-section of CeO_2 shark-skin-patterned surface, (c) p(HEMA-co-EGDA) coated CeO_2 shark-skin-patterned surface, (d) cross-section of 50 nm p(HEMA-co-EGDA) coating on CeO_2 shark-skin-patterned surface. 68

4.3. (a) CV of CeO_2 shark-skin biosensor before and after addition of 1mM H_2O_2 in PBS (pH:7.4). (b) chronoamperometric response of continuous addition of 1mM H_2O_2 in PBS (pH:7.4) at -0.4V. (c) amperometric response as a function of H_2O_2 concentration. (d) with addition of interfering species (ascorbic acid (AA) and uric acid (UA)) and H_2O_2. 70

4.4. In-situ antifouling test for 1 h. CV of (a) CeO_2 shark-skin electrode, (b) P(HEMA-co-EGDA) coated CeO_2 shark-skin electrode in 2.5 mg/ml BSA in $Fe(CN_6)^{4-/3-}$..... 71

4.5. The 24 h area coverage of surface-adhered E. coli on p(HEMA-co-EGDA) coated CeO2 smooth films versus shark-skin-patterned surfaces. 72

5.1. Schematic representation of patterning the hard ZrO_2 master mold and subsequent pattern transfer using the ZrO_2 mold. 84

5.2. (a) TEM image of ZrO_2 NPs (drop casted from diluted ZrO_2 dispersion). (b) DLS measurement of ZrO_2 nanoparticles size distribution, digital image of the ZrO_2 ink. (c) TGA of ZrO_2 nanoparticles. 85

5.3. SEM micrographs of sintered ZrO_2 films at 300°C, 500°C, 750°C, and 1000°C for 2h under air. 87

5.4. Images of (a) Si master mold. (b) ZrO_2 mold on a Si wafer. (c) PMMA inverse structures of the ZrO_2 master on a PET substrate. 88

5.5. SEM micrographs of (a) imprinted ZrO_2 line pattern (width: 500 nm, pitch: 1300 nm), (b) PMMA replica of the ZrO_2 line pattern, (c) imprinted ZrO_2 hole pattern,

(d) PMMA replica of the ZrO_2 hole pattern. Thermal-NIL was conducted to obtain PMMA replicas. 88

5.6. (a) Height profile of the ZrO_2 mold. SEM micrographs of (b) patterned ZrO_2 nanoparticles on Si wafer using solvent-assisted soft NIL, 45° tilted, (c) top view, (d) inverse PMMA structures using hard ZrO_2 mold via thermal NIL. (e) The same ZrO_2 mold after 15 consecutive imprints. (f) Inverse PMMA structures as the 15^{th} replica. (g) The same ZrO_2 mold after 30 consecutive imprints. (g) Inverse PMMA structures as the 30^{th} replica. 89

5.7. SEM images of (a) patterned ZrO_2 NPs on steel using solvent-assisted soft NIL, (b) higher magnification with 45^o tilt, (c) inverse PMMA structures using hard ZrO_2 mold via thermal NIL, and (d) higher magnification. (f) Digital photos of ZrO_2 imprint on a curved watch glass (e) Digital photo of ZrO_2 master mold on Kapton film. SEM images of (g) patterned metal oxide nanoparticles on Kapton film, (h) and inverse PMMA structures using hard metal oxide mold via thermal NIL. 91

5.8. Surface profile images of (a) a bare steel surface. (b) After 1st coating layer on the steel. (c) After 2nd coating layer on the steel. (d) After 3rd coating layer on the steel. (e) After 4th coating layer on the steel. 92

5.9. (a) Digital photo and optical profile of nanopatterned ZrO_2 on a rough steel substrate. (b) Roughness versus the number of planarizing coatings. (c) Digital photo and optical profile of nanopatterned ZrO_2 on the planarized steel substrate, and (d) A digital photo of nanopatterned ZrO_2 and polymer replica and optical profile of the polymer replica. 92

5.10. (a) SEM image of ZrO_2 shark-skin on glass using solvent-assisted soft NIL and a digital photo of ZrO_2 shark-skin mold on glass (b) SEM image of inverse NOA structures using hard ZrO_2 shark-skin mold via UV-NIL. 94

5.11. SEM micrographs of variety patterned nano/microstructures using ZrO_2 dispersion. 95

5.12. SEM micrographs of various aspect ratio structures (2:1, 4:1, and 6:1). Imprinted ZrO2 shark-skin, line pattern, and high aspect ratio pillars and corresponding NOA replicas of the ZrO2 shark-skin, line pattern, and high aspect ratio pillars 96

5.13. (a) Digital photo of patterned ZrO_2 nanoparticles on a steel block using solvent-assisted soft NIL. SEM micrographs of patterned ZrO_2 nanoparticles on a steel block (b) before injection molding (c) after 114,965 injection molding cycles. Digital photos and optical micrographs of nanopatterned polymer replicas (d) after 28,751 cycles, (e) after 50,990 cycles, (f) after 87,380 cycles, and (g) after 114,965 cycles. 97

5.14. AFM height profile of (a) ZrO_2 patterned steel insert, (b) a molded ABS polymer. The height was determined to be ~170 nm for both ZrO_2 mold and replicated polymer. 98

6.1. Schematic representation of the fabrication process of (a) ZrO_2 patterned mold using soft PDMS stamp, (b) patterned steel using the hard ZrO_2 patterned mold. 107

6.2. Digital images of (a) ZrO_2 patterned mold, (b) steel patterned surface, (c) subsequent patterning of the steels using the single ZrO_2 patterned mold. 108

6.3. SEM micrographs, optical and height profilometry of the (a,b) ZrO_2 patterned mold, (c.d) patterned steel substrates using the ZrO_2 mold. 109

6.4. SEM micrographs of patterned steel surfaces from different spots (a,c) low mag, (b.d) high mag. 109

6.5. Optical profilometry of the patterned steel surfaces using a single ZrO_2 patterned mold. (a) The first patterned steel, SS304-1, (b) The third patterned steel, SS304-3 110

6.6. Comparison of steel sheet thicknesses under the same pressing conditions. Height profiles of steel surfaces (a) patterned SS304, (b) patterned SUS 304. 111

6.7. Load versus displacement curves of (a) SS304 under rate control (200 μN/s), (b) SS304 versus SUS304. 111

CHAPTER 1

INTRODUCTION

1.1 Overview of Antifouling and Antibacterial Surfaces

Bacteria, which make up the oldest fossils are known, have existed for more than 3.5 million years. Although some bacteria are essential for the ecosystem, harmful bacteria often cause severe complications in health-care, food processing, and in many other industries.[1] Unfortunately, bacterial contamination causes millions of infections and 23,000 deaths every year in the US alone. Once bacteria attach to a surface, colony formation subsequently follows, which ultimately results in biofilm formation. Bacteria and biofilms are very complex systems and often are not trivial to deal with.[2] There are two major approaches to designing antimicrobial surfaces: antifouling and antibacterial. Antifouling refers to a system that prevents an organism from attaching to a surface, whereas, the term antibacterial often refers to a biocidal surface that kills bacteria upon contact of via leaching chemicals.

Antibacterial agents, including silver (Ag), copper (Cu), photocatalytic titanium dioxide (TiO_2), and zinc oxide (ZnO) have been shown to be bactericidal. The antibacterial characteristics of these materials result from several mechanisms including toxic ions, electrostatic forces, and the generation of reactive oxygen species.[3,4] For example, Ag NPs release Ag^+ ions, which can inactivate a broad-spectrum of bacteria from gram-positive to gram-negative by damaging the bacterial cell membrane. Moreover, antimicrobial peptides[5], antimicrobial enzymes[6] and various antibiotics have exhibited contact-based killing activities. However, antibacterial agents/surfaces often suffer from limited antimicrobial durability and stability due to the complete leaching of active chemicals

and/or as a result of the accumulation of dead bacteria.[7] Furthermore, antibacterial agents often cause more resistant bacteria.[8]

Antifouling surfaces may prevent or resist fouling through several mechanisms including chemistry, topography, and the mechanics of the surface, all of which cause non-favorable interactions between the bacterial cell and the substrate.[9–11] For example, poly(ethylene glycol) (PEG) is one of the gold-standards of coatings which resists protein adsorption as a result of low water interfacial energy (less than 5 $mJ.m^{-2}$).[12] The common properties of protein-adsorption-resistant surfaces are reported as being polar, hydrogen-bond acceptors electrically neutral, and having no hydrogen-bond donors,.[13,14] Moreover, increasing polymer grafting density and chain length also enhances the antifouling properties.[15,16] Bacterial attachment on a substrate is facilitated through an adsorbed protein layer, and therefore surfaces that resist protein adsorption often resist bacterial attachment. However, although PEG displays excellent protein resistance, it often fails in reducing bacterial colonization.[17] Zwitterionic polymers have been demonstrated as alternative materials for non-fouling surfaces due to their enhanced mechanical and chemical stability compared to PEGs. Their non-fouling behavior is explained with the presence of a water layer, which delays the adsorption of proteins and therefore the adhesion of bacteria.[18] However, no such surface has been able to prevent 100% of bacterial attachment. This can be partially attributed to the lack of sufficient mechanical and antimicrobial durability of the current coatings, which prevents antifouling characteristics over sustained periods of time.

Nature-inspired coatings[19,20], based on microtopography, have caught the attention of researchers for their potential to overcome current antimicrobial challenges. Some marine

mammals and fast swimming fishes have distinct topographies on their skin, which result in a non-fouling property.[21] Sharks are one of the most widely studied animals because of their non-fouling skin. For example, shark-skin inspired surfaces have been used in drag reduction, which results from alignment of the longitudinal grooves parallel to the flow direction.[19] It has been reported that shark-skin texture on a commercial aircraft reduced fuel consumption by up to 2% by reducing the drag by up to 8%.[22] Rough topographies exhibiting antifouling characteristics via structure-property relationships often revealed that patterned surfaces have significantly reduced bacterial attachment compared to smooth films of the same material. It has been found that feature size and pattern design are critical factors affecting antifouling behavior. For example, one of the commercialized antifouling microtopographic designs, Sharklet, is inspired by shark-skin and has been shown to inhibit the attachment of a variety of microorganism including *Ulva*, *Escherichia coli (E. coli)*, *Staphylococcus aureus (S. aureus),* and platelet cells up to 70-85% after a 24 h incubation period. However, none of the reported microtopographies is a long-term antifouling solution due to certain intrinsic characteristics such as mechanical and antimicrobial durability. When given sufficient amount of time, biofilms still form. Thus, further development and understanding of advanced antibacterial and antifouling surfaces are needed to obtain new high-performance, durable coatings.

In this thesis, we describe the design of multifunctional shark-skin-patterned surfaces with antifouling and antibacterial activities. Moreover, we discuss the development of advanced biosensors which take advantage of the antifouling characteristics of the multifunctional shark-skin surface. Challenges and needs persisting in the field are explained in more detail in the following chapters.

1.2 Overview of Patterning Techniques

Nano/micro topographies can be fabricated via various techniques[23] including photolithography, ion-beam lithography, e-beam lithography, nanoimprint lithography (NIL)[24], and dip-pen nanolithography[25]. Among the many patterning techniques, NIL stands out as a low-cost, scalable method that lends itself well to the mass production of new high-performance materials. NIL can be divided into many sub-groups, but thermal-NIL and UV-NIL are the most common replication techniques. The general process chain of NIL starts with fabrication of a silicon (Si) master mold via e-beam lithography. Then, the Si master mold is replicated into a soft or hard working stamp. Then, the working stamp is used to replicate many nano/micro patterns into the desired polymer material. The polymer material is shaped into the desired pattern in its viscous state. Thermoplastic polymer films can be patterned at above their glass transition temperature (Tg) within several minutes using a hard stamp. Thermal-NIL often suffers from incomplete-replication, long cycle times, and short stamp lifetimes. In UV-NIL, low viscosity monomers fill the working stamp via capillary action and are rigidified through crosslinking under a UV light.. Thus, better replication quality is enabled, along with a shorter cycle time. Thermal and UV-NIL are capable of patterning not only polymers, but also inorganic sol-gels, which gives them material versatility. The scalability of NIL techniques is evident in that roll-to-roll (R2R) thermal-NIL and R2R UV-NIL have been developed for large-scale applications. Alternatively, injection molding enables the fabrication of nano/micropatterned surfaces for mass production of 3-dimensional objects. For example, compact disks (CDs) and micro-optical components (smartphone cameras) have been developed based on injection molding of micro/nanopatterns.

Nanoimprinting and injection molding techniques have two main challenges which limits the use of patterned surfaces in practical applications. First, the lifetime of a single working stamp is not sufficient to produce the millions of replicas that are required for cost-efficiency. Second, fabrication of seamless patterned surfaces over large areas is limited. In this thesis, we will address on the development of durable working stamps.

In our group, we have developed a solvent-assisted NP imprinting technique, which enables direct imprinting of crystalline NPs and offers practical solutions for battery[26,27], in optics[26,28] and, antimicrobial[29] applications. The advantage of the imprinting of NPs over sol-gels is less shrinkage, which leads stable, crack-free nano/micropatterns. The process is briefly as follows: a NP dispersion is coated on a substrate, a soft poly(dimethylsiloxane) (PDMS) is placed onto the coating, and then NPs fill the stamp via capillary action. The advantages of using PDMS as the working stamp material consist of: (i) conformal contact with planar and nonplanar surfaces, (ii) solvent absorption, (iii) low surface energy which allows easy demolding. Additionally, the formulation of the NP dispersion is essential to obtain high fidelity replicated features. Typically, we select a combination of low and high volatility solvents in which the highly volatile solvent allows fast film formation and the low volatility solvent enables the capillary action and filling of the PDMS inverse stamp. Moreover, solvent compatibility to the PDMS, surface tension of the solvents, and the viscosity of the NP dispersion are important factors that affect imprinting quality. For example, the high surface tension of water and the limited absorption of water by PDMS makes it challenging to imprint water-based NP dispersions. Thus, we imprint the patterns using organic solvents or conduct a solvent exchange of NPs from aqueous-based to organic solvents.

1.3 Materials of Interest

1.3.1 Titanium Dioxide (TiO_2) Nanoparticles

TiO_2 is an excellent photocatalyst, which has been used to decompose organic compounds under illumination. In 1921, Renz reported for the first time that under sunlight illumination, TiO_2 is reduced in the presence of organic compounds and that the TiO_2 turned from white to grey and blue.[30] Later, the photoelectrolysis of water by TiO_2 was reported in 1972.[31] The photocatalytic mechanism of TiO_2 is shown in **Figure 1.1**. Under illumination, upon adsorption of photons, electrons are excited from the valence band to the conduction band, leaving a hole in the valence band. In the presence of water, reactive oxygen species (ROS) are formed. There are three main phases of TiO_2; anatase, rutile, and brookite. The anatase phase has been shown to be the most effective photocatalyst, with a band gap of approximately 3.2 eV, which can be activated under illumination at a wavelength below 385 nm. TiO_2 has been widely used in many applications including water purification, air cleaning, disinfection and self-cleaning.[32]

$$TiO_2 + h\nu \rightarrow e_{cb}^- + h_{vb}^+ \quad (1.1)$$

$$O_2 + e_{cb}^- \rightarrow O_2^-\cdot \quad (1.2)$$

$$h_{vb}^+ + H_2O \rightarrow \cdot OH + H^+ \quad (1.3)$$

$$\cdot OH + \cdot OH \rightarrow H_2O_2 \quad (1.4)$$

$$O_2^-\cdot + H_2O_2 \rightarrow \cdot OH + OH^- + O_2 \quad (1.5)$$

$$O_2^-\cdot + H^+ \rightarrow \cdot OOH \quad (1.6)$$

Figure 1.1. Scheme of the reaction mechanism of a TiO_2 photocatalyst upon light exposure.[33]

Matsunaga et al. first demonstrated antimicrobial activity of TiO_2 in 1985.[34] Since then it has been reported that TiO_2 can be used to inactivate bacteria, fungi, algae, and viruses under a weak UVA illumination. The killing mechanism of TiO_2 toward bacteria has been studied and it has been reported that the lethal action of ROS results in bacterial membrane and cell wall damage, ultimately resulting in the death of the bacteria. Several great references on the photocatalytic killing activity of TiO_2 have been provided by Foster and Fu et al.[33,35]

In this thesis, we describe a multifunctional surface that combines topographical antifouling properties with the photocatalytic advantages of TiO_2 NPs to obtain antibacterial functionality and long-term durability.

1.4 References

(1) Costerton, J. W.; Stewart, P. S.; Greenberg, E. P. Bacterial Biofilms: A Common Cause of Persistent Infections. *Sci.* **1999**, *284* (5418), 1318–1322.

(2) Dang, H.; Lovell, C. R. Microbial Surface Colonization and Biofilm Development in Marine Environments. **2016**, *80* (1), 91–138.

(3) Parashar, U. K.; Kumar, V.; Bera, T.; Saxena, P. S.; Nath, G.; Srivastava, S. K.; Giri, R.; Srivastava, A. Study of Mechanism of Enhanced Antibacterial Activity by Green Synthesis of Silver Nanoparticles. *Nanotechnology* **2011**, *22* (41).

(4) Hasan, J.; Crawford, R. J.; Ivanova, E. P. Antibacterial Surfaces: The Quest for a New Generation of Biomaterials. *Trends Biotechnol.* **2013**, *31* (5), 295–304.

(5) Onaizi, S. A.; Leong, S. S. J. Tethering Antimicrobial Peptides: Current Status and Potential Challenges. *Biotechnol. Adv.* **2011**, *29* (1), 67–74.

(6) Thallinger, B.; Prasetyo, E. N.; Nyanhongo, G. S.; Guebitz, G. M. Antimicrobial Enzymes: An Emerging Strategy to Fight Microbes and Microbial Biofilms. *Biotechnol. J.* **2013**, *8* (1), 97–109.

(7) Yu, Q.; Wu, Z.; Chen, H. Dual-Function Antibacterial Surfaces for Biomedical Applications. *Acta Biomater.* **2015**, *16* (1), 1–13.

(8) Stewart, P. S.; Costerton, J. W. Antibiotic Resistance of Bacteria in Biofilms. *Lancet*

2001, *358* (9276), 135–138.

(9) Lichter, J. A.; Thompson, M. T.; Delgadillo, M.; Nishikawa, T.; Rubner, M. F.; Van Vliet, K. J. Substrata Mechanical Stiffness Can Regulate Adhesion of Viable Bacteria. *Biomacromolecules* **2008**, *9* (6), 1571–1578.

(10) Song, F.; Koo, H.; Ren, D. Effects of Material Properties on Bacterial Adhesion and Biofilm Formation. *J Dent Res* **2015**, *94* (8), 1027–1034.

(11) Banerjee, I.; Pangule, R. C.; Kane, R. S. Antifouling Coatings: Recent Developments in the Design of Surfaces That Prevent Fouling by Proteins, Bacteria, and Marine Organisms. *Adv. Mater.* **2011**, *23* (6), 690–718.

(12) Krishnan, S.; Weinman, C. J.; Ober, C. K. Advances in Polymers for Anti-Biofouling Surfaces. *J. Mater. Chem.* **2008**, *18* (29), 3405–3413.

(13) Ostuni, E.; Chapman, R. G.; Holmlin, R. E.; Takayama, S.; Whitesides, G. M. A Survey of Structure - Property Relationships of Surfaces That Resist the Adsorption of Protein. **2001**, *17* (9), 5605–5620.

(14) Rodriguez-Emmenegger, C.; Brynda, E.; Riedel, T.; Houska, M.; Šubr, V.; Alles, A. B.; Hasan, E.; Gautrot, J. E.; Huck, W. T. S. Polymer Brushes Showing Non-Fouling in Blood Plasma Challenge the Currently Accepted Design of Protein Resistant Surfaces. *Macromol. Rapid Commun.* **2011**, *32* (13), 952–957.

(15) Li, L.; Chen, S.; Zheng, J.; Ratner, B. D.; Jiang, S. Protein Adsorption on Oligo(Ethylene Glycol)-Terminated Alkanethiolate Self-Assembled Monolayers: The Molecular Basis for Nonfouling Behavior. *J. Phys. Chem. B* **2005**, *109* (7), 2934–2941.

(16) Castner, D. G.; Ratner, B. D. *Biomedical Surface Science: Foundations to Frontiers*; 2002; Vol. 500.

(17) Ostuni, E.; Chapman, R. G.; Liang, M. N.; Meluleni, G.; Pier, G.; Ingber, D. E.; Whitesides, G. M. Self-Assembled Monolayers That Resist the Adsorption of Proteins and the Adhesion of Bacterial and Mammalian Cells. *Langmuir* **2001**, *17* (20), 6336–6343.

(18) Sae-Ung, P.; Kolewe, K. W.; Bai, Y.; Rice, E. W.; Schiffman, J. D.; Emrick, T.; Hoven, V. P. Antifouling Stripes Prepared from Clickable Zwitterionic Copolymers. *Langmuir* **2017**, *33* (28), 7028–7035.

(19) Bhushan, B. Biomimetics: Lessons from Nature--an Overview. *Philos. Trans. A. Math. Phys. Eng. Sci.* **2009**, *367* (1893), 1445–1486.

(20) Liu, K.; Jiang, L. Bio-Inspired Self-Cleaning Surfaces. *Annu. Rev. Mater. Res.* **2012**, *42* (1), 231–263.

(21) Zhao, N.; Wang, Z.; Cai, C.; Shen, H.; Liang, F.; Wang, D.; Wang, C.; Zhu, T.; Guo, J.; Wang, Y.; Liu, X.; Duan, C.; Wang, H.; Mao, Y.; Jia, X.; Dong, H.; Zhang, X.;

Xu, J. Bioinspired Materials: From Low to High Dimensional Structure. *Adv. Mater.* **2014**, *26* (41), 6994–7017.

(22) Ball, P. Shark Skin and Other Solutions. *Nat. Eng.* **1999**, *400* (6744), 507–508.

(23) Gates, B. D.; Xu, Q.; Stewart, M.; Ryan, D.; Willson, C. G.; Whitesides, G. M. New Approaches to Nanofabrication: Molding, Printing, and Other Techniques. *Chem. Rev.* **2005**, *105* (4), 1171–1196.

(24) Chou, S. Y.; Krauss, P. R.; Renstrom, P. J. Imprint of Sub-25 Nm Vias and Trenches in Polymers. *Appl. Phys. Lett.* **1995**, *67* (1995), 3114.

(25) Piner, R. D.; Zhu, J.; Xu, F.; Hong, S.; Mirkin, C. A. "Dip-Pen" Nanolithography. *Science (80-.).* **1999**, *283* (5402), 661–663.

(26) Li, W.; Zhou, Y.; Howell, I. R.; Gai, Y.; Naik, A. R.; Li, S.; Carter, K. R.; Watkins, J. J. Direct Imprinting of Scalable , High-Performance Woodpile Electrodes for Three-Dimensional Lithium-Ion Nanobatteries. *ACS Appl. Mater. Interfaces* **2018**, *10* (6), 5447–5454.

(27) Li, W.; Christiansen, T. L.; Li, C.; Zhou, Y.; Fei, H.; Mamakhel, A.; Iversen, B. B.; Watkins, J. J. High-Power Lithium-Ion Microbatteries from Imprinted 3D Electrodes of Sub-10 Nm LiMn2O4/Li4Ti5O12 Nanocrystals and a Copolymer Gel Electrolyte. *Nano Energy* **2018**, 52, 431–440.

(28) Howell, I. R.; Giroire, B.; Garcia, A.; Li, S.; Aymonier, C.; Watkins, J. J. Fabrication of Plasmonic TiN Nanostructures by Nitridation of Nanoimprinted TiO2 Nanoparticles. *J. Mater. Chem. C* **2018**, *6* (6), 1399–1406.

(29) Arisoy, F. D.; Kolewe, K. W.; Homyak, B.; Kurtz, I. S.; Schiffman, J. D.; Watkins, J. J. Bioinspired Photocatalytic Shark-Skin Surfaces with Antibacterial and Antifouling Activity via Nanoimprint Lithography. *Appl. Mater. Interfaces* **2018**, 10 (23), 20055–20063.

(30) Fujishima, A.; Zhang, X.; Tryk, D. A. TiO2 Photocatalysis and Related Surface Phenomena. *Surf. Sci. Rep.* **2008**, *63* (12), 515–582.

(31) Fujishima, A.; Honda, K. Electrochemical Photolysis of Water at a Semiconductor Electrode. *Nature* **1972**, *238* (5358), 37–38.

(32) Carp, O.; Huisman, C. L.; Reller, A. Photoinduced Reactivity of Titanium Dioxide. *Prog. Solid State Chem.* **2004**, *32* (1–2), 33–177.

(33) Foster, H. a.; Ditta, I. B.; Varghese, S.; Steele, A. Photocatalytic Disinfection Using Titanium Dioxide: Spectrum and Mechanism of Antimicrobial Activity. *Appl. Microbiol. Biotechnol.* **2011**, *90* (6), 1847–1868.

(34) Matsunaga, T.; Tomoda, R.; Nakajima, T.; Wake, H. Photoelectrochemical Sterilization of Microbial Cells by Semiconductor Powders. *FEMS Microbiol. Lett.* **1985**, *29* (1–2), 211–214.

(35) Fu, G.; Vary, P. S.; Lin, C.-T. Anatase TiO2 Nanocomposites for Antimicrobial Coatings. *J. Phys. Chem. B* **2005**, *109* (18), 8889–8898.

CHAPTER 2

BIOINSPIRED PHOTOCATALYTIC SHARK-SKIN SURFACES WITH ANTIBACTERIAL AND ANTIFOULING ACTIVITY VIA NANOIMPRINT LITHOGRAPHY

Adapted from Arisoy, F. D.; ; Kolewe, K. W.; Homyak, B.; Kurtz, I. S.; Schi, J. D.; Watkins, J. J. Bioinspired Photocatalytic Shark-Skin Surfaces with Antibacterial and Antifouling Activity via Nanoimprint Lithography. *ACS Appl. Mater. Interfaces* **2018**, *10* (23), 20055–20063.

2.1 Introduction

Pathogenic microorganisms are transferred to at-risk patients through direct patient or clinician contact with contaminated high-touch surfaces[1,2] resulting in healthcare-associated infections (HAIs).[3] Although commercial antibiotics are the most common way to kill bacteria, their misuse and overuse has led to widespread antibiotic resistance, which results in greater than 2 million infections and 23,000 deaths in the United States, per year.[4–6] New coatings for high-touch surfaces, such as bed rails, door knobs, etc, that both limit the attachment of microorganisms and inactivate the persistent microbes are in high demand.[7,8]

Drawing inspiration from nature,[9–12] many biomimetic surface topographies have been shown to reduce microbial adhesion through a biocide-free structure-property relationship.[13–15] For example, the diamond-like riblets on the skin of sharks reduce drag and facilitate self-cleaning.[16–18] Brennan *et al.* fabricated Sharklet AF™, synthetic microstructures in silicone by replicating a silicon wafer mold prepared using

photolithography.[19] Because of their unique hierarchical design and engineered roughness index (ERI),[20] Sharklet AF™ patterned surfaces effectively inhibited the adhesion of the zoospores, *Ulva* (~5 μm diameter) and *Staphylococcus aureus (S. aureus)* (1 μm diameter).[19–22] Furthermore, Reddy *et al.* reported that silicone Sharklet AF™ surfaces reduced surface coverage by the Gram-negative bacteria *Escherichia coli (E. coli)* by up to 55% and the colony size by 76% compared to smooth films, after a 24 h incubation period.[23] However, Sharklet AF™ patterned surfaces share a limitation intrinsic to all microtopographic patterned surfaces: given a sufficient amount of time, bacteria will accumulate on the surface. For this reason, microtopography alone is insufficient and there is a need to develop multifunctional coatings that are antifouling and antibacterial.

Photocatalytic materials, including titanium dioxide (TiO_2), are effective antimicrobial agents that inactivate a wide array of microorganisms including both Gram -positive and -negative bacteria, fungi and viruses.[24,25] TiO_2-based nanocomposites have been extensively studied for a variety of applications, including surface disinfectants.[26–28] When TiO_2 absorbs UV light, redox reactions with H_2O or OH^- molecules form reactive hydroxyl radicals and superoxide ions, respectively.[29,30] Interaction of these reactive species with the outer membrane of bacteria induce rupture and subsequent cell death.[25] The benefits of using TiO_2 nanoparticles (NPs) compared to other well-known antibacterial agents (silver, copper, etc) are their low cost, wide availability, and ability to be incorporated into transparent coatings. These advantages make TiO_2 an attractive candidate for use in high-touch antimicrobial surface coatings.

In this work, we developed multifunctional surfaces by synergistically combining the antibacterial activity of TiO_2 with adhesion-resistant biomimetic shark skin microtopography. To the best of our knowledge, this work represents the first reported use

of antibacterial NPs in shark skin patterned surfaces. Orthogonal shark skin surfaces were fabricated using solvent-assisted nanoimprint lithography (NIL)[31,32] on flexible polyethylene terephthalate (PET) substrates from polymer and ceramic composite dispersions. Polymeric shark skin composites containing 10 wt% and 50 wt% TiO_2 NPs were prepared using Norland Optical Adhesive (NOA). Ceramic shark skin was prepared with 90 wt% TiO_2 NPs using tetraethyl orthosilicate (TEOS) as a binder. We further investigated the wettability, mechanical, antibacterial, and antifouling characteristics of the composites and shark skin patterned surfaces as a function of TiO_2 composition. Scalable and low-cost photocatalytic shark skin patterned surfaces offer high antimicrobial performance towards the development of light-assisted, environmentally friendly antifouling and antibacterial surface coatings.

2.2 Experimental Section

2.2.1 Materials

All materials were used as received without further purification. Titanium dioxide (TiO_2, anatase phase) nanoparticles (5-30 nm diameter) 15 wt% dispersed in water were purchased from Nanostructured & Amorphous Materials Inc. (Houston, TX). Norland Optical Adhesive 60 (NOA) was purchased from Norland Products, Inc. (Cranbury, NJ). N-methyl-2-pyrrolidone (NMP, ReagentPlus 99%), M9 minimal salts (M9 media), phosphate buffered saline (PBS, 10× sterile biograde), and 98% tetraethyl orthosilicate (TEOS) were purchased from Sigma-Aldrich (St. Louis, MO). Poly(vinyl alcohol) (PVOH, 80% hydrolyzed, 6 kg mol^{-1}) was purchased from Polysciences, Inc. (Warrington, PA). Methanol (MeOH) and poly(tetrafluoroethylene) (PTFE) filters (0.45 μm) were purchased from Fisher Scientific (Hampton, NH). Polyethylene terephthalate (PET) roll (ST 505, 125

μm thick films), Dupont, were purchased from Tekra Corporation (New Berlin, WI). Heptadecafluoro-1,1,2,2-tetrahydrodecyl)dimethylchlorosilane was acquired from Gelest (Morrisville, PA). Sylgard 184 silicone elastomer kit (polydimethylsiloxane (PDMS)) was purchased from Dow Corning (Midland, MI).

2.2.2 Solvent Exchange of TiO_2 Nanoparticle (NP) Dispersion

The details of solvent exchange can be found in previous publications from our group.[31] Briefly, TiO_2 (100 g of 15 wt%) aqueous dispersion was added into a 250 mL bottle. NMP (50 g) and MeOH (50 g) were added to the dispersion and mixed. The mixed solution was placed under air flow overnight until majority of the solvent was removed, resulting in a slurry. The amount of the solvent and solid were calculated and subsequently, NMP and MeOH were added in a 1:1 weight ratio to the slurry mixture to obtain an approximately 15 wt% TiO_2 dispersion. The dispersion was sonicated (~30 min) until stable TiO_2 NP dispersions were obtained. The final TiO_2 concentration was calculated as 15.2 wt% and remained stable for a year.

2.2.3 PDMS Mold Fabrication

Sample compositions are named as NOA (100 wt% NOA), TiO_2-10 (10 wt% TiO_2/90 wt% NOA), TiO_2-50 (50 wt% TiO_2/50 wt% NOA), and TiO_2-C (90 wt% TiO_2/10 wt% TEOS). In order to fabricate shark skin patterns from NOA, TiO_2-10, TiO_2-50, and TiO_2-C with the same dimensions, two different masters (*Master 1* and *Master 2*) were used as further explained in the results and discussion section.

Master 1: Soft PDMS replica molds were fabricated using the standard fabrication method.[33] PDMS was prepared by mixing Sylgard 184 at a 1:10 ratio of curing agent to base, then poured onto a Sharklet nickel (*Master 1*; height: 3 μm, width: 2 μm, pitch: 4

μm) mold (provided by Sharklet Technologies) and placed into an oven to be crosslinked at 70 °C for 3 h. The PDMS was then peeled off from the *Master 1* to obtain a soft mold of the inverse Sharklet structure. The inverse Sharklet PDMS mold was used to imprint TiO_2-50 and TiO_2-C shark skin patterns.

Master 2: A TiO_2-50 patterned shark skin sample used as a master mold (*Master 2*; height: 1.6 μm, width: 1.3 μm, pitch: 4 μm). TiO_2-50 was placed in an oxygen (O_2) plasma cleaner for 2 min, then the surface modified with (heptadecafluoro-1,1,2,2-tetrahydrodecyl)-dimethylchlorosilane at 60 °C for 12 h to obtain an anti-sticking surface. The inverse shark skin PDMS mold was prepared from *Master 2* using the same procedure given above. Inverse shark skin PDMS mold was used to imprint NOA and TiO_2-10 shark skin patterns.

2.2.4 Shark Skin Pattern Fabrication Using Solvent-Assisted NIL

PET substrates were cleaned using ethanol and isopropanol then exposed to O_2 plasma for 3 min and used as substrate for the imprints. TiO_2 composite dispersions were prepared using solvent-exchanged 15.2 wt% TiO_2 (NMP/MeOH). To prepare NOA shark skin patterns, a 20 wt% NOA solution in NMP was spin-coated onto a PET substrate, then an PDMS stamp (replica from *Master 2*) was placed on top. TiO_2-10 (10 wt% TiO_2/90 wt% NOA) dispersion was prepared as a 17 wt% (solids) dispersion in NMP/MeOH and spin-coated to form an 800 nm film. A PDMS mold (replica from *Master 2*) was then placed on top. A TiO_2-50 (50 wt% TiO_2/50 wt% NOA) dispersion was prepared as 30 wt% (solids) dispersion in NMP/MeOH and spin-coated to form an 800 nm film. A PDMS mold (replica from *Master 1*) was then placed on top. TiO_2-C (90 wt% TiO_2/10 wt% TEOS) dispersion was prepared as 17 wt% solid in NMP/MeOH and spin-coated to form an 800 nm film. A PDMS mold (replica from *Master 1*) was then placed on top. The assemblies were placed

on a 50 °C hot plate for 30 min to evaporate residual solvents. NOA, TiO_2-10, and TiO_2-50 assemblies were UV cured to obtain crosslinked structures (UV light wavelength: 365 nm, with an energy of 11 J/cm^2).[31] TiO_2-C assembly was NIR (Adphos, 3 KW) irradiated (10 s) to quickly obtain silica binding. For each case, PDMS was gently peeled off from the coating and the shark skin patterns were obtained. NOA, TiO_2-10, TiO_2-50, and TiO_2-C dispersions were used to fabricate smooth films with the same chemistry as the patterned samples. UV or NIR curing procedures were conducted for corresponding samples.

2.2.5 Materials Characterization

To prepare thin films for transmission electron microscopy (TEM) imaging, glass substrates were coated with a PVOH sacrificial layer and placed on a hot plate for 1 min. Thin films (~100 nm) of TiO_2-10, TiO_2-50, and TiO_2-C composites were spin-coated onto PVOH. Films were floated on water after PVOH was dissolved and picked-up by carbon coated copper grids for TEM. In addition to composite films, solvent exchanged TiO_2 NPs in NMP/MeOH were diluted further with NMP/MeOH and drop casted on a carbon coated copper grid for TEM characterization. TEM was performed in bright field imaging mode using a JEOL 2000 FX TEM operated at an accelerating voltage of 200 kV. To measure the mechanical properties of NOA, TiO_2-10, TiO_2-50, TiO_2-C films, dispersions of each polymer and ceramic composite were spin-coated into films of 800 to 1200 nm on PET substrates. The hardness and reduced modulus of films were determined using a Hysitron TriboIndenter (TI 950) by averaging 30 indentations obtained under rate control (10 μN/s) using a Berkovich tip (100 nm) for each film. Significant difference was determined by analysis of variance (ANOVA) with Tukey test. Values of $p<0.05$ was considered to be significant. The concentration of TiO_2 NPs was confirmed by thermogravimetric analysis (TGA, TA Instruments Q50) using the following temperature program under air: heating

from room temperature to 700 °C, with a rate of 10 °C/min. Scanning electron microscopy (SEM) was performed on a field emission SEM (Magellan 400). The NOA and TiO_2-10 shark skin samples were gold sputtered using a sputter coater (CR 108) for 45 s prior to imaging. The TiO_2-50 and TiO_2-C shark skin samples were imaged as-produced in the SEM. 3D optical profilometer (Zygo, Nexview) was used to measure feature dimensions. Contact angle measurements were acquired using a VCA Optima surface analysis/goniometry system. Prior to testing, shark skin patterned samples were kept in the dark for 14 days to minimize UV effects. Static, advancing, and receding water contact angles were determined from parallel and orthogonal directions using 6 independent measurements at room temperature (5 μL water drops were used).

2.2.6 Antifouling Performance

The fouling resistance of shark skin patterned NOA, TiO_2-10, TiO_2-50, and TiO_2-C composites, as well as smooth chemistry controls were evaluated with a bacterial attachment assay using the model bacteria, *Escherichia coli* K12 MG1655 (*E. coli*, expressing green fluorescent protein).[34] *E. coli* was cultured overnight in Luria-Bertani broth (Sigma-Aldrich) then washed and re-suspended in M9 media to a final concentration of 1×10^8 cells/mL. Samples were placed at the base of separate wells in 6-well polystyrene plates (Fisher Scientific) and inoculated with 5 mL of *E. coli* suspended in M9 media. Following a 24 h incubation period at 37 ºC, the growth media was removed using a sterilized glass pipette and samples were rinsed repeatedly with PBS before analysis. Samples were analyzed using a Zeiss Microscope Axio Imager A2M (20× and 50× magnification, Thornwood, NY). The surface area coverage of attached bacteria was quantified by analyzing 10–15 randomly acquired images over at least three parallel replicates using *ImageJ* 1.45 software (National Institutes of Health, Bethesda, MD).

2.2.7 Antibacterial Activity

The antibacterial activity of the samples were evaluated using a using a standard assay modified to expose the samples to UV light.[35] Smooth thin films of TiO_2-10, TiO_2-50, and TiO_2-C were evaluated in parallel with controls including NOA, PET, and glass slides (data not shown). Samples were placed at the base of separate wells in 6-well polystyrene plates to which 5 mL of M9 media containing *E. coli* or *S. aureus* (1×10^8 cells/mL) were added before incubating for 1 h at 37 °C under UV light (F15W/T8 McMaster-Carr, 15W 365 nm wavelength). Samples were held at a 15 cm fixed distance from the UV source. UV light intensity was measured using a UV light meter (Thorlabs GM10HS, Hamamatsu S2281 probe) and determined to be 1.0 mW/cm^2. Following photoactivation, the samples were removed and stained with propidium iodide (PI) for 15 min to identify the dead cells before being throughly washed with PBS to remove excess stain. The loss of viability was visualized using a Zeiss Microscope Axio Imager A2M, quantified using *ImageJ* software, and the percentage of dead cells (or loss of viability) was calculated from the ratio of the number of cells stained with PI divided by the total number of cells.[35]

Statistics: Significant differences between samples were determined with an unpaired Student *t*-test. Significance is denoted in the graphs using asterisks and defined in the figure captions.

2.3 Results and Discussion

2.3.1 Polymer and Ceramic Composite Shark Skin Pattern Fabrication

Orthogonal shark skin microstructures were successfully imprinted using TiO_2 loaded dispersions via solvent assisted NIL,[31,32] as shown in **Figure 2.1**. The *Master 1* mold

(height: 3 μm, width: 2 μm, pitch: 4 μm) and the *Master 2* mold (height: 1.6 μm, width: 1.3 μm, pitch: 4 μm) consist of riblets, with different lengths ranging from 4-16 μm (**Figure 2.2**). While *Master 1* (Nickel mold) was provided by Sharklet Technologies, *Master 2* (TiO_2-50) was made of a TiO_2-50 shark skin patterned sample. The soft PDMS molds were replicated from the masters, and therefore contain the inverse structure of the master and can be used to imprint the original-tone pattern on PET substrates. Dispersions of NOA, TiO_2-10, TiO_2-50, and TiO_2-C were spin-coated onto PET substrates with sufficient residual solvent so that the coating had an appropriate viscosity (liquid enough) to fill the PDMS when placed in contact on top of the coating. The PDMS mold was kept on the substrate until the shark skin microstructures were formed, which was about 30 min, although the pattern transfer process was not optimized for cycle time. Other publications from our group show NIL patterning of titania surface patterns with cycle times of a few minutes or less.[32,36] NOA, TiO_2-10, and TiO_2-50 assemblies were cured under UV exposure and ceramic TiO_2-C shark skin assemblies were cured under NIR irradiation. After completing the curing process, the PDMS mold was peeled off, revealing microstructured shark skin patterned films. The mechanism behind the pattern formation via solvent assisted NIL is a result of the capillary force that drives the solution to form into the shape of the mold.[31,32] As the solvent evaporates through the air-permeable PDMS stamp, the patterned structures form.

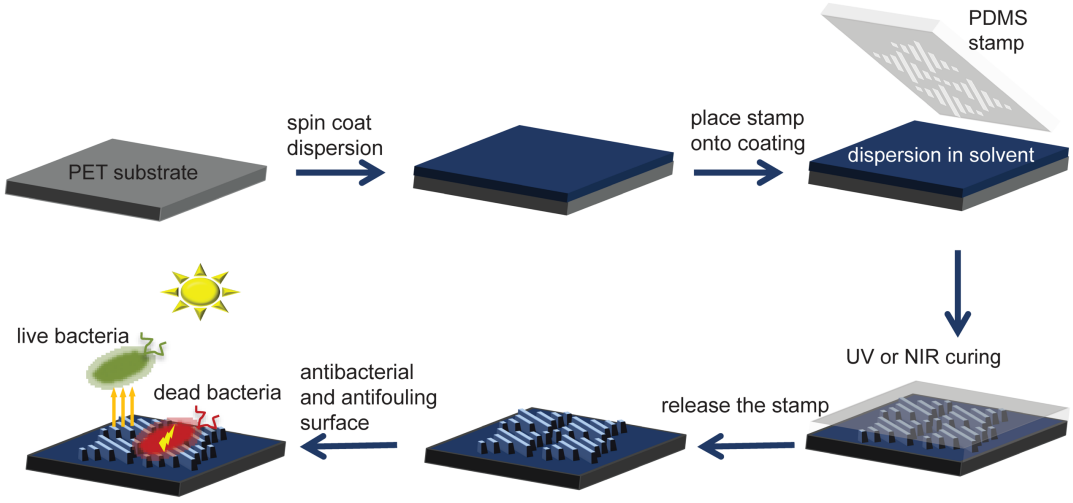

Figure 2.1. Schematic representation of the fabrication process of shark skin patterns using a PDMS soft stamp on flexible PET substrates.

Our goal was to fabricate all shark skin patterned surfaces with the same dimensions as the TiO_2-C shark skin microstructures. Notably, as the solvent evaporates during imprinting, the TiO_2 NPs pack and shrink more than the polymer. Depending on the amount of solvent during imprint, the dimensions of the features change, resulting in features with dimensions less than the mold dimensions. Whereas, polymer materials can be imprinted with a perfect replication of the master mold.[37] Thus, to make NOA and TiO_2-10 imprints with the same dimensions as TiO_2-C, we used a different master mold (*Master 2*) than the one used for TiO_2-50 and TiO_2-C shark skin patterned structures (*Master 1*).

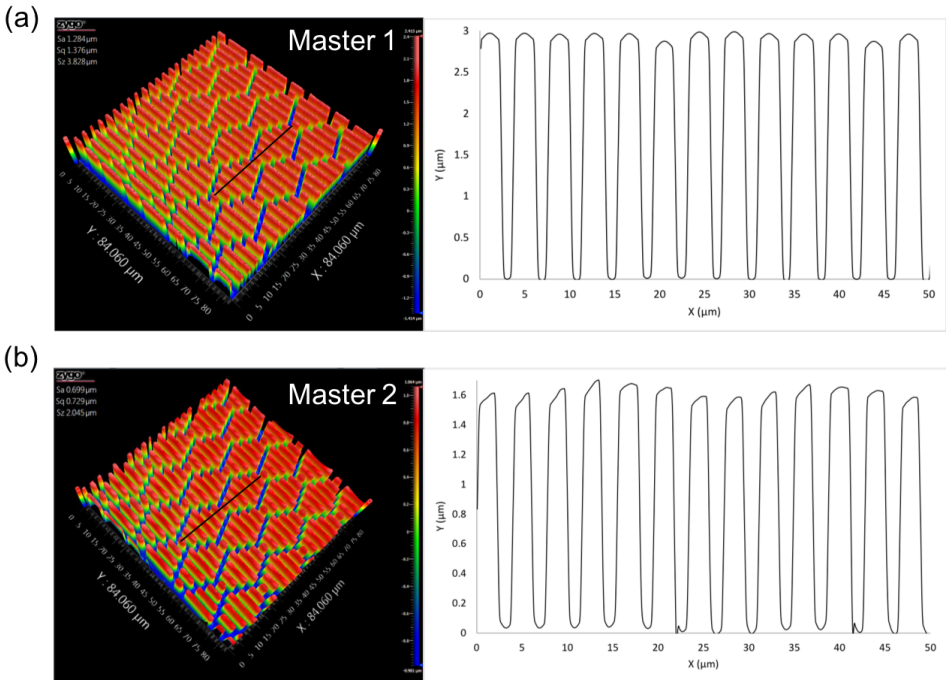

Figure 2.2. Optical profilometry images and dimensions of **(a)** *Master 1* (nickel mold) and **(b)** *Master 2* (TiO_2-50 mold).

The use of stable dispersions is a key requirement to obtain uniform filling of the stamp, which results in reproducible, well-replicated structures. Due to the high surface tension of aqueous solutions, wetting interactions between the solution and PDMS mold are not favorable without the use of surfactants. Organic solvents such as N-methyl-2-pyrrolidone (NMP) and methanol (MeOH) have lower surface tension, which makes them preferable for solvent-assisted NIL. Moreover, the use of organic solvents and an elevated temperature (50 °C) increased solvent evaporation in solvent-assisted NIL, decreasing the overall imprint time. Thus, solvent exchange was conducted from water to a solvent mixture of NMP/MeOH yielding a stable dispersion of 10-15 wt% TiO_2 NPs. MeOH, which is highly volatile, allows for fast film formation, while NMP, which is less volatile, evaporates more slowly and therefore, allows sufficient time for the imprinting process. Furthermore, NMP is a common solvent to disperse both NOA and TiO_2 NPs. Relative

humidity (RH) is also an important parameter to consider when trying to obtain reproducible patterned surfaces. At high RH (above 30%), spin-coated films become thinner.[32] Optimum humidity was determined as below 20% RH. Spin-coating speed and time can be adjusted according to RH to obtain desirable thickness and fluidity of the film.

2.3.2 Characterization of the Composites

NOA is a UV curable optical adhesive material that has been used as matrix for NP composites.[31,38] In our study, we chose NOA as a model nanoimprint lithography matrix for several reasons, including that NOA can homogeneously disperse TiO_2 NPs, NOA cures in several seconds to minutes depending on film thickness and light intensity, and NOA has favorable mechanical properties, such as high modulus.[31,39] TiO_2-10 and TiO_2-50 shark skin microstructures were prepared as 10 wt% and 50 wt% TiO_2 loading to NOA. The loading of TiO_2 NPs in samples TiO_2-10 and TiO_2-50 was measured by TGA and confirmed to be 10 wt% and 50 wt%, respectively (**Figure 2.3**).

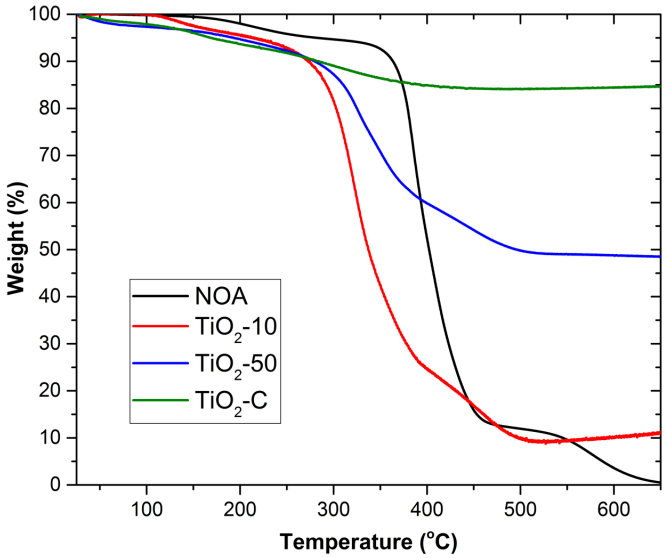

Figure 2.3. TGA of NOA, TiO_2-10, TiO_2-50, and TiO_2-C.

Fully ceramic TiO_2-C samples were prepared using a 90 wt% TiO_2 and 10 wt% TEOS dispersion, in which TEOS polymerizes under NIR irradiation to create a SiO_2 binder to obtain ceramic coatings. The resulting crosslinked silica structures generated upon heating prevent deformation of microstructures after immersing the films in an aqueous solution. The samples without NIR curing were not stable in water overnight. Light sintering has several advantages compared to thermal sintering such as rapid process times and ability to sinter directly on flexible polymeric substrates. In previous works, NIR heating of TiO_2 NPs was performed on metallic and fluorine doped tin oxide (FTO) glass substrates. NIR light was absorbed by the substrates and heat the film up to 700 °C in 12.5 s.[40,41] The PET substrate does not absorb NIR, however due to absorption of TiO_2 above 1800 nm[42], heat radiation makes silica binding form quickly (10 s). Through NIR light annealing, ceramic TiO_2-C shark skin structures were obtained on flexible PET substrates.

TEM images of TiO_2 NPs and TiO_2-10, TiO_2-50, and TiO_2-C films are shown in **Figure 2.4**. The average TiO_2 NP size was calculated to be 8.7 ± 4.5 nm by measuring at least 100 particles across multiple TEM images. The TEM micrographs indicate that the TiO_2-10 composites exhibit a homogeneous dispersion of NPs, without any agglomeration; this is in contrast what was observed for the TiO_2-50 composite. In the ceramic sample, TiO_2-C, a high concentration of nanoparticles was observed, and as expected, the quick NIR treatment did not change the average size of the NPs.

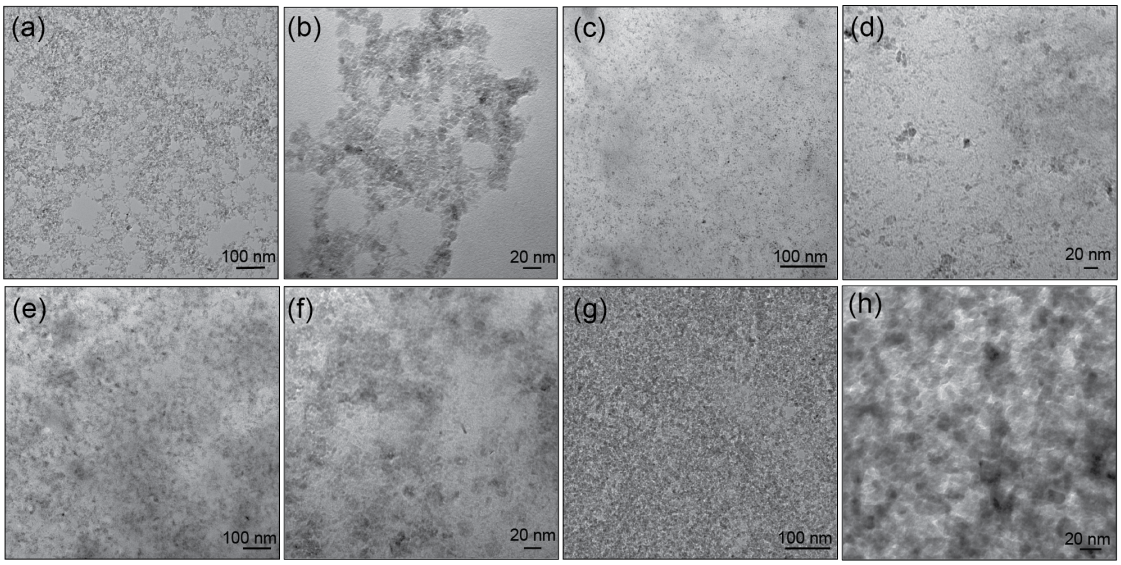

Figure 2.4. TEM images of low and high magnifications **(a, b)** TiO_2 NPs (drop casted from solvent exchanged TiO_2 (NMP/MeOH) dispersion), as well as the **(c, d)** TiO_2-10, **(e, f)** TiO_2-50, **(g, h)** TiO_2-C composite films.

The mechanical properties of composites were characterized using nanoindentation.[43,44] During the measurements, indentation depth did not exceed 10% of the film thickness to prevent substrate effects. Hardness and reduced modulus values are shown in **Table 2.1**. The hardness of NOA and TiO_2-10 were determined to be 279 ± 14 MPa and 278 ± 32 MPa, respectively. There was not a significant difference in the hardness and modulus values between NOA and TiO_2-10. However, as the loading of TiO_2 NPs increased, from TiO_2-10 to TiO_2-50, the hardness decreased significantly from 278 ± 32 MPa to 204 ± 81 MPa and modulus decreased from 4.6 ± 0.4 GPa to 4.0 ± 0.8 GPa, potentially due to a decreased crosslinking density of the NOA matrix. Under UV exposure, the TiO_2 present in the composite materials may be preventing full curing due to the UV absorption of TiO_2. The hardness and modulus of the fully-ceramic TiO_2-C films were determined to be 490 ± 68 MPa and 16 ± 2 GPa, respectively, which were significantly higher than the polymeric composite materials. As expected, the fully ceramic nature of

these films gave rise to ~75% and ~233% increase in hardness and reduced modulus respectively, compared to the polymeric composite materials.

Table 2.1. Nanomechanical analysis of composite materials. Standard deviation is displayed.

	NOA	TiO_2-10	TiO_2-50	TiO_2-C
Hardness (MPa)	$279^a \pm 14$	$278^a \pm 32$	$204^b \pm 81$	$490^c \pm 68$
Reduced Modulus (GPa)	$4.8^a \pm 0.2$	$4.6^a \pm 0.4$	$4.0^a \pm 0.8$	$16^b \pm 2$

Superscript letters within a row indicate statistically significant differences at $p<0.05$ level (Tukey's HSD).

2.3.3 Characterization of Shark Skin Patterned Surfaces

The SEM micrographs of shark skin patterned surfaces in NOA (**Figure 2.5a**), TiO_2-10 (**Figure 2.5b**), TiO_2-50 (**Figure 2.5c, 2.5d**), and TiO_2-C (**Figure 2.5e, 2.5f**) are shown in **Figure 2.5**. The dimensions of the shark skin imprints were determined using an optical profilometer and from SEM imaging. The height, width and spacing of riblets were ~1.6 μm, 1.3 μm and 2.7 μm, respectively (**Figure 2.5**). All the features were replicated uniformly in size and shape over a large area (4 cm × 4 cm). Digital pictures of the shark skin patterns on PET substrates are shown in **Figure 2.6**. We have also prepared NOA* (100% NOA) shark skin with the same dimensions of the *Master 1* as a control patterned surface, **Figure 2.7.** The antifouling properties of NOA* (height: 3 μm, width: 2 μm, spacing: 2 μm) patterned surfaces were compared with NOA (height: 1.6 μm, width: 1.3 μm, spacing: 2.7 μm) patterned surfaces to understand if increasing the spacing between the features would affect the adhesion of *E. coli*.

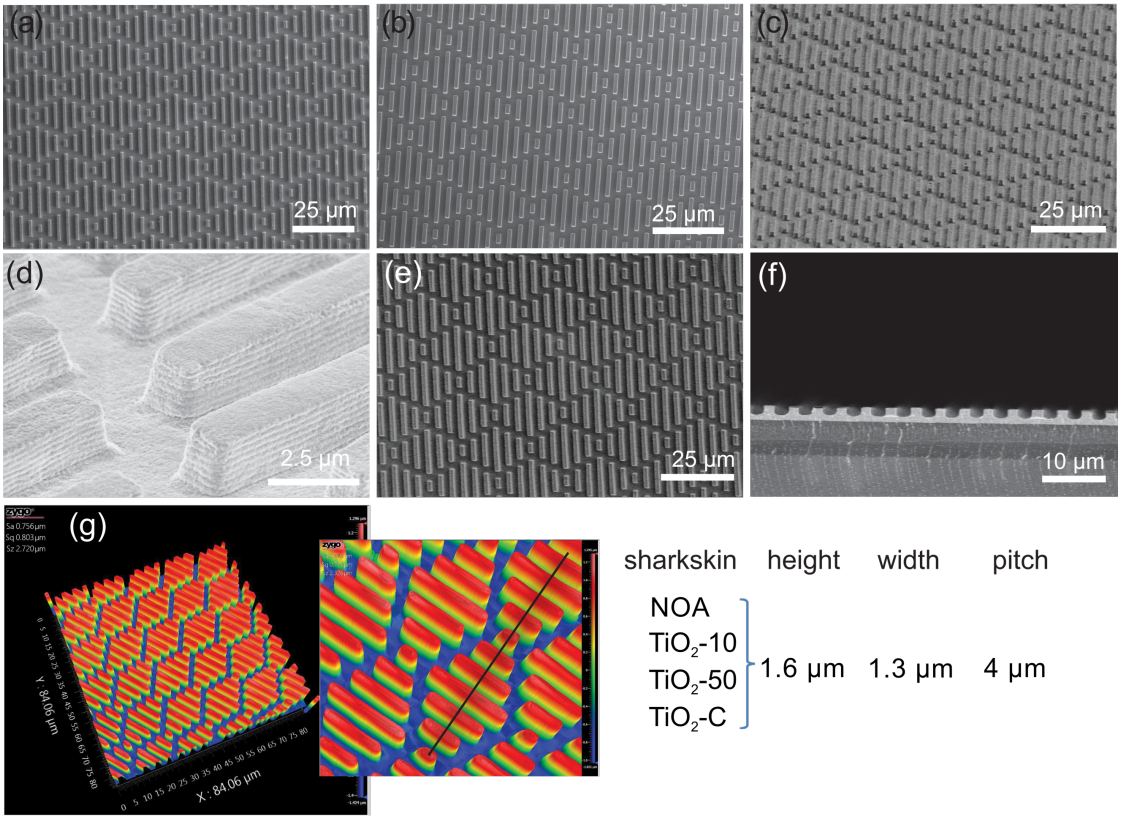

Figure 2.5. SEM images and dimensions of shark skin patterns with different composites. **(a)** NOA (top view), **(b)** TiO_2-10 (top view), **(c)** TiO_2-50 (45° tilted), **(d)** TiO_2-50 (45° tilted, high mag), **(e)** TiO_2-C (top view), **(f)** TiO_2-C (cross section), and **(g)** optical profilometry images and dimensions of shark skin patterned surfaces.

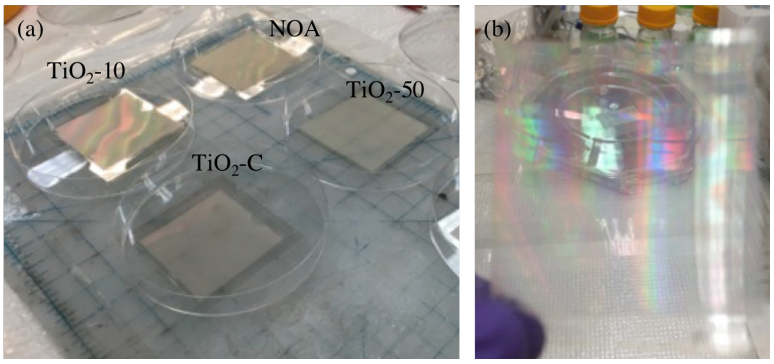

Figure 2.6. (a, b) Digital photos of NOA, TiO_2-10, TiO_2-50, and TiO_2-C shark skin patterns on a PET substrate (4 cm × 4 cm).

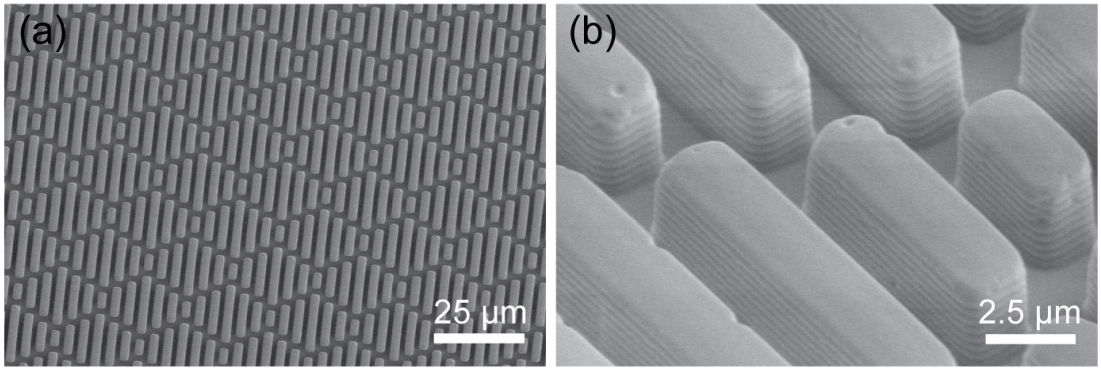

Figure 2.7. SEM micrographs of NOA* (100% NOA) shark skin surfaces as a control patterned surface (a) top view, (b) 45° tilted. Imprints were conducted using a PDMS mold from *Master 1* (height: 3 µm, width: 2 µm, pitch: 4 µm).

After imprints were successfully achieved, their advancing, receding and static water contact angles were determined, and the results are shown in **Figure 2.8**. As the concentration of TiO_2 NPs in the patterned surfaces increased, the static contact angle decreased from 139° to 106°. This is due to high affinity of TiO_2 for water. The contact angles were recorded parallel and perpendicular to features due to anisotropy of the surfaces. Difference in contact angle from different direction is expected and can be explained by the energy barrier, which was observed for discontinuous gradient surfaces, consistent with Sharklet AF™ surfaces.[45] In addition, a higher contact angle hysteresis (CAH) was observed for the photocatalytic shark skin microstructures (~100°) compared to the NOA shark skin surface (~30°). This can be explained by chemical heterogeneous composition and the interaction between TiO_2 NPs and water.[46,47] Despite the high CAH observed in the photocatalytic shark skin surfaces, these surfaces demonstrated a great ability to resist the initial attachment of bacteria. Overall, the antifouling property of shark skin patterned surfaces is closely linked to the organisms' size relative to the surface topography and potentially, also due to biological mechanisms. The CAH of a surface does not play the key role in repelling microbes from patterned surfaces.[15,48–50]

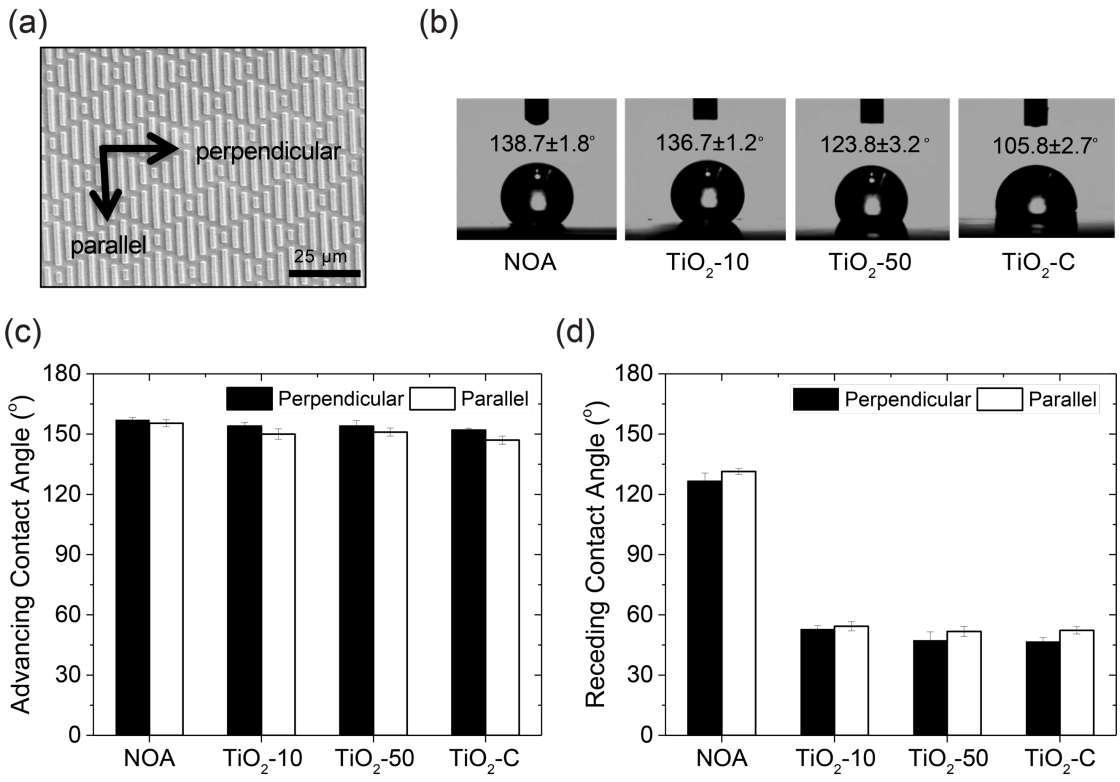

Figure 2.8. Water contact angle analysis of shark skin patterned surfaces. **(a)** Schematic representation of perpendicular and parallel directions to the shark skin patterns. **(b)** Static water contact angle on shark skin patterned surfaces, **(c)** Advancing water contact angle perpendicular and parallel to the of shark skin patterned surfaces. **(d)** Receding water contact angle perpendicular and parallel to the of shark skin patterned surfaces. Error bars denote standard deviation.

2.3.4 Antifouling Activity of Shark Skin Patterned Surfaces

The 24 h antifouling properties of shark skin patterned surfaces were tested using the model Gram-negative microorganism, *E. coli*, and compared to smooth chemistry controls **Figure 2.9 and Figure 2.10**. Bacterial adhesion is influenced by many factors including the topography, chemistry, and mechanical properties of a surface.[34,51,52] Shark skin patterned surfaces (of all composite chemistries) reduced bacterial surface area coverage to less than 1% of the total surface area of the sample. NOA, TiO_2-10, TiO_2-50, and TiO_2-C shark skin patterned surfaces displayed surface area coverages of 0.67 ±

0.20%, 0.57 ± 0.18%, 0.58 ± 0.17%, and 0.79 ± 0.22%, respectively. Compared to smooth films with the same chemistry, shark skin patterned NOA surfaces reduced bacterial area coverage by up to 85% and TiO_2-10, TiO_2-50, and TiO_2-C surfaces reduced bacterial area coverage by up to 70%. Compared to flat PET controls, shark skin patterned surfaces reduced *E. coli* attachment by up to 80% (**Figure 2.10**).

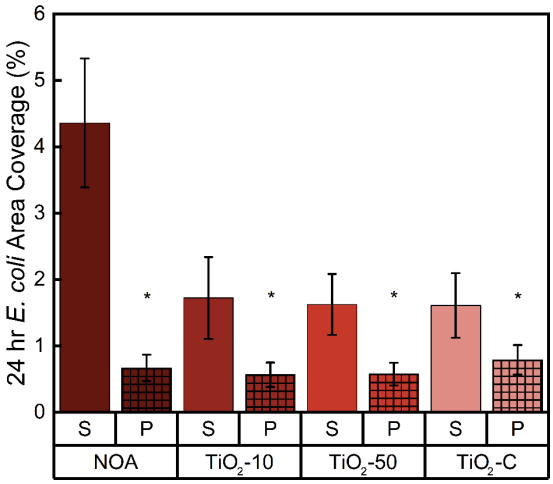

Figure 2.9. The 24 h area coverage of surface-adhered E. coli on smooth films (S) versus patterned surfaces (P) of NOA, TiO_2-10, TiO_2-50, and TiO_2-C. An asterisk (*) denotes 95% significance between smooth and patterned samples. Error bars denote standard error.

Although smooth TiO_2 composites decreased the bacterial attachment up to 60% compared to NOA smooth samples, there was no significant difference between the antifouling activity of the NOA, TiO_2-10, TiO_2-50, and TiO_2-C shark skin patterned surfaces. These results indicate that surface topography dominated over the chemical composition of the shark skin surfaces. Moreover, doubling the height, and increasing the aspect ratio and spacing of the features, NOA* (height: 3 µm, aspect ratio: 1.5, spacing: 2 µm), did not elicit a statistically significant difference in *E. coli* area coverage compared to NOA (height: 1.6 µm, aspect ratio: 1.2, spacing: 2.7 µm) shark skin surfaces (**Figure 2.10**). While Schumacher *et al.*, found that increasing the aspect ratio of PDMS Sharklet

AF™ surfaces significantly reduced the attachment of Ulva spores and barnacle cyprids by up to 42%-45%, this was due to the larger size of their organism.[53]

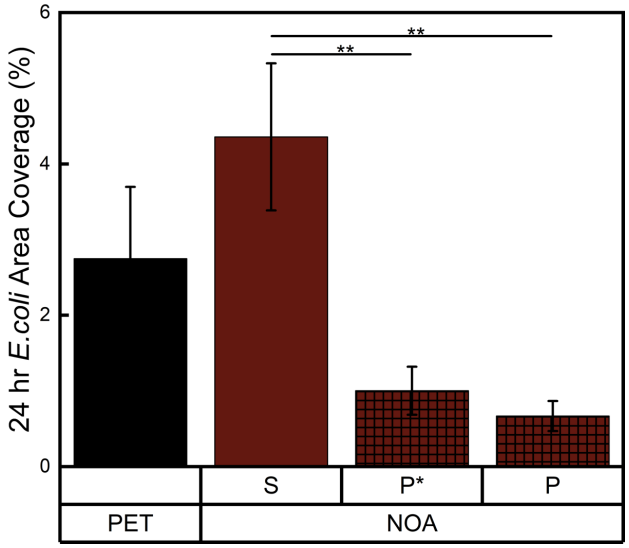

Figure 2.10. The total area coverage of surface-adhered E. coli on smooth (S) and patterned (P) NOA surfaces, as well as on PET controls. The dimensions of NOA (P) surfaces are height: 1.6 µm, width: 1.3 µm, and spacing: 2.7 µm, whereas NOA* (P*) dimensions are height: 3 µm, width: 2 µm, and spacing: 2 µm. Two asterisks (**) indicates that values are significantly different at 0.01 level. Standard error is provided.

The *E. coli* that adhered to the surfaces was observed between the features (**Figure 2.11**), consistent with previous studies.[23] If the spacing between the features is larger than the width of the bacteria, bacteria falls between the patterns and attaches to the spaces rather than being repelled by the features.[15,54,55] However, due to physical disturbance of the microstructures, cell to cell interactions decrease and delays colony formation. In the long term, the bacteria can still form a biofilm if the adhered bacteria continue to live on the engineered surfaces, thus, a killing mechanism is needed to inactivate the settled microbes.

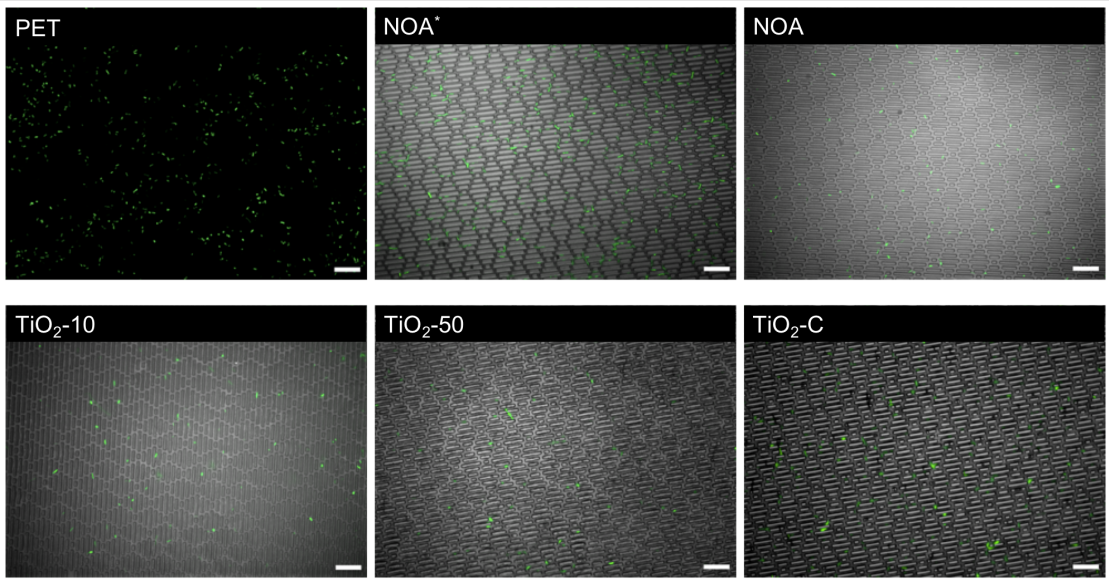

Figure 2.11. Fluorescent micrographs show that E. coli adhered between the patterned features. All scale bars are 20 µm.

2.3.5 Antibacterial Activity of TiO_2 NP Composites

The photocatalytic antibacterial activity of flat films was evaluated using the model microbial species *E. coli* and *S. aureus*, **Figure 2.12**. All composite compositions that contained TiO_2 NPs (TiO_2-10, TiO_2-50, and TiO_2-C) showed significant antibacterial activity, 90 ± 4%, 83 ± 6%, and 93 ± 2%, respectively for *E. coli*, and 83 ± 5%, 80 ± 8%, and 80 ± 7%, respectively for *S. aureus* after 1 h of UV light exposure. The control samples, flat PET and NOA, showed only baseline inactivation, ~5% killing. Notably, there was not a significant difference in the killing efficiency between the lowest, TiO_2-10, and the highest, TiO_2-C, TiO_2 concentration samples. The concentration, size, and phase of TiO_2, the polymer matrix, and additives are the main factors that influence antibacterial activity of TiO_2 NPs.[26,56,57] In our experiments, we used anatase phase TiO_2 NPs, which were reported to exhibit higher photocatalytic activity compared to rutile phase NPs.[26,58]

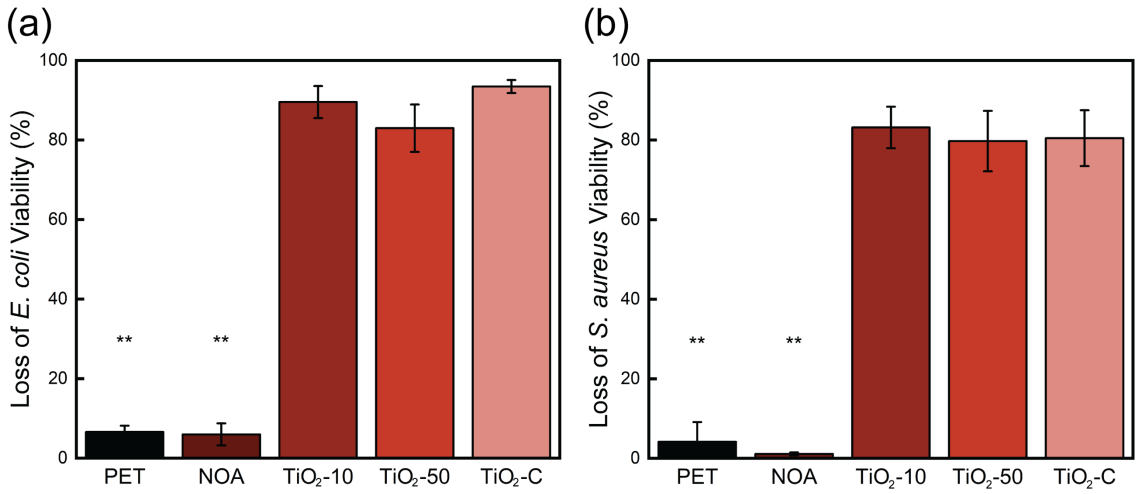

Figure 2.12. Loss of (a) E. coli and (b) S. aureus viability after 1 h of UV exposure to planar TiO_2-10, TiO_2-50, and TiO_2-C films. Control PET and NOA surfaces (no TiO_2) are also provided. Two asterisks (**) denotes 99% significance between control and TiO_2-containing samples. Error bars denote standard error.

Another important factor is how homogeneous the dispersion of NPs is within the matrix. Kubacka *et al.* reported that by using only 2 wt% TiO_2 NPs (~9 nm) in ethylene-vinyl alcohol copolymer composite, they had a 6.3 log reduction of *P. aeruginosa* after 30 min due to well distributed NPs.[59] A homogeneous dispersion of nanoparticles increases the available surface area, diffusion of reactive hydroxyl radicals and superoxide ions, and therefore, increases their photocatalytic activity. Here, composites were prepared without using any ligands or dispersing agents and still resulted in a sufficiently homogeneous dispersion using a straightforward solution processing technique. Alternatively, one could also incorporate metal NPs such as copper or silver into the TiO_2 composite material. In this way, the band gap decreases and absorption of light shifts towards the visible light.[60,61] Another factor that influences antibacterial performance is the UV source and source intensity.[57] Here we used a UV lamp (365 nm) with a weak light intensity of 1.0 mW/cm^2, which still had an excellent antibacterial activity in 1 h. Notably, while TiO_2 is known to have degradative effects on organic materials, with low enough UV intensity, polymer composites can maintain their performance. Here, while the degradation kinetics of

polymer composites was not investigated because it was beyond the scope of this project, we hypothesize that because the UV exposure was sufficiently low, minimal degradation occurred.

2.4 Conclusions

We have presented a simple strategy to fabricate multifunctional shark skin surfaces with antifouling and antibacterial properties. Moreover, ceramic shark skin coatings (TiO_2-C) were successfully imprinted on a flexible PET substrate and cured using only 10s of NIR irradiation. We studied the wetting and mechanical properties of shark skin patterned surfaces as a function of TiO_2 loading in the composites. Introduction of TiO_2 NPs increased CAH from 30^o to 100^o on shark skin surfaces. The hardness and reduced modulus were not significantly altered by increasing TiO_2 NPs up to 50 wt%; however, the hardness of ceramic TiO_2-C sample increased by up to 2 times compared with NOA, TiO_2-10, and TiO_2-50. Shark skin surfaces reduced the attachment of *E. coli* by 70-85% and killed 85-95% of *E. coli* and *S. aureus* after 1 h of UV light exposure. To the best of our knowledge, this work represents the first reported use of antibacterial NPs in shark skin patterns. The combination of passive and active strategies on a single surface is a most promising material design strategies to control bacterial fouling. Our fabrication technique is a roll-to-roll compatible method that can be scaled up to be used for practical applications.

2.5 References

(1) Boyce, J. M.; Havill, N. L.; Otter, J. A.; Adams, N. M. T. Widespread Environmental Contamination Associated With Patients With Diarrhea and Methicillin-Resistant Staphylococcus Aureus Colonization of the Gastrointestinal Tract. *Infect. Control Hosp. Epidemiol.* **2007**, *28* (10), 1142–1147.

(2) Carling, P. C.; Briggs, J.; Hylander, D.; Perkins, J. An Evaluation of Patient Area Cleaning in 3 Hospitals Using a Novel Targeting Methodology. *Am. J. Infect. Control* **2006**, *34* (8), 513–519.

(3) Weber, D. J.; Rutala, W. A.; Miller, M. B.; Huslage, K.; Sickbert-Bennett, E. Role of Hospital Surfaces in the Transmission of Emerging Health Care-Associated Pathogens: Norovirus, Clostridium Difficile, and Acinetobacter Species. *Am. J. Infect. Control* **2010**, *38* (5 SUPPL.), S25–S33.

(4) Pogorzelska-Maziarz, M.; Carter, E. J.; Manning, M. L.; Larson, E. L. State Health Department Requirements for Reporting of Antibiotic-Resistant Infections by Providers, United States, 2013 and 2015. *Public Health Rep.* **2016**, *132* (1), 32–36.

(5) Centers for Disease Control and Prevention (CDC). Antibiotic Resistance Threats in the United States, 2013. Atlanta, Georgia: U.S. Department of Health and Human Services, CDC, 2013. Available at: http://www.cdc.gov/drugresistance/threat-report-2013.

(6) Stewart, P. S.; Costerton, J. W. Antibiotic Resistance of Bacteria in Biofilms. *Lancet* **2001**, *358* (9276), 135–138.

(7) Costerton, J. W.; Stewart, P. S.; Greenberg, E. P. Bacterial Biofilms: A Common Cause of Persistent Infections. *Science.* **1999**, *284* (5418), 1318–1322.

(8) Lu, Y.; Yue, Z.; Wang, W.; Cao, Z. Strategies on Designing Multifunctional Surfaces to Prevent Biofilm Formation. *Front. Chem. Sci. Eng.* **2015**, *9* (3), 324–335.

(9) Zhao, N.; Wang, Z.; Cai, C.; Shen, H.; Liang, F.; Wang, D.; Wang, C.; Zhu, T.; Guo, J.; Wang, Y.; Liu, X.; Duan, C.; Wang, H.; Mao, Y.; Jia, X.; Dong, H.; Zhang, X.; Xu, J. Bioinspired Materials : From Low to High Dimensional Structure. *Adv. Mater.* **2014**, *26*, 6994–7017.

(10) Bhushan, B. Biomimetics: Lessons from Nature-an Overview. *Philos. Trans. R. Soc. A Math. Phys. Eng. Sci.* **2009**, *367* (1893), 1445–1486.

(11) Liu, K.; Jiang, L. Bio-Inspired Self-Cleaning Surfaces. *Annu. Rev. Mater. Res.* **2012**, *42* (1), 231–263.

(12) Scardino, A. J.; de Nys, R. Mini Review: Biomimetic Models and Bioinspired Surfaces for Fouling Control. *Biofouling* **2011**, *27* (1), 73–86.

(13) Hasan, J.; Chatterjee, K. Recent Advances in Engineering Topography Mediated Antibacterial Surfaces. *Nanoscale* **2015**, *7* (38), 15568–15575.

(14) Genzer, J.; Efimenko, K. Recent Developments in Superhydrophobic Surfaces and Their Relevance to Marine Fouling: A Review. *Biofouling* **2006**, *22* (5–6), 339–360.

(15) Graham, M.; Cady, N. Nano and Microscale Topographies for the Prevention of Bacterial Surface Fouling. *Coatings* **2014**, *4* (1), 37–59.

(16) Liu, K.; Jiang, L. Bio-Inspired Self-Cleaning Surfaces. *Annu. Rev. Mater. Res.* **2012**, *42* (1), 231–263.

(17) Bechert, D. W.; Bruse, M.; Hage, W. Experiments with Three-Dimensional Riblets as an Idealized Model of Shark Skin. *Exp. Fluids* **2000**, *28* (5), 403–412.

(18) Bixler, G. D.; Bhushan, B. Fluid Drag Reduction with Shark-Skin Riblet Inspired Microstructured Surfaces. *Adv. Funct. Mater.* **2013**, *23* (36), 4507–4528.

(19) Carman, M. L.; Estes, T. G.; Feinberg, A. W.; Schumacher, J. F.; Wilkerson, W.; Wilson, L. H.; Callow, M. E.; Callow, J. A.; Brennan, A. B. Engineered Antifouling Microtopographies--Correlating Wettability with Cell Attachment. *Biofouling* **2006**, *22* (1–2), 11–21.

(20) Schumacher, J. F.; Carman, M. L.; Estes, T. G.; Feinberg, A. W.; Wilson, L. H.; Callow, M. E.; Callow, J. A.; Finlay, J. A.; Brennan, A. B. Engineered Antifouling Microtopographies - Effect of Feature Size, Geometry, and Roughness on Settlement of Zoospores of the Green Alga Ulva. *Biofouling* **2007**, *23* (1–2), 55–62.

(21) Chung, K. K.; Schumacher, J. F.; Sampson, E. M.; Burne, R. A.; Antonelli, P. J.; Brennan, A. B. Impact of Engineered Surface Microtopography on Biofilm Formation of Staphylococcus Aureus. *Biointerphases* **2007**, *2* (2), 89–94.

(22) Schumacher, J. F.; Long, C. J.; Callow, M. E.; Finlay, J. A.; Callow, J. A.; Brennan, A. B. Engineered Nanoforce Gradients for Inhibition of Settlement (Attachment) of Swimming Algal Spores. *Langmuir* **2008**, *24* (9), 4931–4937.

(23) Reddy, S. T.; Chung, K. K.; McDaniel, C. J.; Darouiche, R. O.; Landman, J.; Brennan, A. B. Micropatterned Surfaces for Reducing the Risk of Catheter-Associated Urinary Tract Infection: An *In Vitro* Study on the Effect of Sharklet Micropatterned Surfaces to Inhibit Bacterial Colonization and Migration of Uropathogenic Escherichia Coli. *J. Endourol.* **2011**, *25* (9), 1547–1552.

(24) Li, Y.; Zhang, W.; Niu, J.; Chen, Y. Mechanism of Photogenerated Reactive Oxygen Species and Correlation with the Antibacterial Properties of Engineered Metal-Oxide Nanoparticles. *ACS Nano* **2012**, *6* (6), 5164–5173.

(25) Kubacka, A.; Diez, M. S.; Rojo, D.; Bargiela, R.; Ciordia, S.; Zapico, I.; Albar, J. P.; Barbas, C.; Martins dos Santos, V. A. P.; Fernandez-Garcia, M.; Ferrer, M. Understanding the Antimicrobial Mechanism of TiO_2-Based Nanocomposite Films in a Pathogenic Bacterium. *Sci. Rep.* **2014**, *4* 4134.

(26) Fu, G.; Vary, P. S.; Lin, C.-T. Anatase TiO_2 Nanocomposites for Antimicrobial Coatings. *J. Phys. Chem. B* **2005**, *109* (18), 8889–8898.

(27) Kühn, K. P.; Chaberny, I. F.; Massholder, K.; Stickler, M.; Benz, V. W.; Sonntag, H. G.; Erdinger, L. Disinfection of Surfaces by Photocatalytic Oxidation with Titanium Dioxide and UVA Light. *Chemosphere* **2003**, *53* (1), 71–77.

(28) Carp, O.; Huisman, C. L.; Reller, A. Photoinduced Reactivity of Titanium Dioxide. *Prog. Solid State Chem.* **2004**, *32* (1–2), 33–177.

(29) Hashimoto, K.; Irie, H.; Fujishima, A. A Historical Overview and Future Prospects. *AAPPS Bull.* **2007**, *17* (6), 12–28.

(30) Fujishima, A.; Rao, T. N.; Tryk, D. A. Titanium Dioxide Photocatalysis. *J. Photochem. Photobiol. C Photochem. Rev.* **2000**, *1* (1), 1–21.

(31) Beaulieu, M. R.; Hendricks, N. R.; Watkins, J. J. Large-Area Printing of Optical Gratings and 3D Photonic Crystals Using Solution-Processable Nanoparticle/Polymer Composites. *ACS Photonics* **2014**, *1* (9), 799–805.

(32) Kothari, R.; Beaulieu, M. R.; Hendricks, N. R.; Li, S.; Watkins, J. J. Direct Patterning of Robust 1-D, 2-D and 3-D Crystalline Metal Oxide Nanostructures Using Imprint Lithography and Nanoparticle Dispersion Inks. *Chem. Mater.* **2017**, *29*, 3908−3918.

(33) Moran, I. W.; Briseno, A. L.; Loser, S.; Carter, K. R. Device Fabrication by Easy Soft Imprint Nano-Lithography. *Chem. Mater.* **2008**, *20* (14), 4595–4601.

(34) Kolewe, K. W.; Peyton, S. R.; Schiffman, J. D. Fewer Bacteria Adhere to Softer Hydrogels. *ACS Appl. Mater. Interfaces* **2015**, *7* (35), 19562–19569.

(35) Rieger, K. A.; Cho, H. J.; Yeung, H. F.; Fan, W.; Schiffman, J. D. Antimicrobial Activity of Silver Ions Released from Zeolites Immobilized on Cellulose Nano Fi Ber Mats. *ACS Appl. Mater. Interfaces* **2016**, *8* (5), 3032–3040.

(36) Li, W.; Zhou, Y.; Howell, I. R.; Gai, Y.; Naik, A. R.; Li, S.; Carter, K. R.; Watkins, J. J. Direct Imprinting of Scalable , High-Performance Woodpile Electrodes for Three-Dimensional Lithium-Ion Nanobatteries. *ACS Appl. Mater. Interfaces* **2018**, *10* (6), 5447–5454.

(37) Guo, L. J. Nanoimprint Lithography: Methods and Material Requirements. *Adv. Mater.* **2007**, *19* (4), 495–513.

(38) Li, C.; Colella, N. S.; Watkins, J. J. Low-Temperature Fabrication of Mesoporous Titanium Dioxide Thin Films with Tunable Refractive Indices for One-Dimensional Photonic Crystals and Sensors on Rigid and Flexible Substrates. *ACS Appl. Mater. Interfaces* **2015**, *7* (24), 13180–13188.

(39) Chen, X.; Sun, J.; Shen, J. Patterning of Layer-by-Layer Assembled Organic-Inorganic Hybrid Films: Imprinting versus Lift-Off. *Langmuir* **2009**, *25* (5), 3316–3320.

(40) Watson, T.; Mabbett, I.; Hongxia, W.; Worsley, D. Ultrafast near Infrared Sintering of TiO_2 Layers on Metal Substrates for Dye-Sensitized Solar Cells. *Prog. Photovolt Res. Appl.* **2010**, *19*, 482–486.

(41) Hooper, K.; Carnie, M.; Charbonneau, C.; Watson, T. Near Infrared Radiation as a

Rapid Heating Technique for TiO_2 Films on Glass Mounted Dye-Sensitized Solar Cells. *Int. J. Photoenergy* **2014**, *2014* (1), 1–8.

(42) Jeevanandam, P.; Mulukutla, R. S.; Phillips, M.; Chaudhuri, S.; Erickson, L. E.; Klabunde, K. J. Near Infrared Reflectance Properties of Metal Oxide Nanoparticles. *J. Phys. Chem. C* **2007**, *111* (5), 1912–1918.

(43) Oliver, C.; Pharr, M. An Improved Technique for Determining Hardness and Elastic Modulus Using Load and Displacement Sensing Indentation Experiments. *Journal of Materials Research*. **1992**, *7* (6) 1564–1583.

(44) Oliver, W. C.; Pharr, G. M. Measurement of Hardness and Elastic Modulus by Instrumented Indentation: Advances in Understanding and Refinements to Methodology. *J. Mater. Res.* **2004**, *19* (1), 3–20.

(45) Long, C. J.; Schumacher, J. F.; Brennan, A. B. Potential for Tunable Static and Dynamic Contact Angle Anisotropy on Gradient Microscale Patterned Topographies. Langmuir **2009**, *25* (22), 12982–12989.

(46) Gao, L.; McCarthy, T. J. Contact Angle Hysteresis Explained. *Langmuir* **2006**, *22* (14), 6234–6237.

(47) Youngblood, J. P.; McCarthy, T. J. Ultrahydrophobic Polymer Surfaces Prepared by Simultaneous Ablation of Polypropylene and Sputtering of Poly(tetrafluoroethylene) Using Radio Frequency Plasma. *Am. Chem. Soc. Polym. Prepr. Div. Polym. Chem.* **1999**, *40* (2), 563–564.

(48) Ucar, I. O.; Cansoy, C. E.; Erbil, H. Y.; Pettitt, M. E.; Callow, M. E.; Callow, J. A. Effect of Contact Angle Hysteresis on the Removal of the Sporelings of the Green Alga *Ulva* from the Fouling-Release Coatings Synthesized from Polyolefin Polymers. *Biointerphases* **2010**, *5* (3), 75–84.

(49) Alexander, M. R.; Williams, P. Water Contact Angle Is Not a Good Predictor of Biological Responses to Materials. *Biointerphases* **2017**, *12* (2), 02C201.

(50) Dobosz, K. M.; Kolewe, K. W.; Schiffman, J. D. Green Materials Science and Engineering Reduces Biofouling: Approaches for Medical and Membrane-Based Technologies. *Front. Microbiol.* **2015**, *6* (196), 1–8.

(51) Song, F.; Koo, H.; Ren, D. Effects of Material Properties on Bacterial Adhesion and Biofilm Formation. *J Dent Res* **2015**, *94* (8), 1027–1034.

(52) Anselme, K.; Davidson, P.; Popa, A. M.; Giazzon, M.; Liley, M.; Ploux, L. The Interaction of Cells and Bacteria with Surfaces Structured at the Nanometre Scale. *Acta Biomater.* **2010**, *6* (10), 3824–3846.

(53) Schumacher, J. F.; Aldred, N.; Callow, M. E.; Finlay, J. A.; Callow, J. A.; Clare, A. S.; Brennan, A. B. Species-Specific Engineered Antifouling Topographies: Correlations between the Settlement of Algal Zoospores and Barnacle Cyprids.

Biofouling **2007**, *23* (5–6), 307–317.

(54) Perni, S.; Prokopovich, P. Micropatterning with Conical Features Can Control Bacterial Adhesion on Silicone. *Soft Matter* **2013**, *9* (6), 1844–1851.

(55) Whitehead, K. A.; Colligon, J.; Verran, J. Retention of Microbial Cells in Substratum Surface Features of Micrometer and Sub-Micrometer Dimensions. *Colloids Surfaces B Biointerfaces* **2005**, *41* (2–3), 129–138.

(56) Fujishima, A.; Zhang, X.; Tryk, D. A. TiO_2 Photocatalysis and Related Surface Phenomena. *Surf. Sci. Rep.* **2008**, *63* (12), 515–582.

(57) Benabbou, A. K.; Derriche, Z.; Felix, C.; Lejeune, P.; Guillard, C. Photocatalytic Inactivation of Escherischia Coli. Effect of Concentration of TiO_2 and Microorganism, Nature, and Intensity of UV Irradiation. *Appl. Catal. B Environ.* **2007**, *76* (3–4), 257–263.

(58) Matsunaga, T.; Tomoda, R.; Nakajima, T.; Wake, H. Photoelectrochemical Sterilization of Microbial Cells by Semiconductor Powders. *FEMS Microbiol. Lett.* **1985**, *29* (1–2), 211–214.

(59) Kubacka, A.; Serrano, C.; Ferrer, M.; Lunsdorf, H.; Bielecki, P.; Cerrada, M. L.; Fernandez-García, M.; Fernandez-García, M. High-Performance Dual-Action Polymer − TiO_2 Nanocomposite Films via Melting Processing. Nano Lett. **2007**, *7* (8), 2529–2534.

(60) Leyland, N. S.; Podporska-Carroll, J.; Browne, J.; Hinder, S. J.; Quilty, B.; Pillai, S. C. Highly Efficient F, Cu Doped TiO_2 Anti-Bacterial Visible Light Active Photocatalytic Coatings to Combat Hospital-Acquired Infections. *Sci. Rep.* **2016**, *6*, 24770.

(61) Page, K.; Wilson, M., Parkin, I. P. Antimicrobial Surfaces and Their Potential in Reducing the Role of the Inanimate Environment in the Incidence of Hospital-Acquired Infections. J. Mater. Chem. **2009**, *19*, 3819–3831.

CHAPTER 3

DIRECT PATTERNING OF BIOINSPIRED, PHOTOCATALYTIC, DURABLE, CERAMIC SURFACES WITH ANTIFOULING AND ANTIBACTERIAL ACTIVITY

3.1 Introduction

Healthcare-associated infections (HAIs),[1,2] which are the result of bacterial contamination on high-touch surfaces, are a significant challenge, causing 2 million infections and 23,000 deaths, as well as being responsible for additional billions of dollars in healthcare costs in the United States every year.[3] Typical hospital cleaning protocols only decrease bacterial contamination from 74% to 66%.[4] Antibiotics and disinfectants have been used to decrease bacterial contamination; however, the excessive use antibiotics has led to the increased resistance of bacteria to treatments.[5] Although there have been many efforts to reduce HAIs, there continues to be demand for high-performance, hard, antifouling, and antimicrobial coatings that are durable, non-toxic, and cost-effective.

Metallic materials have been widely studied for hard, durable, antimicrobial coatings.[6] Inorganic antibacterial coatings, such as those of copper, have been fabricated using electroless plating[7], cold spraying[8], and chemical vapor deposition[9]. Copper-based coatings contain a broad spectrum of antibacterial properties, thus are quite effective at killing bacteria; however, dead bacteria still adhere to the surface, conditioning the surface or masking the antibacterial surface chemistry and subsequently leading to biofilm formation. In addition, leakage of the active components limits the duration of antimicrobial activity and leads to environmental concerns. Moreover, it is often difficult to fabricate transparent coatings that contain metal additives.

Due to the toxicity of metals and their poor antimicrobial activity for long-term applications,[10] biocide-free approaches such as bacteria-release surfaces, micro/nano topographies, or biomimetic surfaces, have recently received attention.[11] For example, a bioinspired shark skin surface made from silicone, Sharklet AF™ effectively reduced the area coverage of zoospores, *Ulva*, *Staphylococcus aureus (S. aureus)* and *Escherichia coli (E. coli*) by up to 55-86% after a 24 h incubation period.[12–16] However, two main challenges still remain. First, the limited long-term mechanical durability of the soft patterned surfaces restricts their use on high-touch surfaces (i.e., hospital bed rails, door handles, etc). Second, although these coatings prevent the initial fouling of organisms, over a longer periods of time bacteria will accumulate. Thus, there is a need to develop multifunctional, antibacterial and antifouling coatings that are hard and wear-resistant and therefore more suitable for long-term, practical applications. One way to increase the hardness and improve the antimicrobial property of patterned surfaces is by incorporating functional inorganic nanoparticles within a hard matrix. Functional nanoparticles can be used as antibacterial agents as well as a means to improve mechanical properties.[17,18]

Doll *et al*. fabricated shark skin coatings in titanium using ultra-short pulse laser ablation.[19] They showed that micropatterned titanium surfaces reduced *S. aureus* area coverage significantly compared to smooth titanium surfaces. However, due to the high cost of laser ablation, it is not practical to implement laser-ablated microstructures in the production of large area coatings. On the other hand, soft nanoimprint lithography (NIL) offers a cost-effective, rapid, and scalable method compared to other current techniques, such as ion-beam etching and laser ablation. NIL enables imprinting of a wide range of materials such as polymers[20] and inorganic materials[21]. Recently, our group developed a

direct metal-oxide imprinting technique and has demonstrated its use for a variety of applications including optical[22,23] and battery[24,25] applications.

We fabricated hard, ceramic shark-skin-patterned surfaces using solvent-assisted soft NIL. While we previously reported titania and titania/polymer antimicrobial surfaces[17], here we use zirconium dioxide (ZrO_2) NPs to form the matrix its low-cost and the outstanding thermal, chemical, and wear-resistant characteristics of ZrO_2.[26] Non-toxic titanium dioxide (TiO_2) NPs were incorporated as an antibacterial agent for its excellent photocatalytic activity under a UV light exposure. TiO_2 containing coatings are transparent yet can inactivate a wide range of microorganism including Gram-positive/Gram-negative bacteria, fungi, and viruses.[27,28] Thus, orthogonal ZrO_2/TiO_2 (90 wt%/10 wt%) shark-skin microstructures were fabricated on glass substrates and sintered to obtain hard ceramic microstructures. Wettability, mechanical properties, antifouling, and antibacterial properties of ZrO_2/TiO_2 shark-skin-patterned surfaces were investigated. Scalable and low-cost photocatalytic hard ceramic shark-skin-patterned surfaces offer durable, light-assisted antimicrobial coatings for practical applications.

3.2 Experimental section

3.2.1 Materials

All materials were used as received without further purification. Zirconium dioxide nanoparticles (ZrO_2 NPs, 50wt% in ethanol (EtOH)) with an average diameter of 5 nm) were purchased from Pixelligent (Baltimore, MD). Titanium dioxide (TiO_2, anatase phase) NPs (5-30 nm diameter), 15 wt% dispersion in water, were purchased from Nanostructured & Amorphous Materials Inc. (Houston, TX). N-methyl-2-pyrrolidone (NMP, ReagentPlus 99%), EtOH, 1, 2 Propanediol, M9 minimal salts (M9 media), and phosphate buffered

saline (PBS, 10× sterile biograde) were purchased from Sigma-Aldrich (St. Louis, MO). Methanol (MeOH) and poly(tetrafluoroethylene) (PTFE) filters (0.45 μm) were purchased from Fisher Scientific (Hampton, NH). Heptadecafluoro-1,1,2,2-tetrahydrodecyl)dimethylchlorosilane was acquired from Gelest (Morrisville, PA). Sylgard 184 silicone elastomer kit (polydimethylsiloxane (PDMS)) was purchased from Dow Corning (Midland, MI).

3.2.2 Methods

Preparation of ZrO_2/TiO_2 Nanoparticle (NP) Dispersion Ink

ZrO_2 NPs were diluted to 30 wt% ZrO_2 with EtOH and diluted further to 24 wt% with 1,2 propanediol. The ZrO_2/TiO_2 NP composite dispersion was prepared to achieve a 10 wt% TiO_2 loading to solid content. TiO_2 NPs were used from a stock dispersion (14 wt% in NMP/MeOH) that was solvent-exchanged from a water dispersion (15 wt% in water). The detailed solvent-exchange procedure is in our previous publication.[22] The ZrO_2/TiO_2 dispersion was sonicated for 10 min and a stable, 22.5 wt% NP dispersion was obtained.

Fabrication of PDMS mold and ZrO_2/TiO_2 Shark Skin Microstructures

To prepare PDMS molds, Sylgard 184 was mixed in a 1:10 ratio of curing agent to base,[29] then poured onto a Sharklet AF™ nickel (height: 3 μm, width: 2 μm, pitch: 4 μm) master mold (provided by Sharklet Technologies), and placed into an oven to be crosslinked at 70 °C for 3 h.

The ZrO_2/TiO_2 NP dispersion was spin-coated onto a glass substrate to form a 700 nm film. The inverse Sharklet PDMS mold was placed onto the still-wet, spin-coated film. As the remaining solvent evaporates through the mold, the rigid shark skin structures were

formed. The stamp/substrate assembly was placed on a hot plate (~50 °C) for 5-10 min. The PDMS mold was peeled off and ZrO_2/TiO_2 composite microstructures were obtained. After the imprinting step, ZrO_2/TiO_2 shark-skin-patterned surfaces were sintered at a variety of temperatures (300 °C to 1000 °C) to obtain hard ceramic structures. Here, ZrO_2/TiO_2 shark skin structures and smooth films were prepared on a glass substrate and sintered at 500 °C for 2 h and cooled to room temperature over 2 h and then used for further experiments.

Parylene HT conformal coating

Parylene HT, also named AF-4 (poly(α, α, α′, α′-tetrafluoro-para-xylylene) conformal coating was conducted on the ZrO_2/TiO_2 shark-skin-patterned surfaces and smooth films by Specialty Coating Systems (Indianapolis, IN, USA). Before coating, samples were treated with an adhesion promoter (AdPro PlusVR , SCS).

3.2.3 Characterization and Evolution of Shark Skin Microstructures

3.2.3.1. Characterization:

The 22.5 wt% ZrO_2/TiO_2 NP dispersion was diluted with EtOH and drop casted on a carbon coated copper grids for transmission electron microscopy (TEM) imaging. TEM was performed in bright fi eld imaging mode using a JEOL 2000 FX. TEM was operated at an accelerating voltage of 200 kV. Scanning electron microscopy (SEM) was performed on a fi eld emission scanning electron microscope (Magellan 400). 3D optical profilometry (Zygo, Nexview) was used to measure feature dimensions. The thickness of Parylene HT was determined by SEM cross-section imaging. Contact angle measurements were acquired using a VCA Optima surface analysis/goniometry system. Advancing and

receding water contact angles were determined using 6 independent measurements on different samples from parallel and perpendicular directions to features (5 μL of water drop was used) at room temperature. To measure the mechanical properties of ZrO_2/TiO_2, the dispersion was spin coated into 800 nm films on silicon wafers. Films of Parylene HT (25 μm thick) were used to measure the hardness and reduced modulus properties of Parylene HT using a Hysitron TriboIndenter (TI 950) by averaging 30 indentations obtained under rate control (10 μN/s) using a Berkovich tip (100 nm) for each film. Indentation depth was kept less than 10% of the film thickness to prevent substrate effects. Significant difference was determined by analysis of variance (ANOVA) with Tukey test. Values of $p<0.05$ was considered to be significant.

3.2.3.2. Antifouling Performance

The fouling resistance of shark-skin patterned composites, as well as smooth surface control samples were evaluated with a bacterial attachment assay using the model bacteria, *Escherichia coli* K12 MG1655 (*E. coli*, expressing green fluorescent protein).[30] *E. coli* was cultured overnight in Luria-Bertani broth (Sigma-Aldrich) then washed and re-suspended in M9 media to a final concentration of 1×10^8 cells/mL. Samples and controls were placed at the base of separate wells in 6-well polystyrene plates (Fisher Scientific) and inoculated with 5 mL of *E. coli* suspended in M9 media. Following a 24 h incubation period at 37 ºC, the growth media was removed using a sterilized glass pipette and samples were rinsed repeatedly with PBS before analysis. Samples were analyzed using a Zeiss Microscope Axio Imager A2M (20× and 50× magnification, Thornwood, NY). The surface area coverage of attached bacteria was quantified by analyzing 10–15 randomly acquired

images over at least three parallel replicates using *ImageJ* 1.45 software (National Institutes of Health, Bethesda, MD).

3.2.3.3. Antibacterial Activity

The antibacterial activity of the TiO_2 containing samples was evaluated using a using a standard antibacterial assay modified to enable exposure of the samples to UV light.[31] Smooth ZrO_2/TiO_2 films were evaluated in parallel with TiO_2-free ZrO_2 control samples and glass slides. The samples were placed at the base of separate wells in 6-well polystyrene plates to which 5 mL of M9 media containing *E. coli* (1×10^8 cells/mL) were added before incubating for 1 h at 37 °C under UV light (F15W/T8 McMaster-Carr, 15W 365 nm wavelength). The samples were held at a 15 cm fixed distance from the UV source. UV light intensity was measured using a UV light meter (Thorlabs GM10HS, Hamamatsu S2281 probe) and determined to be 1.0 mW/cm^2. Following photoactivation, the samples were removed and stained with propidium iodide (PI) for 15 min to identify the dead cells before being throughly washed with PBS to remove excess stain. The loss of viability was visualized using a Zeiss Microscope Axio Imager A2M, quantified using *ImageJ* software, and the percentage of dead cells (or loss of viability) was calculated from the ratio of the number of cells stained with PI divided by the total number of cells.[31]

3.3 Results and Discussion

3.3.1 Fabrication of ZrO_2/TiO_2 Shark Skin Patterned Surfaces

To imprint ceramic, shark-skin-patterned surfaces via solvent-assisted NIL, the ink needs to be optimized to ensure NPs are well-dispersed in a mixture of solvents with low

and high volatilities. The highly volatile solvent provides fast film formation during spin-coating while the low-volatility solvent evaporates slowly, giving sufficient time for the imprinting process. ZrO_2 NPs (50 wt% in EtOH) were diluted with EtOH (30 wt% ZrO_2) and then with 1,2 propanediol (1,2PD) to obtain 24 wt% ZrO_2 NPs in an EtOH/1,2PD solvent mixture. The TiO_2 NP dispersion (14 wt%) was mixed with the ZrO_2 NP dispersion (24 wt% in EtOH/1,2PD) to achieve a 10 wt% TiO_2 loading relative to total solids. Thus, a stable 90 wt% ZrO_2/10 wt% TiO_2 (ZrO_2/TiO_2) composite dispersion was prepared. The size of the NPs were determined to be 5.8 ± 0.8 nm in TEM (**Figure 3.1a)**. Dynamic light scattering (DLS) shows that the particle size distribution is between 5-40 nm, which indicates that the ZrO_2 NPs forms tiny clusters in the solvent system (**Figure 3.1b)**.

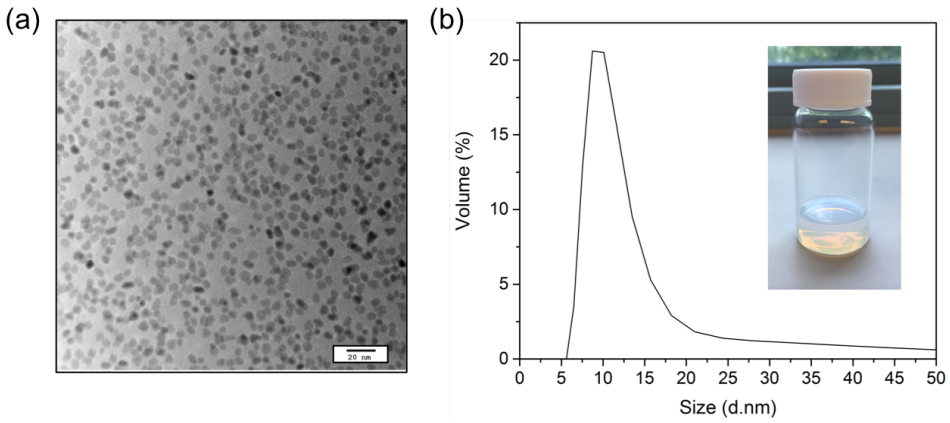

Figure 3.1. (a) TEM image of ZrO_2/TiO_2 NPs, (b) DLS measurement of ZrO_2/TiO_2 nanoparticles size distribution, digital image of the ZrO_2/TiO_2 ink.

Shark-skin-patterned surfaces were fabricated using ZrO_2/TiO_2 NP dispersion via solvent-assisted NIL,[22,32] scheme is shown in **Figure 3.2**. First, a soft PDMS mold was replicated from a nickel Sharklet AF^{TM} master mold. The nickel master mold consists of 2 µm width and 3 µm height riblets, with different lengths ranging from 4-16 µm, separated by a fixed 2 µm distance between features. The ZrO_2/TiO_2 NP dispersion was spin-coated

onto a glass substrate and the PDMS mold was placed onto the spin-coated film containing residual solvents, which provides enough fluidity to allow capillary forces to drive the nanoparticles into the mold.[24,32] As the solvent evaporated through the mold, rigid shark skin microstructures were formed in a few minutes. Then, the PDMS stamp was peeled off and ceramic ZrO_2/TiO_2 composite microstructures were obtained. After the imprinting process, ZrO_2/TiO_2 shark skin films were sintered at 500°C for 2 h to obtain hard, ceramic, shark-skin-patterned surfaces.

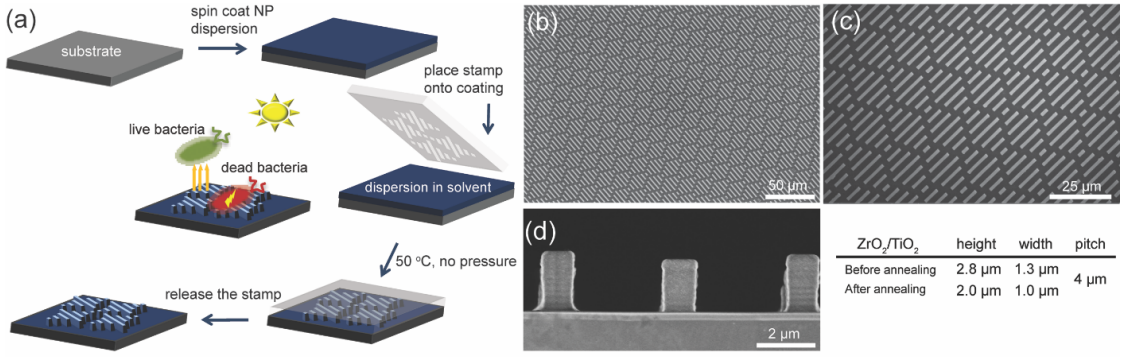

Figure 3.2. (a) Schematic representation of the fabrication process of ZrO2/TiO2 shark-skin-patterns using soft PDMS stamp, SEM micrographs of ZrO2/TiO2 shark-skin-patterned surfaces (b) ZrO_2/TiO_2 shark-skin-patterned surface, low magnification (top view), (c) ZrO_2/TiO_2 shark-skin-patterned surface, higher magnification (top view), (d) Cross section image of shark-skin-patterned surface after annealing at 500 °C.

SEM micrographs and the feature dimensions of the ZrO_2/TiO_2 shark-skin-patterned surfaces are shown in **Figure 3.2 and Figure 3.3**. The features were successfully replicated uniformly in size and shape over a large area, which was limited by the size of the stamp. Direct imprinting of NPs offers some advantages over imprinting sol-gel precursors. The transition from the sol to gel phase results in a height reduction up to approximately 60%, and subsequent calcination to obtain crystalline NPs results in additional height reduction (~80%), which causes unstable nano/micro structures and cracks formation.[21,33–35] Herein, ZrO_2/TiO_2 shark-skin-patterned surfaces had only 33%

shrinkage in height compared to height of the master mold. The shrinkage is due to solvent that drives the imprinting process and post heat treatment. As the solvent evaporated through the stamp, crystalline NPs pack firmly and results in empty space between the mold and NPs. Before sintering the patterned surfaces, shrinkage in height was 7% (**Figure 3.3**). After sintering the patterned shark skin film at 500°C, 29% shrinkage was observed in the height of the ZrO_2/TiO_2 shark-skin-patterned surfaces (**Figure 3.2d**).

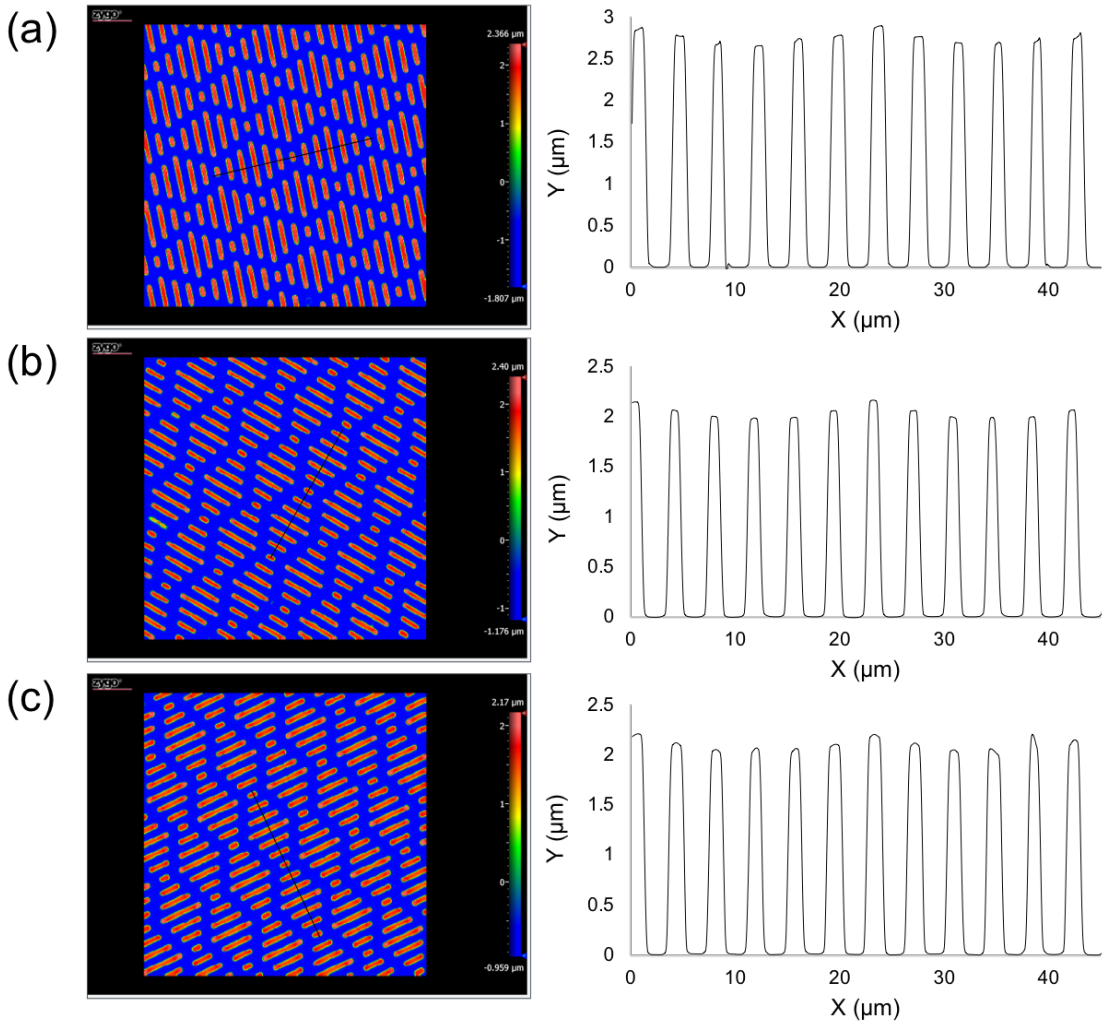

Figure 3.3. Optical profilometry images and height profile of (a) the ZrO_2/TiO_2 before annealing and (b) the ZrO_2/TiO_2 after annealing, (c) Parylene HT coated ZrO_2/TiO_2.

Hardness and reduced modulus of the smooth films of ZrO_2/TiO_2 were characterized as a function of temperature after sintering at 300, 500, 750, and 1000 °C using nanoindentation, shown in **Figure 3.4**. After sintering the ZrO_2/TiO_2 film at 500 °C, the hardness and modulus of the ZrO_2/TiO_2 coating significantly increased from 0.61 ± 0.03 GPa and 18 ± 2 GPa to 3.7 ± 0.4 GPa and 88 ± 9 GPa, respectively. Moreover, the hardness and modulus increased significantly up to 13 ± 2 GPa and 160 ± 7 GPa, respectively when sintered at 1000 °C. The glass substrates were durable up to 500 °C, so the experiments were continued with sintered smooth and shark skin patterned surfaces at 500 °C. Typical shark-skin patterned surfaces are made of PDMS[14], which has very low hardness (H) and modulus (E_r) (H= ~0.2-0.5 MPa and E_r=~1.7–3.0 MPa)[36,37], so they easily wear and can only be used for limited amounts of time. By contrast, the excellent mechanical properties of the ZrO_2/TiO_2 shark-skin-patterned surfaces combined with their self-cleaning nature imparted by the photocatalytic activity of TiO_2 NPs suggests that these surfaces will be durable and functional over extended periods of time.

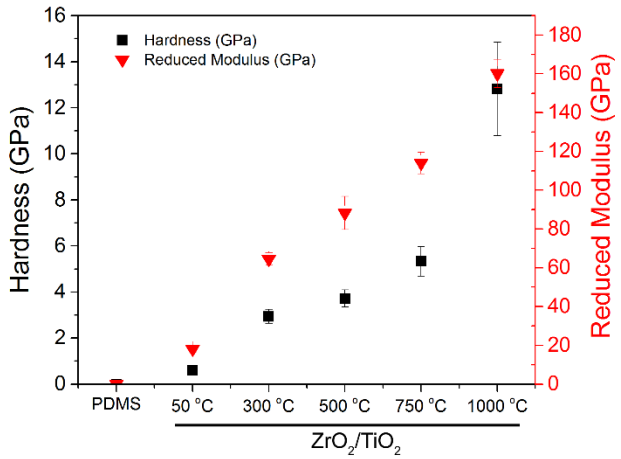

Figure 3.4. Nanoindentation analysis of PDMS[37], ZrO2/TiO2 film before and after annealing at 300°C, 500°C, 750°C, and 1000°C. Hardness and reduced modulus of the films are given.

To determine the wettability of shark-skin-patterned surfaces, advancing and receding water contact angles were measured and are shown in **Table 3.1**. The hydrophilic or hydrophobic characteristics of surfaces can be influenced by using rough and/or patterned surfaces.[38–40] Our ZrO_2/TiO_2 shark-skin-patterned surfaces displayed superhydrophilic behavior with a water contact angle of less than 5°, while the smooth ZrO_2/TiO_2 film had 31 ± 1° advancing and 16 ± 2° receding contact angle. Thus, we obtained superhydrophilic shark-skin-patterned surfaces using a hydrophilic ZrO_2/TiO_2 NPs. Superhydrophilic surfaces have been used as antifouling surfaces and their performance is explained in part by the presence of a water layer that prevents the adhesion of cells to the surface.[36,41,42] In our previous study,[17] we demonstrated that hydrophobic shark-skin-patterned surfaces also had great antifouling performance although they had a high contact angle hysteresis (~101°). Overall, both superhydrophilic and hydrophobic shark skin patterned surfaces exhibited excellent bacteria release performances despite their different wettability characteristics.[43,44] These results suggest that shark-skin-patterned surfaces can be modified with different chemistries and be used for functional devices while maintaining their bacteria resistant characteristics.

Table 3.1. Wetting analysis of ZrO_2/TiO_2 smooth and shark-skin-patterned surfaces. Standard deviation is displayed.

	Advancing Water Contact Angle	Receding Water Contact Angle
ZrO_2/TiO_2 (smooth)	31 ± 1°	16 ± 2°
ZrO_2/TiO_2 (shark-skin)	Less than 5 °	Less than 5 °

3.3.2 Antifouling and Antibacterial Activity

The antifouling activity of shark-skin-patterned surfaces was evaluated after 24 h using *E. coli*, a model Gram-negative bacteria, (**Figure 3.5**). The ZrO_2/TiO_2 shark-skin-patterned surfaces displayed surface area coverage of $0.20 \pm 0.05\%$. ZrO_2/TiO_2 shark-skin-patterned surfaces showed a decrease in bacterial attachment up to 95% compared to an uncoated glass substrate and 85% compared to smooth ZrO_2/TiO_2 films.

The antibacterial activity of the ZrO_2/TiO_2 smooth films was tested using the model bacteria, *E. coli* (**Figure 3.6**). The tests were performed under a UV lamp (365 nm) with an intensity of 1.0 mW/cm^2. The control sample, ZrO_2/TiO_2 under dark, showed only baseline inactivation, ~ 5% killing after 1 h. The ZrO_2/TiO_2 composite films showed significant antibacterial activity with 82 ± 2 % lethality for *E.coli* after 1 h UV light illumination. The excellent antibacterial performance of ZrO_2/TiO_2 films under the low UV dose is a result of the high photocatalytic activity of the high surface area, small TiO_2 NPs (8-15 nm). This antibacterial activity of TiO_2 is due to formation of hydroxyl radicals upon light irritation in the presence of water. The photocatalytic activity of TiO_2 in turn depends on several criteria including particle size, the crystalline phase of the NPs, and UV dose.[28] Here, sintering of ZrO_2/TiO_2 NPs was conducted at 500 °C. Although sintering at this temperature may have resulted in some transition from the anatase to the less-catalytic rutile phase of TiO_2, we expect that impact of low levels of the transition on the antimicrobial properties of the surface to be negligible. However, the phase of NPs is not the only criteria to obtain best performance.[45] For example, Degussa P-25 has a great photocatalytic activity due to high surface area despite having 80 % anatase and 20 % rutile phases.[46] Overall, 10 wt% TiO_2 NP incorporation resulted in excellent antibacterial activity in 1 h with a very low UV dose.

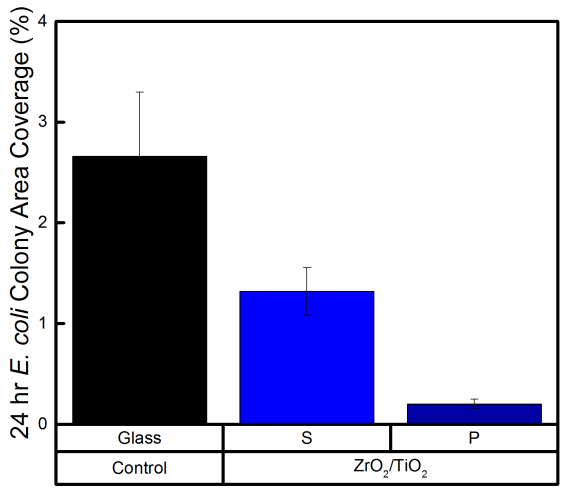

Figure 3.5. Representative micrographs of E. coli attached to after a 24 hr incubation period on a flat ZrO2/TiO2 surface (ZrO2 S), shark skin patterned ZrO2/TiO2 surfaces (ZrO2 P). There was a significant reduction in bacterial adhesion on patterned surfaces (P) in comparison to smooth surfaces (S). Error bars denote standard error. One asterisk (*) indicates that values are significantly different at 0.05 level and two asterisks (**) indicates that values are significantly different at 0.01 level.

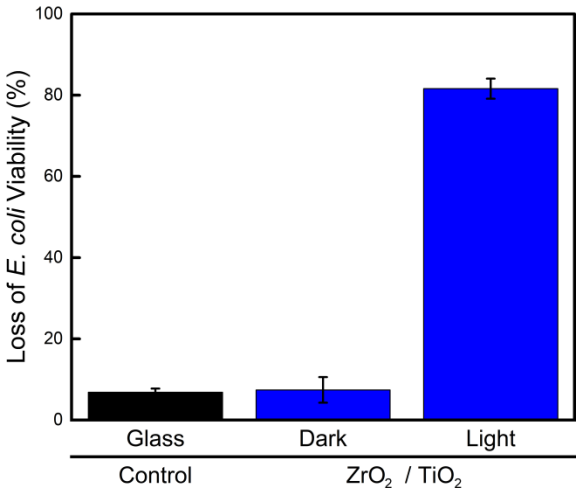

Figure 3.6. Loss of E. coli viability after 1 hr UV-exposure to films containing TiO_2 exhibited excellent antimicrobial functionality, with 82% killing efficiency. Control glass surfaces (no TiO_2) and ZrO_2/TiO_2 "dark" control displayed less than 7% killing. Error bars denote standard error.

3.3.3 Parylene HT-Coated Shark-Skin-Patterned Surfaces

ZrO_2/TiO_2 shark-skin-patterned surfaces were coated conformally with a layer of Parylene HT, which known as gold-standard antifouling coating and widely used in medical devices.[47] Parylene HT conformal coating was conducted by Specialty Coating Systems, Inc. using chemical vapor deposition (CVD) onto the shark skin microstructures as 145 nm in thickness. SEM micrographs of Parylene HT-coated ZrO_2/TiO_2 shark-skin-patterned surfaces are shown in **Figure 3.7.** Hardness and reduced modulus of Parylene HT were determined to be 0.3 ± 0.1 GPa and 2.6 ± 0.4 GPa, respectively. Parylene HT is a hard polymer and relatively easy to make a conformal coating compared to other types of antifouling coatings such as PDMS and polyethylene glycol (PEG).

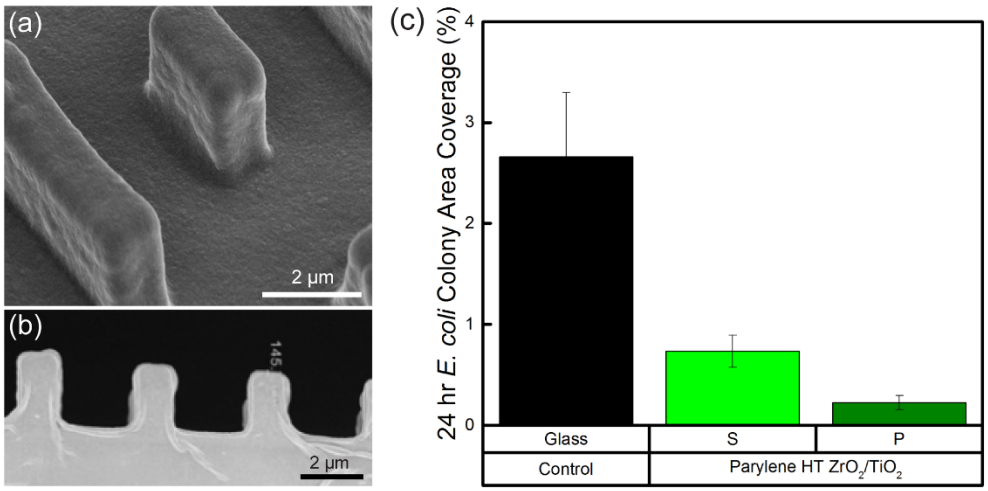

	Hardness (GPa)	Reduced Modulus (GPa)	Advancing Contact Angle (°)	Receding Contact Angle (°)
Parylene HT (S)	0.3 ± 0.1	2.6 ± 0.4	104 ± 3	75 ± 1
Parylene HT (P)			155 ± 4	51 ± 3

Figure 3.7. SEM micrographs of Parylene HT coated ZrO_2/TiO_2 shark-skin-patterned surfaces (a) top view, (b) cross section, (c) Representative micrographs of *E. coli* attached to after a 24 hr incubation period on a smooth Parylene HT coated ZrO_2/TiO_2 surface (S), Parylene HT coated shark-skin-patterned ZrO_2/TiO_2 surfaces (P).

Parylene-HT conformal coated shark-skin-patterned surfaces had hydrophobic surface with 155 ± 4° and 51 ± 3° advancing and receding contact angles, respectively (**Figure 3.7**). Parylene HT-coated ZrO_2/TiO_2 shark-skin-patterned surfaces displayed surface area coverages of 0.22 ± 0.07% after 24 h *E. coli* incubation. Parylene HT-coated shark-skin-patterned surfaces decreased the bacterial attachment up to 70% compared to Parylene HT smooth films. Despite different surface wettability of the ZrO_2/TiO_2 and Parylene HT-coated ZrO_2/TiO_2 shark-skin surfaces (superhydrophilic versus hydrophobic), both decreased the bacterial attachment significantly compared to smooth films, which supported our previous study that the antifouling performance of shark-skin-patterned surfaces are not directly linked with surface wettability characteristics.[17,48] Although Parylene HT-coated shark-skin-patterned surface reduced the bacterial attachment

significantly compared to smooth Parylene HT films, in the long term, the bacteria can still form a biofilm on the engineered Parylene HT surfaces; thus, a killing mechanism is still needed to inactivate the settled microbes.[14] In the future, Parylene HT-coated shark-skin-patterned surfaces can be modified with desired enzymes, antibacterial biomolecules and be used as functional biosensors or medical implants.

3.4 Conclusions

In summary, we have fabricated hard, ZrO_2/TiO_2 ceramic, shark-skin-patterned surfaces possessing both antifouling and antibacterial functionality using a simple and cost-effective patterning technique. Moreover, superhydrophilic shark skin patterned surfaces were obtained with less than 5° water contact angle. The hardness and reduced modulus of the ZrO_2/TiO_2 films were increased to 13 GPa and 160 GPa, respectively. The shark-skin-patterned surfaces reduced the attachment of *E. coli* by 85-95% and killed 80% of *E. coli* after 1 h of UV light exposure. In addition, conformal Parylene-HT coated shark-skin-patterned surfaces reduced the attachment of *E. coli* by 70% compared to smooth antifouling Parylene-HT surfaces. Both the excellent antimicrobial performance and the superior mechanical properties of these ZrO_2/TiO_2 ceramic, shark-skin-patterned surfaces will provide durability and functionality over the long term.

3.5 References

(1) Carling, P. C.; Briggs, J.; Hylander, D.; Perkins, J. An Evaluation of Patient Area Cleaning in 3 Hospitals Using a Novel Targeting Methodology. *Am. J. Infect. Control* **2006**, *34* (8), 513–519.

(2) Weber, D. J.; Rutala, W. A.; Miller, M. B.; Huslage, K.; Sickbert-Bennett, E. Role of Hospital Surfaces in the Transmission of Emerging Health Care-Associated Pathogens: Norovirus, Clostridium Difficile, and Acinetobacter Species. *Am. J.*

Infect. Control **2010**, *38* (5 SUPPL.), S25–S33.

(3) CDC. *Antibiotic Resistance Threats in the United States, 2013*; 2013.

(4) French, G. L.; Otter, J. A.; Shannon, K. P.; Adams, N. M. T.; Watling, D.; Parks, M. J. Tackling Contamination of the Hospital Environment by Methicillin-Resistant Staphylococcus Aureus</Em> (MRSA): A Comparison between Conventional Terminal Cleaning and Hydrogen Peroxide Vapour Decontamination. *J. Hosp. Infect.* **2018**, *57* (1), 31–37.

(5) Stewart, P. S.; Costerton, J. W. Antibiotic Resistance of Bacteria in Biofilms. *Lancet* **2001**, *358* (9276), 135–138.

(6) Reddy, M. C. C. G. S.; Nadagouda, M. N. Antimicrobial and Anticorrosive Efficacy of Inorganic Nanoporous Surfaces. *Clean Technol. Environ. Policy* **2017**, *19* (3), 845–857.

(7) Yu, Z. J.; Kang, E. T.; Neoh, K. G. Electroless Plating of Copper on Polyimide Films Modified by Surface Grafting of Tertiary and Quaternary Amines Polymers. *Polymer (Guildf).* **2002**, *43* (15), 4137–4146.

(8) Sanpo, N.; Ang, S. M.; Cheang, P.; Khor, K. a. Antibacterial Property of Cold Sprayed Chitosan-Cu/Al Coating. *J. Therm. Spray Technol.* **2009**, *18* (December), 600–608.

(9) Ozkan, E.; Crick, C. C.; Taylor, A.; Allan, E.; Parkin, I. P. Copper-Based Water Repellent and Antibacterial Coatings by Aerosol Assisted Chemical Vapour Deposition. *Chem. Sci.* **2016**, *7* (8), 5126–5131.

(10) Hartleb, W.; Saar, J. S.; Zou, P.; Lienkamp, K. Just Antimicrobial Is Not Enough: Toward Bifunctional Polymer Surfaces with Dual Antimicrobial and Protein-Repellent Functionality. *Macromol. Chem. Phys.* **2016**, *217* (2), 225–231.

(11) Scardino, A. J.; de Nys, R. Mini Review: Biomimetic Models and Bioinspired Surfaces for Fouling Control. *Biofouling* **2011**, *27* (1), 73–86.

(12) Carman, M. L.; Estes, T. G.; Feinberg, A. W.; Schumacher, J. F.; Wilkerson, W.; Wilson, L. H.; Callow, M. E.; Callow, J. a; Brennan, A. B. Engineered Antifouling Microtopographies--Correlating Wettability with Cell Attachment. *Biofouling* **2006**, *22* (1–2), 11–21.

(13) Schumacher, J. F.; Carman, M. L.; Estes, T. G.; Feinberg, A. W.; Wilson, L. H.; Callow, M. E.; Callow, J. a; Finlay, J. a; Brennan, A. B. Engineered Antifouling Microtopographies - Effect of Feature Size, Geometry, and Roughness on Settlement of Zoospores of the Green Alga Ulva. *Biofouling* **2007**, *23* (1–2), 55–62.

(14) Chung, K. K.; Schumacher, J. F.; Sampson, E. M.; Burne, R. a; Antonelli, P. J.; Brennan, A. B. Impact of Engineered Surface Microtopography on Biofilm Formation of Staphylococcus Aureus. *Biointerphases* **2007**, *2* (2), 89–94.

(15) Schumacher, J. F.; Long, C. J.; Callow, M. E.; Finlay, J. a.; Callow, J. a.; Brennan, A. B. Engineered Nanoforce Gradients for Inhibition of Settlement (Attachment) of Swimming Algal Spores. *Langmuir* **2008**, *24* (9), 4931–4937.

(16) Reddy, S. T.; Chung, K. K.; McDaniel, C. J.; Darouiche, R. O.; Landman, J.; Brennan, A. B. Micropatterned Surfaces for Reducing the Risk of Catheter-Associated Urinary Tract Infection: An *In Vitro* Study on the Effect of Sharklet Micropatterned Surfaces to Inhibit Bacterial Colonization and Migration of Uropathogenic Escherichia Coli. *J. Endourol.* **2011**, *25* (9), 1547–1552.

(17) Arisoy, F. D.; Kolewe, K. W.; Homyak, B.; Kurtz, I. S.; Schi, J. D.; Watkins, J. J. Bioinspired Photocatalytic Shark-Skin Surfaces with Antibacterial and Antifouling Activity via Nanoimprint Lithography. *ACS Appl. Mater. Interfaces* **2018,** 10 (23), 20055–20063.

(18) Díez-Pascual, A. M.; Díez-Vicente, A. L. Nano-TiO2 Reinforced PEEK/PEI Blends as Biomaterials for Load-Bearing Implant Applications. *ACS Appl. Mater. Interfaces* **2015**, *7* (9), 5561–5573.

(19) Doll, K.; Fadeeva, E.; Stumpp, N. S.; Grade, S.; Chichkov, B. N.; Stiesch, M. Reduced Bacterial Adhesion on Titanium Surfaces Micro-Structured by Ultra-Short Pulsed Laser Ablation. *BioNanoMaterials* **2016**, *17* (1–2), 53–57.

(20) Guo, L. J. Nanoimprint Lithography: Methods and Material Requirements. *Adv. Mater.* **2007**, *19* (4), 495–513.

(21) Hampton, M. J.; Williams, S. S.; Zhou, Z.; Nunes, J.; Ko, D. H.; Templeton, J. L.; Samulski, E. T.; DeSimone, J. M. The Patterning of Sub-500 Nm Inorganic Oxide Structures. *Adv. Mater.* **2008**, *20* (14), 2667–2673.

(22) Beaulieu, M. R.; Hendricks, N. R.; Watkins, J. J. Large-Area Printing of Optical Gratings and 3D Photonic Crystals Using Solution-Processable Nanoparticle/Polymer Composites. *ACS Photonics* **2014**, *1* (9), 799–805.

(23) Li, S.; Kazemi-moridani, A.; Zhou, Y.; Howell, I. R.; Kothari, R.; Lee, J.; Watkins, J. J. Wavelength-Selective Three-Dimensional Thermal Emitters via Imprint Lithography and Conformal Metallization. **2018**, 10 (9), 8173–8179.

(24) Li, W.; Zhou, Y.; Howell, I. R.; Gai, Y.; Naik, A. R.; Li, S.; Carter, K. R.; Watkins, J. J. Direct Imprinting of Scalable , High-Performance Woodpile Electrodes for Three-Dimensional Lithium-Ion Nanobatteries. *ACS Appl. Mater. Interfaces* **2018**, *10* (6), 5447–5454.

(25) Li, W.; Christiansen, T. L.; Li, C.; Zhou, Y.; Fei, H.; Mamakhel, A.; Iversen, B. B.; Watkins, J. J. High-Power Lithium-Ion Microbatteries from Imprinted 3D Electrodes of Sub-10 Nm LiMn2O4/Li4Ti5O12 Nanocrystals and a Copolymer Gel Electrolyte. *Nano Energy* **2018**, 52, 431–440.

(26) Zhang, W.; Ji, G.; Bu, A.; Zhang, B. Corrosion and Tribological Behavior of ZrO2

Films Prepared on Stainless Steel Surface by the Sol-Gel Method. *ACS Appl. Mater. Interfaces* **2015**, *7* (51), 28264–28272.

(27) Kubacka, A.; Diez, M. S.; Rojo, D.; Bargiela, R.; Ciordia, S.; Zapico, I.; Albar, J. P.; Barbas, C.; Martins dos Santos, V. A. P.; Fernandez-Garcia, M.; Ferrer, M. Understanding the Antimicrobial Mechanism of TiO2-Based Nanocomposite Films in a Pathogenic Bacterium. *Sci. Rep.* **2014**, *4*.

(28) Fu, G.; Vary, P. S.; Lin, C.-T. Anatase TiO2 Nanocomposites for Antimicrobial Coatings. *J. Phys. Chem. B* **2005**, *109* (18), 8889–8898.

(29) Moran, I. W.; Briseno, A. L.; Loser, S.; Carter, K. R. Device Fabrication by Easy Soft Imprint Nano-Lithography. *Chem. Mater.* **2008**, *20* (14), 4595–4601.

(30) Kolewe, K. W.; Peyton, S. R.; Schiffman, J. D. Fewer Bacteria Adhere to Softer Hydrogels. *ACS Appl. Mater. Interfaces* **2015**, *7* (35), 19562–19569.

(31) Rieger, K. A.; Cho, H. J.; Yeung, H. F.; Fan, W.; Schi, J. D. Antimicrobial Activity of Silver Ions Released from Zeolites Immobilized on Cellulose Nano Fi Ber Mats. **2016**, *8* (5), 3032–3040.

(32) Kothari, R.; Beaulieu, M. R.; Hendricks, N. R.; Li, S.; Watkins, J. J. Direct Patterning of Robust 1-D, 2-D and 3-D Crystalline Metal Oxide Nanostructures Using Imprint Lithography and Nanoparticle Dispersion Inks. *Chem. Mater.* **2017**, *29*, 3908−3918.

(33) Ganesan, R.; Dumond, J.; Saifullah, M. S. M.; Lim, S. H.; Hussain, H.; Low, H. Y. Direct Patterning of TiO2 Using Step-and-Flash Imprint Lithography. *ACS Nano* **2012**, *6* (2), 1494–1502.

(34) Li, M.; Tan, H.; Chen, L.; Wang, J.; Chou, S. Y. Large Area Direct Nanoimprinting of SiO2–TiO2 Gel Gratings for Optical Applications. *J. Vac. Sci. Technol. B Microelectron. Nanom. Struct.* **2003**, *21* (2), 660–663.

(35) Park, H. H.; Zhang, X.; Lee, S. W.; Kim, K. D.; Choi, D. G.; Choi, J. H.; Lee, J. Y.; Lee, E. S.; Park, H. H.; Hill, R. H.; Jeong, J. H. Facile Nanopatterning of Zirconium Dioxide Films via Direct Ultraviolet-Assisted Nanoimprint Lithography. *J. Mater. Chem.* **2011**, *21* (3), 657–662.

(36) Krishnan, S.; Wang, N.; Ober, C. K.; Finlay, J. A.; Callow, M. E.; Callow, J. A.; Hexemer, A.; Sohn, K. E.; Kramer, E. J.; Fischer, D. A. Comparison of the Fouling Release Properties of Hydrophobic Fluorinated and Hydrophilic PEGylated Block Copolymer Surfaces: Attachment Strength of the Diatom Navicula and the Green Alga Ulva. *Biomacromolecules* **2006**, *7* (5), 1449–1462.

(37) Ma, P.; Xu, Z.; Wang, M.; Lu, L.; Yin, M.; Chen, X.; Li, D.; Ren, W. Fast Fabrication of TiO2hard Stamps for Nanoimprint Lithography. *Mater. Res. Bull.* **2017**, *90*, 253–259.

(38) Dou, X. Q.; Zhang, D.; Feng, C.; Jiang, L. Bioinspired Hierarchical Surface Structures with Tunable Wettability for Regulating Bacteria Adhesion. *ACS Nano* **2015**, *9* (11), 10664–10672.

(39) Drelich, J.; Chibowski, E. Superhydrophilic and Superwetting Surfaces: Definition and Mechanisms of Control. *Langmuir* **2010**, *26* (24), 18621–18623.

(40) Su, B.; Tian, Y.; Jiang, L. Bioinspired Interfaces with Superwettability: From Materials to Chemistry. *J. Am. Chem. Soc.* **2016**, 138 (6), 1727–1748.

(41) Drelich, J.; Chibowski, E.; Meng, D. D.; Terpilowski, K. Hydrophilic and Superhydrophilic Surfaces and Materials. *Soft Matter* **2011**, *7* (21), 9804.

(42) Zhang, P.; Lin, L.; Zang, D.; Guo, X.; Liu, M. Designing Bioinspired Anti-Biofouling Surfaces Based on a Superwettability Strategy. *Small* **2016**, *13* (4), 1–9.

(43) Ucar, I. O.; Cansoy, C. E.; Erbil, H. Y.; Pettitt, M. E.; Callow, M. E.; Callow, J. A. Effect of Contact Angle Hysteresis on the Removal of the Sporelings of the Green Alga *Ulva* from the Fouling-Release Coatings Synthesized from Polyolefin Polymers. *Biointerphases* **2010**, *5* (3), 75–84.

(44) Alexander, M. R.; Williams, P. Water Contact Angle Is Not a Good Predictor of Biological Responses to Materials. *Biointerphases* **2017**, *12* (2), 02C201.

(45) Hanaor, D. A. H.; Sorrell, C. C. Review of the Anatase to Rutile Phase Transformation. *J. Mater. Sci.* **2011**, *46* (4), 855–874.

(46) Hurum, D. C.; Agrios, A. G.; Gray, K. A.; Rajh, T.; Thurnauer, M. C. Explaining the Enhanced Photocatalytic Activity of Degussa P25 Mixed-Phase TiO2 Using EPR. *J. Phys. Chem. B* **2003**, *107* (19), 4545–4549.

(47) Kim, B. J.; Meng, E. Micromachining of Parylene C for BioMEMS. *Polym. Adv. Technol.* **2016**, *27* (5), 564–576.

(48) Dobosz, K. M.; Kolewe, K. W.; Schiffman, J. D. Green Materials Science and Engineering Reduces Biofouling: Approaches for Medical and Membrane-Based Technologies. *Front. Microbiol.* **2015**, *6* (MAR), 1–8.

CHAPTER 4

NANOCERIA-BASED SHARK-SKIN PATTERNS WITH BIOSENSING AND ANTIFOULING ACTIVITIES

4.1 Introduction

Hydrogen peroxide (H_2O_2) is an essential analyte in medical diagnosis, in fact, many illnesses such as cancer or neurodegenerative diseases can be diagnosed at an early stage with an accurate H_2O_2 detection.[1] There is considerable interest in H_2O_2 biosensing not only as a disease biomarker but also as an intermediate analyte for many enzymatic reactions. Moreover, antifouling biosensors are in high demand not only in health-care but also in many industries such as in food processing and pharmaceuticals. However, the biggest challenge of the current sensors is stability in a biological environment. The sensitivity of the sensor decreases due to adhesion of proteins (e.g., albumin, fibrinogen, fibronectin, and collagen) and cells (red blood cells, macrophages, bacteria).[2] Within a few weeks, an avascular fibrous capsule is formed around the device and reduces the mass transfer of the analyte significantly.[3] Thus, there is a need for a long-term durable antifouling surface for any sensor to be able to obtain accurate and reliable results in biological media.

Cerium dioxide (CeO_2) is a biocompatible, low-cost material and has been widely applied in catalysis, in fuel cells, as a metal polishing agent, and in photochemistry.[4] CeO_2 has an ability to switch oxidation states between III and IV which makes CeO_2 a perfect catalyst to reduce H_2O_2 by mimicking the enzyme, superoxide dismutase (SOD).[5,6] CeO_2 nanoparticles (NPs) have been explored for non-enzymatic H_2O_2 sensors and showed great

catalytic responses with high selectivity.[7–9] However, the stability of the sensors in a biofouling environment continued to be a big issue that has not been well-addressed.[8,10]

Antifouling properties of a surface is influenced by many factors including the surface chemistry, topography, and mechanical characteristics.[11,12] Protein adsorption on CeO_2 NPs is highly favorable at neutral pH due to the high isoelectric point of CeO_2 NPs.[13] Charge interactions can be prevented with an antifouling hydrogel coating such as poly (ethylene glycol) (PEG) and poly (hydroxyethyl methacrylate) (PHEMA).[14–16] PEG and PHEMA show resistance to protein adsorption and cell adhesion due to low interfacial energy with water.[17,18] Moreover, hydrogels perform well as protective coatings that do not block the analyte transfer required for sensor performance. However, protein adsorption and subsequent cell accumulation on the smooth hydrogels nevertheless do occur after a sufficient amount of time due to defects or the complex biological environment. The commercially available, bioinspired, micropatterned surface, Sharklet AF™, has been shown to prevent adhesion of Ulva spores, bacteria, and platelet cells.[19–21] A conformal, pin-hole-free, uniform hydrogel coating can be deposited onto a shark-skin surface via initiated chemical vapor deposition (iCVD). Yague et al. demonstrated that a synthesized PHEMA hydrogel crosslinked with EGDA, p(HEMA-co-EGDA), via iCVD resulted in obtaining mechanically stable hydrogel films.[22] Hydrogel coatings including PHEMA have been demonstrated to be resistant to protein adsorption while allowing for the permeation of small analytes for sensing.[23] Thus, the combined characteristics of the antifouling hydrogel and shark-skin electrode on a single surface will prevent protein adsorption and cell adhesion for a long-term biosensor device.

In this study, we designed an antifouling H_2O_2 biosensor based on enzyme-mimetic CeO_2 NPs. CeO_2 NPs were dispersed in a solvent and CeO_2 shark-skin patterns were

imprinted using solvent-assisted soft nanoimprint lithography.[24,25] To decrease protein adsorption, a conformal coating of p(HEMA-co-EGDA) hydrogel was deposited onto the CeO_2 shark-skin electrodes via iCVD. Excellent H_2O_2 sensing, with high selectivity and sensitivity, was demonstrated. Non-enzymatic antifouling CeO_2 shark-skin electrodes offer long-term durable, low-cost devices for H_2O_2 detection for early diagnosis of many diseases. Antifouling shark-skin electrodes can be applied to other types of analytes by incorporating corresponding sensing materials and can also be scaled up for many other practical applications.

4.2 Experimental Section

4.2.1 Materials

All materials were used as received without further purification. Cerium dioxide (CeO_2) (20wt% in water) nanoparticles (NPs) (10-20 nm diameter) were purchased from Nyacol Nano Technologies, Inc (Ashland, MA). N-methyl-2-pyrrolidone (NMP, ReagentPlus 99%), M9 minimal salts (M9 media), potassium hexacyanoferrate (III), potassium hexacyanoferrate (II) trihydrate, and phosphate buffered saline (PBS, 10× sterile biograde were purchased from Sigma-Aldrich (St. Louis, MO). Methanol (MeOH) and poly(tetrafluoroethylene) (PTFE) filters (0.45 μm) were purchased from Fisher Scientific (Hampton, NH). Heptadecafluoro-1,1,2,2-tetrahydrodecyl)dimethylchlorosilane was acquired from Gelest (Morrisville, PA). Sylgard 184 silicone elastomer kit (polydimethylsiloxane (PDMS)) was purchased from Dow Corning (Midland, MI).

4.2.2 Methods

Solvent Exchange of CeO_2 Nanoparticle (NP) Dispersion

The details of solvent exchange can be found in previous publications from our group.[26] Briefly, CeO_2 (100 g of 20 wt%) aqueous dispersion was added into a 250 mL bottle. NMP (50 g) and MeOH (50 g) were added to the dispersion and mixed. The mixed solution was placed under air flow overnight until the majority of the solvent was removed. The mass of the solvent and solids were calculated and subsequently, NMP and MeOH were added to the mixture in a 1:0.5 weight ratio to obtain an approximately 25 wt% CeO_2 dispersion. The dispersion was sonicated (30 min) until a stable CeO_2 NP dispersion was obtained. The final CeO_2 concentration was calculated as 25.2 wt% and remained stable for over a year.

Fabrication of PDMS mold and CeO_2 Shark Skin Microstructures

To prepare PDMS molds, Sylgard 184 was mixed in a 1:10 ratio of curing agent to base, then poured onto a Sharklet AF^{TM} nickel (height: 3 μm, width: 2 μm, pitch: 4 μm) master mold (provided by Sharklet Technologies), and then placed into an oven to be crosslinked at 70°C for 3 h. The CeO_2 NP dispersion was spin-coated onto a gold-sputtered silicon wafer. The spin coating conditions were optimized to achieve a 700 nm dry film. The inverse Sharklet PDMS mold was placed onto the still-wet, spin-coated film. As the remaining solvent evaporates through the mold, the rigid shark skin structures were formed. The stamp/substrate assembly was placed on a hot plate (50°C) for 5-10 min. The PDMS mold was peeled off and CeO_2 shark-skin-patterned surfaces were obtained. After the imprinting step, CeO_2 shark-skin-patterned surfaces were sintered at 500 °C for 1 h and then used for further experiments.

P(HEMA-co-EGDA) Hydrogel Coating via iCVD

Thin films were deposited by using a commercial iCVD facility (GVD Corp.). The CeO_2 shark-skin-patterned and smooth films were placed on a heat controlling stage, with constant temperature at 26℃. A mixed vapor flow containing the vaporized tert-butyl peroxide (TBPO) initiator, HEMA and EGDA were transferred into the vacuum chamber (base pressure 30 mTorr) by mild heating. TBPO, HEMA and EGDA were heated at 30℃, 35℃ and 55℃ respectively. The total pressure in the chamber during the deposition was controlled to be 60 mTorr and the flow rates were 0.5 sccm, 1.5 sccm and 0.5 sccm for TBPO, HEMA and EGDA, respectively. The temperature of the heating filament array was approximately 187.8℃, confirmed by an attached thermocouple. The target deposition thickness was 40-60 nm, as monitored by in-situ interferometry.

4.2.3 Characterization

Material Characterization

The 25.2 wt% CeO_2 NP dispersion was diluted with NMP and drop casted on carbon coated copper grids for transmission electron microscopy (TEM) imaging. TEM was performed in bright field imaging mode using a JEOL 2000 FX. TEM was operated at an accelerating voltage of 200 kV. Scanning electron microscopy (SEM) was performed on a field emission scanning electron microscope (Magellan 400). 3D optical profilometry (Zygo, Nexview) was used to measure feature dimensions. Thermogravimetric analysis (TGA, TA Instruments Q50) of CeO_2 NPs was conducted using the following temperature program under air: heating from room temperature to 500°C, at a rate of 10 °C/min.

Electrochemical Tests

Electrochemical measurements (cyclic voltammetry (CV) and chronoamperometry (CA)) were performed using a CHI 660E electrochemical workstation with a three-electrode system: a working electrode, a Pt wire counter electrode and an Ag/AgCl reference electrode. CV was performed in 40 mL PBS (pH 7.4) with a potential range of 0.8 V to −0.8 V at a scan rate of 50 mV/s. CA was conducted in 40 mL PBS (pH 7.4) at -0.4 V, based on the redox activity implicated in CV scans, and H_2O_2 was added at different concentrations to generate a calibration curve. The CA measurements were run with the addition of 1 mM H_2O_2 and interfering species (1 mM ascorbic acid (AA), and uric acid (UA)).

In-Situ Protein Adsorption Test

In-situ antifouling tests were performed using the CeO_2 shark-skin electrode and p(HEMA-co-EGDA) coated CEO_2 shark-skin electrode in 2.5 mg/ml bovine serum albumin (BSA) in the presence of 2.5 mM/2.5 mM $[Fe(CN)_6]^{4-}/[Fe(CN)_6]^{3-}$ redox probe and CV was recorded at every 15 min for 1 h.

Antifouling Performance

The fouling resistance of p(HEMA-co-EGDA) coated shark-skin-patterned surfaces, as well as smooth-surface control samples were evaluated with a bacterial attachment assay using the model bacteria, *Escherichia coli* K12 MG1655 (*E. coli*, expressing green fluorescent protein).[27] *E. coli* was cultured overnight in Luria-Bertani broth (Sigma-Aldrich) then washed and re-suspended in M9 media to a final concentration of 1×10^8 cells/mL. Samples and controls were placed at the base of separate wells in 6-

well polystyrene plates (Fisher Scientific) and inoculated with 5 mL of *E. coli* suspended in M9 media. Following a 24 h incubation period at 37ºC, the growth media was removed using a sterilized glass pipette and samples were rinsed repeatedly with PBS before analysis. Samples were analyzed using a Zeiss Microscope Axio Imager A2M (20× and 50× magnification, Thornwood, NY). The surface area coverage of attached bacteria was quantified by analyzing 10–15 randomly acquired images over at least three parallel replicates using *ImageJ* 1.45 software (National Institutes of Health, Bethesda, MD).

4.3 Results and Discussion

4.3.1 CeO_2 Shark-Skin and p(HEMA-co-EGDA) Coating

Ceria NPs were imprinted in shark-skin-patterned surfaces via solvent-assisted soft NIL.[25] After the successful imprinting and annealing of CeO_2 shark-skin-patterned surfaces, iCVD was conducted to obtain conformal p(HEMA-co-EGDA) hydrogel onto the shark-skin surfaces. The scheme of the imprinting process is shown in **Figure 1**. Direct imprinting of NPs requires several criteria to obtain complete, uniform, and reproducible replication. First, the NP-based dispersion needs to be stable in low and high volatility solvents with low surface tensions. Second, the dispersion must have a relatively high concentration, depending on the NP size, (~10-25 wt%) to be able to imprint micron-thickness features. Here, the solvent exchange of the CeO_2 NPs was conducted from an aqueous dispersion to NMP/MeOH solvent mixture, and a ~25 wt% stable dispersion was obtained. Imprinting conditions were discussed in detail in our previous publications.[24,25,28,29] Dynamic light scattering (DLS) shows that the particle size distribution in NMP/MeOH is between 5-30 nm, which indicates that the CeO_2 NPs stay in small clusters in the NMP/MeOH solvent mixture (**Figure 2a**).

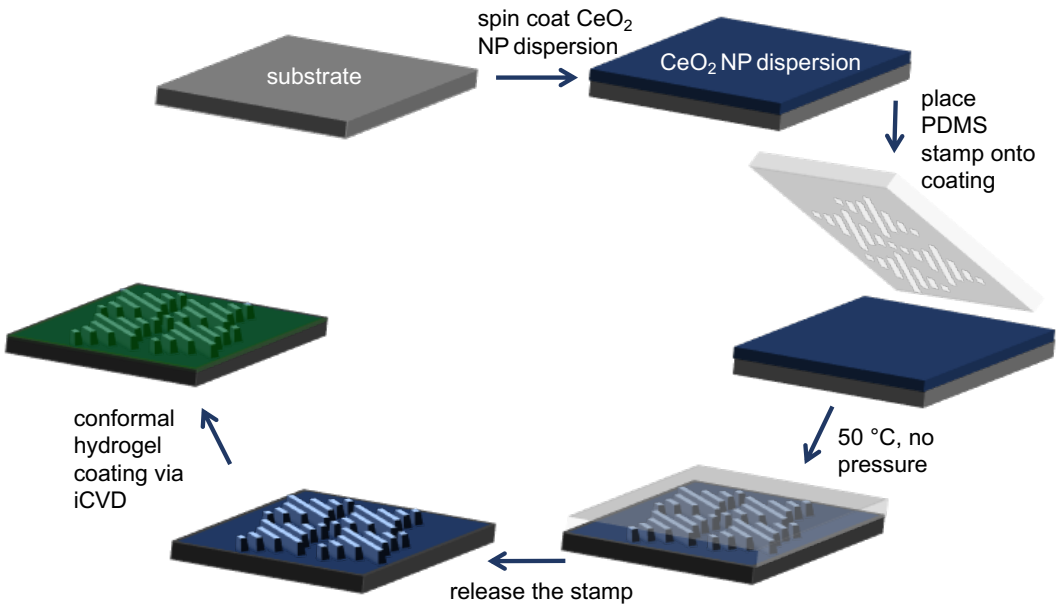

Figure 4.1. Schematic representation of the fabrication process of shark skin patterns using a PDMS soft stamp on gold coated Si wafers.

SEM micrographs of CeO_2 shark-skin patterned surfaces and p(HEMA-co-EGDA) coated CeO_2 shark-skin patterned surfaces are shown in **Figure 2**. The shark-skin patterns were successfully replicated uniformly in size and shape. The dimensions of the shark skin imprints were determined through optical profilometry and SEM imaging. The height, width, and spacing of the riblets were ~2 µm, ~1 µm and ~3 µm, respectively. Conformal, uniform, and pinhole-free p(HEMA-co-EGDA) coverage was observed on the patterned surfaces . The thickness of the coating was determined to be ~50 nm via cross-sectional SEM imaging (**Figure 2d**).

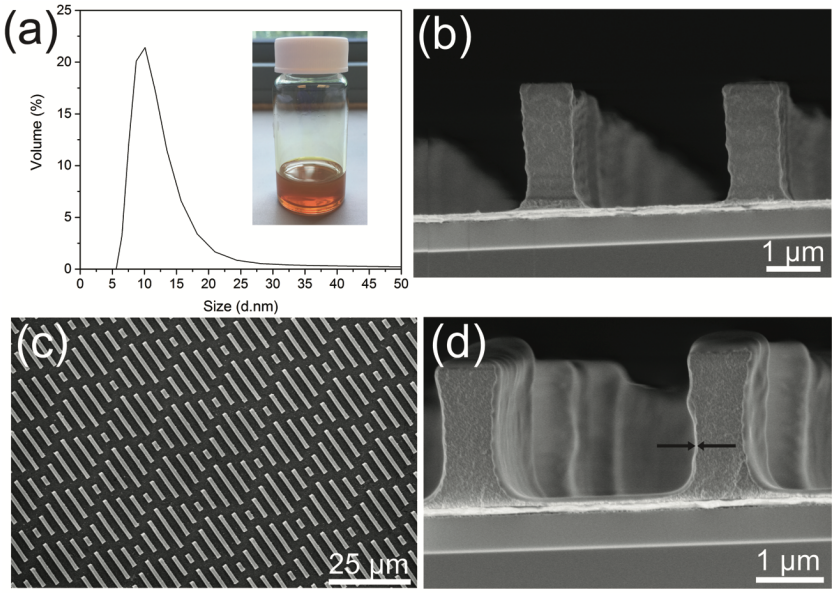

Figure 4.2. (a) DLS measurement of CeO_2 NP size distribution, digital image of the CeO_2 ink. SEM micrographs of (b) cross-section of CeO_2 shark-skin-patterned surface, (c) p(HEMA-co-EGDA) coated CeO_2 shark-skin-patterned surface, (d) cross-section of 50 nm p(HEMA-co-EGDA) coating on CeO_2 shark-skin-patterned surface.

In order to obtain a stable hydrogel film in the buffer solution, the composition of EGDA crosslinker in P(HEMA-co-EGDA) was adjusted to be approximately 10% and confirmed in the FTIR calculating the intensity ratio of hydroxyl peaks and carbonyl peaks.[22] Yague et al. reported that mesh size of P(HEMA-co-EGDA) hydrogel was between 0.5 nm and 2 nm depending on crosslinking amount.[22] Low amount of EGDA enables crosslinking of HEMA without decreasing mesh size of hydrogel significantly for sensing of the analytes. Therefore, we obtained a stable hydrogel film in the buffer solutions.

4.3.2 Electrochemical Activities

P(HEMA-co-EGDA)-coated CeO_2 shark-skin electrodes were tested to detect H_2O_2. CV curves are shown before and after the addition of 1 mM H_2O_2 (**Figure 3a**), in

which the current clearly increases with the addition of H_2O_2 as a result of the catalytic reduction of H_2O_2. **Figure 3b** shows the CA plots of the P(HEMA-co-EGDA)-coated CeO_2 shark-skin electrodes upon successive additions of 1 mM H_2O_2 in a PBS solution (pH=7.4) at -0.4 V. A working voltage of -0.4 V was selected to obtain a significant current response and to avoid interference species.[9] A sufficiently good response time, between 1-2 s, was observed as a result of having thin hydrogel coating of approximately 50 nm. Montero et al. analyzed two different thicknesses of pHEMA hydrogel coatings, 100 and 200 nm, and showed that the sensing performance of 100 nm hydrogel was significantly better than 200 nm thickness due to faster diffusion and hydration process.[30]

A calibration curve was obtained with the addition of 0.125 mM-1.0 mM concentrations of H_2O_2 solution. The calibration curve was linear in the range of 0.1-1.0 mM H_2O_2 with a correlation coefficient of 0.999 and a sensitivity of 44.1 $\mu A.cm^{-2}.mM^{-1}$ (**Figure 3c**). The sensitivity obtained in this study was higher than many reported CeO_2-based non-enzymatic H_2O_2 sensors.[8,9] The detection limit was estimated to be 6 μM at a signal-to-noise ratio of 3. Finally, the selectivity of the sensor was tested with the addition of 1 mM ascorbic acid (AA) and uric acid (UA), which are common interference species. There was no significant current change as shown in **Figure 3d**. Thus, non-enzymatic CeO_2-based shark-skin sensors showed excellent selectivity and sensitivity. The stability of the electrodes was investigated in protein and cell-based buffer solutions.

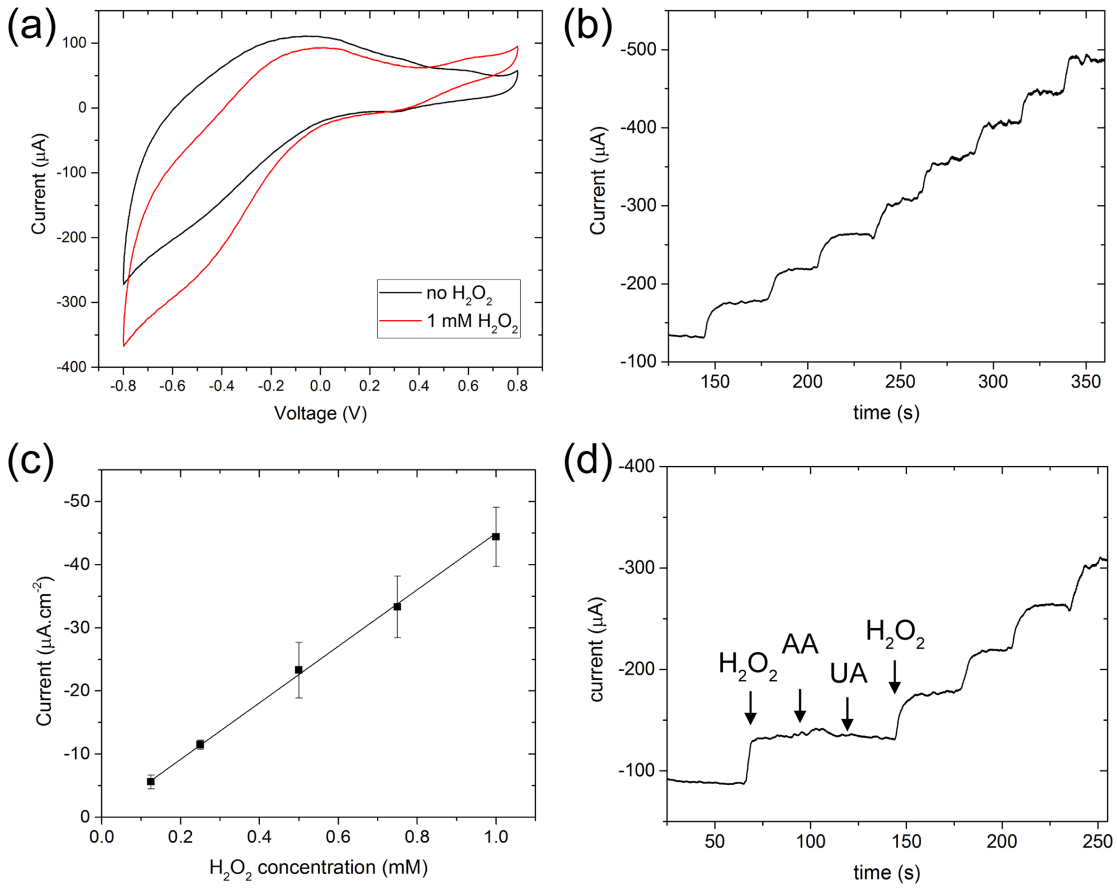

Figure 4.3. (a) CV of CeO_2 shark-skin biosensor before and after addition of 1mM H_2O_2 in PBS (pH:7.4). (b) chronoamperometric response of continuous addition of 1mM H_2O_2 in PBS (pH:7.4) at -0.4V. (c) amperometric response as a function of H_2O_2 concentration. (d) with addition of interfering species (ascorbic acid (AA) and uric acid (UA)) and H_2O_2.

4.3.3 Antifouling Activities

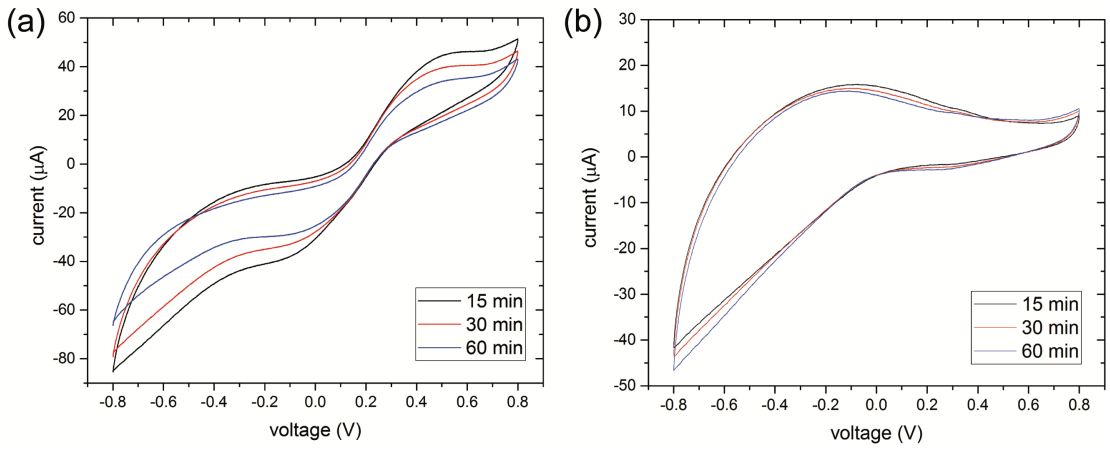

Figure 4.4. In-situ antifouling test for 1 h. CV of (a) CeO_2 shark-skin electrode, (b) P(HEMA-co-EGDA) coated CeO_2 shark-skin electrode in 2.5 mg/ml BSA in $Fe(CN_6)^{4-/3-}$.

To evaluate the protein adsorption resistance of the p(HEMA-co-EGDA), we ran in-situ antifouling tests in a protein medium. CV measurements of the CeO_2 shark-skin and p(HEMA-co-EGDA) coated CeO_2 shark-skin electrodes were taken in a 2.5 mg/ml BSA solution at every 15 min for 1 h. The current decreased significantly due to the fouling of BSA on the CeO_2 shark-skin electrode (**Figure 4a**). This result is due to the favorable charge interaction between BSA and CeO_2. CeO_2 has a high isoelectric point (IEP) of 9.5, which is positively charged at pH 7.4. The IEP of BSA is 4.7 and negatively charged at pH 7.4. Thus, immobilization of proteins on a CeO_2 surface is favored due to strong electrostatic interaction. In highly concentrated protein mediums, excessive fouling occurs which causes a decrease in sensitivity and leaching of the CeO_2. However, our p(HEMA-co-EGDA)-coated CeO_2 shark-skin electrode did not show any significant current decrease in the 2.5 mg/ml BSA solution (**Figure 4b**). Thus, the BSA adsorption on the electrodes was decreased using p(HEMA-co-EGDA) hydrogel; however, it is well-known that despite

having a great protein resistance, after a sufficient amount of time, the cells (e.g., bacteria and platelet) can still accumulate on the electrode surface in the absence of a secondary mechanism to prevent cell attachment.

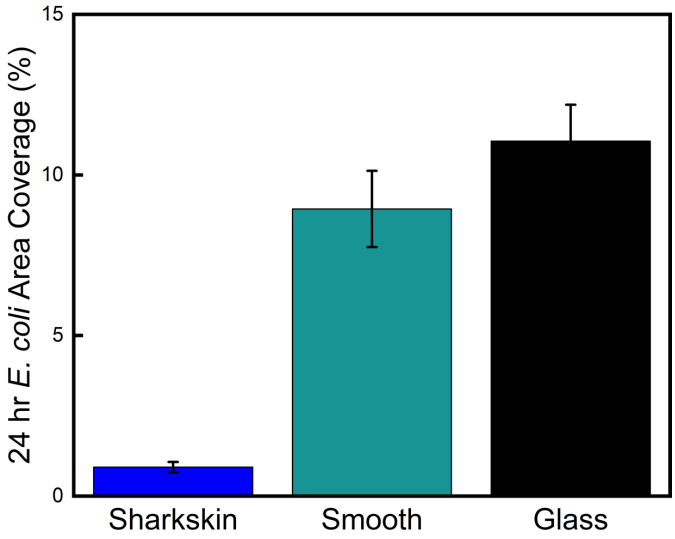

Figure 4.5. The 24 h area coverage of surface-adhered E. coli on p(HEMA-co-EGDA) coated CeO2 smooth films versus shark-skin-patterned surfaces. An asterisk (*) denotes 95% significance between smooth and patterned samples. Error bars denote standard error.

To demonstrate the effectiveness of microtopography against cell adhesion, we performed an antifouling test using a model bacteria cell, *Escherichia coli (E. coli)* for 24 h (**Figure 5**). Our results indicate/show that P(HEMA-co-EGDA)-coated CeO_2 shark-skin electrodes significantly decreased the *E. coli* attachment by up to 90% compared to smooth, p(HEMA-co-EGDA)-coated CeO_2 electrodes. In the previous chapters (**Chapter 2** and **Chapter 3**), we discussed the antifouling behavior of shark-skin-patterned surfaces in more detail. Briefly, the antifouling characteristics of shark-skin-patterned surfaces are dominated by the relationship between bacterial cell and pattern feature sizes, rather than surface chemistry and wettability. Topography and surface chemistry have been studied for antifouling performance, however, there are not many reports on combined biosensing and antifouling activities. Herein, we have shown that the combination of an antifouling

hydrogel coating with a non-enzymatic shark-skin topography offers excellent protein- and cell-resistant surfaces, which are ideal for biosensing applications.

4.4 Conclusions

We have presented a simple strategy to fabricate multifunctional shark skin surfaces with both biosensing and antifouling activities. To the best of our knowledge, this work represents the first reported antifouling shark skin patterns that also exhibit biosensing activity. Non-enzymatic CeO_2 shark-skin-electrodes were fabricated via a straight-forward, solvent-assisted imprinting method. Excellent H_2O_2 sensing by the shark-skin electrodes, with strong selectivity towards AA and UA, was demonstrated, and BSA adsorption on CeO_2 shark-skin surfaces was decreased by depositing a conformal p(HEMA-co-EGDA) hydrogel coating. Moreover, p(HEMA-co-EGDA) coated shark-skin-patterned surfaces reduced the attachment of *E. coli* by 90% after a 24 h incubation. Protein- and cell-resistant shark-skin electrodes offer long-term, stable biosensors for many practical applications.

4.5 References

(1) Sena, L. A.; Chandel, N. S. Physiological Roles of Mitochondrial Reactive Oxygen Species. *Mol. Cell* **2012**, *48* (2), 158–166.

(2) Gorbet, M. B.; Sefton, M. V. Biomaterial-Associated Thrombosis: Roles of Coagulation Factors, Complement, Platelets and Leukocytes. *Biomater. Silver Jubil. Compend.* **2006**, *25*, 219–241.

(3) Wisniewski, N.; Reichert, M. Methods for Reducing Biosensor Membrane Biofouling. *Colloids Surfaces B Biointerfaces* **2000**, *18* (3–4), 197–219.

(4) Reed, K.; Cormack, A.; Kulkarni, A.; Mayton, M.; Sayle, D.; Klaessig, F.; Stadler, B. Exploring the Properties and Applications of Nanoceria: Is There Still Plenty of Room at the Bottom? *Environ. Sci. Nano* **2014**, *1* (5), 390–405.

(5) Karakoti, A. S.; Kuchibhatla, S. V. N. T.; Babu, K. S.; Seal, S. Direct Synthesis of

Nanoceria in Aqueous Polyhydroxyl Solutions. *J. Phys. Chem. C* **2007**, *111* (46), 17232–17240.

(6) Korsvik, C.; Patil, S.; Seal, S.; Self, W. T. Superoxide Dismutase Mimetic Properties Exhibited by Vacancy Engineered Ceria Nanoparticles. *Chem. Commun.* **2007**, No. 10, 1056–1058.

(7) Mehta, A.; Patil, S.; Bang, H.; Cho, H. J.; Seal, S. A Novel Multivalent Nanomaterial Based Hydrogen Peroxide Sensor. *Sensors Actuators, A Phys.* **2007**, *134* (1), 146–151.

(8) Neal, C. J.; Gupta, A.; Barkam, S.; Saraf, S.; Das, S.; Hyoung, J. Picomolar Detection of Hydrogen Peroxide Using Enzyme-Free Inorganic Nanoparticle-Based Sensor. *Sci. Rep.* **2017**, No. October 2016, 1–10.

(9) Ujjain, S. K.; Das, A.; Srivastava, G.; Ahuja, P.; Roy, M.; Arya, A.; Bhargava, K.; Sethy, N.; Singh, S. K.; Sharma, R. K.; Das, M. Nanoceria Based Electrochemical Sensor for Hydrogen Peroxide Detection. *Biointerphases* **2014**, *9* (3), 031011.

(10) Jiao, X.; Song, H.; Zhao, H.; Bai, W.; Zhang, L.; Lv, Y. Well-Redispersed Ceria Nanoparticles: Promising Peroxidase Mimetics for H 2O 2 and Glucose Detection. *Anal. Methods* **2012**, *4* (10), 3261–3267.

(11) Anselme, K.; Davidson, P.; Popa, A. M.; Giazzon, M.; Liley, M.; Ploux, L. The Interaction of Cells and Bacteria with Surfaces Structured at the Nanometre Scale. *Acta Biomater.* **2010**, *6* (10), 3824–3846.

(12) Song, F.; Koo, H.; Ren, D. Effects of Material Properties on Bacterial Adhesion and Biofilm Formation. *J Dent Res* **2015**, *94* (8), 1027–1034.

(13) Patil, S.; Sandberg, A.; Heckert, E.; Self, W.; Seal, S. Protein Adsorption and Cellular Uptake of Cerium Oxide Nanoparticles as a Function of Zeta Potential. *Biomaterials* **2007**, *28* (31), 4600–4607.

(14) Banerjee, I.; Pangule, R. C.; Kane, R. S. Antifouling Coatings: Recent Developments in the Design of Surfaces That Prevent Fouling by Proteins, Bacteria, and Marine Organisms. *Adv. Mater.* **2011**, *23* (6), 690–718.

(15) Desai, N. P.; Hubbell, J. A. Solution Technique to Incorporate Polyethylene Oxide and Other Water-Soluble Polymers into Surfaces of Polymeric Biomaterials. *Biomaterials* **1991**, *12* (2), 144–153.

(16) Tanaka, M.; Mochizuki, A.; Ishii, N.; Motomura, T.; Hatakeyama, T. Study of Blood Compatibility with Poly(2-Methoxyethyl Acrylate). Relationship between Water Structure and Platelet Compatibility in Poly(2-Methoxyethylacrylate-Co-2-Hydroxyethylmethacrylate). *Biomacromolecules* **2002**, *3* (1), 36–41.

(17) Ostuni, E.; Chapman, R. G.; Liang, M. N.; Meluleni, G.; Pier, G.; Ingber, D. E.; Whitesides, G. M. Self-Assembled Monolayers That Resist the Adsorption of

Proteins and the Adhesion of Bacterial and Mammalian Cells. *Langmuir* **2001**, *17* (20), 6336–6343.

(18) Krishnan, S.; Wang, N.; Ober, C. K.; Finlay, J. A.; Callow, M. E.; Callow, J. A.; Hexemer, A.; Sohn, K. E.; Kramer, E. J.; Fischer, D. A. Comparison of the Fouling Release Properties of Hydrophobic Fluorinated and Hydrophilic PEGylated Block Copolymer Surfaces: Attachment Strength of the Diatom Navicula and the Green Alga Ulva. *Biomacromolecules* **2006**, *7* (5), 1449–1462.

(19) Schumacher, J. F.; Carman, M. L.; Estes, T. G.; Feinberg, A. W.; Wilson, L. H.; Callow, M. E.; Callow, J. a; Finlay, J. a; Brennan, A. B. Engineered Antifouling Microtopographies - Effect of Feature Size, Geometry, and Roughness on Settlement of Zoospores of the Green Alga Ulva. *Biofouling* **2007**, *23* (1–2), 55–62.

(20) Chung, K. K.; Schumacher, J. F.; Sampson, E. M.; Burne, R. a; Antonelli, P. J.; Brennan, A. B. Impact of Engineered Surface Microtopography on Biofilm Formation of Staphylococcus Aureus. *Biointerphases* **2007**, *2* (2), 89–94.

(21) May, R. M.; Magin, C. M.; Mann, E. E.; Drinker, M. C.; Fraser, J. C.; Siedlecki, C. A.; Brennan, A. B.; Reddy, S. T. An Engineered Micropattern to Reduce Bacterial Colonization, Platelet Adhesion and Fibrin Sheath Formation for Improved Biocompatibility of Central Venous Catheters. *Clin. Transl. Med.* **2015**, *4* (1), 9.

(22) Yag??e, J. L.; Gleason, K. K. Systematic Control of Mesh Size in Hydrogels by Initiated Chemical Vapor Deposition. *Soft Matter* **2012**, *8* (10), 2890–2894.

(23) Baxamusa, S. H.; Montero, L.; Dubach, J. M.; Clark, H. A.; Borros, S.; Gleason, K. K. Protection of Sensors for Biological Applications by Photoinitiated Chemical Vapor Deposition of Hydrogel Thin Films. *Biomacromolecules* **2008**, *9* (10), 2857–2862.

(24) Kothari, R.; Beaulieu, M. R.; Hendricks, N. R.; Li, S.; Watkins, J. J. Direct Patterning of Robust 1-D, 2-D and 3-D Crystalline Metal Oxide Nanostructures Using Imprint Lithography and Nanoparticle Dispersion Inks. *Chem. Mater.* **2017**, *29*, 3908−3918.

(25) Arisoy, F. D.; Kolewe, K. W.; Homyak, B.; Kurtz, I. S.; Schiffman, J. D.; Watkins, J. J. Bioinspired Photocatalytic Shark-Skin Surfaces with Antibacterial and Antifouling Activity via Nanoimprint Lithography. *ACS Appl. Mater. Interfaces* **2018**, 10 (23), 20055–20063.

(26) Beaulieu, M.; Hendricks, N.; Watkins, J. Large Area Printing of Optical Gratings and 3-D Photonic Crystals Using Solution Processable Nanoparticle/Polymer Composites. *ACS Photonics* **2014**, *1* (9), 799–805.

(27) Kolewe, K. W.; Peyton, S. R.; Schiffman, J. D. Fewer Bacteria Adhere to Softer Hydrogels. *ACS Appl. Mater. Interfaces* **2015**, *7* (35), 19562–19569.

(28) Li, S.; Kazemi-moridani, A.; Zhou, Y.; Howell, I. R.; Kothari, R.; Lee, J.; Watkins,

J. J. Wavelength-Selective Three-Dimensional Thermal Emitters via Imprint Lithography and Conformal Metallization. *ACS Appl. Mater. Interfaces,* **2018**, 10 (9), 8173–8179.

(29) Li, W.; Zhou, Y.; Howell, I. R.; Gai, Y.; Naik, A. R.; Li, S.; Carter, K. R.; Watkins, J. J. Direct Imprinting of Scalable , High-Performance Woodpile Electrodes for Three-Dimensional Lithium-Ion Nanobatteries. *ACS Appl. Mater. Interfaces* **2018**, *10* (6), 5447–5454.

(30) Montero, L.; Gabriel, G.; Guimerà, A.; Villa, R.; Gleason, K. K.; Borrós, S. Increasing Biosensor Response through Hydrogel Thin Film Deposition: Influence of Hydrogel Thickness. *Vacuum* **2012**, *86* (12), 2102–2104.

CHAPTER 5

LOW-COST, DURABLE MASTER MOLDS FOR THERMAL-NIL, UV-NIL, AND INJECTION MOLDING

5.1 Introduction

Micro- or nanopatterned surfaces have a wide range of applications in optical devices, biosensors, structural colors, microfluidics, and self-cleaning.[1–4] Various nanopatterning techniques, lithographic methods, inkjet printing, and direct writing have been explored; however, large area production of patterned surfaces at low cost remains a challenge.[5,6] Nanoimprint lithography (NIL)[7,8] and micro/nano injection molding[9,10] have been the most promising of these replication techniques due to scalability speed, and high-resolution capabilities. However, master mold life-time is too short to fabricate millions of replicas within a short cycle time. For both NIL and micro/nano injection molding, the mold requires frequent replacement because of a lack of mold strength, which limits the commercial production of large-area, patterned surfaces.[11,12]

Silicon, quartz, and nickel are the most common hard molds in NIL. Hard molds are preferred over soft or hybrid molds due to high strength and durability. However, silicon-based molds are brittle and often have limited durability. Above the glass transition temperature (Tg) of thermoplastic polymers, polymers soften and can be molded with a hard stamp via thermal-NIL in several minutes. Moreover, UV-NIL is a more precise replication technique in which monomers are crosslinked after filling the cavities in a UV-transparent mold, resulting in rigid, patterned polymer replicas. Both thermal-NIL and UV-NIL suffer from limited mold lifetime due to stress accumulation from the repetitive direct patterning process.[13]

Injection molding is desired over NIL because it possesses the capability of producing millions of parts in a short time.[14] Steel master mold inserts have been used for pattern transfer in injection molding processes; however, fabrication of the steel molds with micro- or nanopatterns over large areas is challenging and requires multiple steps and long processing times.[15] On the other hand, electroformed nickel molds have been used as an alternative to the steel molds. Although the nickel molds can be fabricated at the lower cost compared to the steel molds, the nickel molds easily wear after 10,000 replication cycles.[16] Additional protective coatings, titanium nitrate (TiN), has been applied on the Nickel molds in CD/DVD industry, but unfortunately the coating was durable only up to 15,000-20,000 cycles.[17] the Bulk metallic glass molds (BMG)[16,18] and hydrogen silsesquioxane (HSQ) on steel[19] have also been demonstrated as alternative hard molds for injection molding. BMG molds were durable only up to 20,000 mold cycles with the cycle time less than 10 s.[20] Not only are these mold limited in durability, but also require the use of a sacrificial silicon-based master mold to fabricate BMG molds, limiting low-cost nanopattern production over a large area. Hydrogen silsesquioxane (HSQ) is an organosilicon imprint resist that has been used for e-beam etching processing and in optical applications.[21] Hobaek et al. showed that HSQ could be coated on steel surfaces and patterned using nanoimprint lithography.[19] Sol-gel imprinted inorganic materials often suffer because of high shrinkage which causes cracking.[22,23] Although nano/micro-patterned surfaces can be imprinted with high resolution and low roughness using HSQ resist, the lower modulus value of HSQ (27.9 GPa) compared to BMG and Nickel (~180-200 GPa) results in reduced mechanical durability and fewer cycles in the injection molding.[19,24] Thus, the current molds (steel and nickel) and alternative molds (BMG and HSQ) had either scalability or durability problems. Consequently, there is scientific and

commercial interest in developing novel process routes for durable and low-cost molds for mass production of micro- or nanopatterned surfaces.

We fabricated a UV-transparent, nano/micropatterned zirconium dioxide (ZrO_2) hard mold via solvent-assisted patterning technique and demonstrated successful pattern replication in polymer replicas using thermal-, UV-assisted NIL, and injection molding. ZrO_2 has outstanding thermal, chemical, and wear-resistant characteristics, which makes the ZrO_2 an excellent mold material for pattern transfer applications.[25] Recently, we developed a method of direct imprinting of metal oxide nanoparticles and used the patterned surfaces for antibacterial applications[26], batteries[27,28], and in optics[29,30]. In this study, the hardness and modulus of ZrO_2 films were determined as a function of annealing temperature. A variety of nano and micro features were imprinted in ZrO_2 on a variety of surfaces including flat and curve, and subsequently, the ZrO_2 molds were used for the next imprints. Moreover, a ZrO_2 nanopatterned mold was used for 115,000 injection molding cycles without any deformation. This low-cost, durable, and large area patterned ZrO_2 mold enables replication of a variety of nano/micro features for commercial and scientific applications.

5.2 Experimental Section

5.2.1 Materials

All materials were used as received without further purification. Zirconium dioxide (ZrO_2 50 wt% in ethanol (EtOH)) nanoparticles (NPs) (5 nm in diameter) were purchased from Pixelligent (Baltimore, MD). Poly(tetrafluoroethylene) (PTFE) filters (0.45 μm) and EtOH were purchased from Fisher Scientific (Hampton, NH). 1*H*,1*H*,2*H*,2*H*-Perfluorodecyltriethoxysilane (FDTS) was acquired from Gelest (Morrisville, PA).

Sylgard 184 silicone elastomer kit (polydimethylsiloxane (PDMS)) was purchased from Dow Corning (Midland, MI). 1,2 propanediol, Propylene glycol monomethyl ether acetate (PGMEA), and Poly(methyl methacrylate) (PMMA) (molecular weight 199,000 g/mol) were purchased from Sigma-Aldrich (St. Louis, MO). Norland Optical Adhesive 60 (NOA) was purchased from Norland Products, Inc. (Cranbury, NJ). Poly(ethylene terephthalate) (PET) film (ST 505, 125 μm thick films), Dupont, was purchased from Tekra Corporation (New Berlin, WI). Kapton (polyimide) film was purchased from American Durafilm (Holliston, MA). Stainless steel substrates (304 and 316L) were purchased from Stainlesssupply (Monroe, NC). Stainless steel wafers (316, diameter: 85 mm), steel inserts (2 cm x 2 cm, cube) and Si master molds were obtained/purchased from NIL Technologies (Kongens Lyngby, Denmark).

5.2.2 Methods

5.2.2.1 ZrO_2 Ink Formulation and ZrO_2 Master Mold Fabrication

To prepare PDMS molds, Sylgard 184 was mixed in a 1:10 ratio of curing agent to base, then poured onto various Silicon/Nickel master molds and placed into an oven to be crosslinked at 70^{o}C for 3 h. The 50 wt% ZrO_2 dispersion was diluted with ethanol and 1,2 propanediol down to between 25 to 10 wt%. The mixture was sonicated for 15 min, and a stable dispersion was obtained. Substrates were cleaned with hexane, acetone, and isopropanol, respectively, followed by 5-10 min of O_2 plasma. The ZrO_2 dispersion was spin coated onto the substrate, and then PDMS mold was placed onto the top of the coating. The stamp/coating assembly was placed on a hot plate (50 $^{\circ}$C) for a few minutes to get rid of all residual solvent. Then the PDMS mold was peeled off, and a patterned structure was obtained on the substrate. The patterned surfaces were annealed at 300^{o}C - 1000 ^{o}C for 2

h. Afterwards, the annealed patterned surface was fluorinated in order to create an anti-stick surface for the next imprints. The same procedure was conducted on the various type of substrates such as steel, glass, ceramics, and Kapton. The annealing temperature was limited based on the properties of the substrate material.

5.2.2.2 Solution Deposition Planarization of Rough Surfaces

A ZrO_2 nanoparticle solution (10-20 wt%) was spin coated onto the rough steel substrate as a thin layer (~400-500 nm in thickness), and after complete solvent removal, it was sintered at 350-500^oC for 15 min. The same procedure was repeated on the same steel via layer by layer coating until the roughness was sufficiently reduced.

5.2.2.3 Pattern Transfer Using ZrO_2 Master Mold

Thermal-NIL: Poly(methyl methacrylate) (PMMA, 199,000 g/mol) was dispersed in anisole at 30 wt% and spin coated onto the PET substrate to obtain a PMMA film. Thermal-NIL of the PMMA film was performed using Nanonex imprinting tool (NX-2000). The ZrO_2 mold was placed on the top of the PMMA film and thermal imprint was conducted under a pressure of 300 PSI at 140°C for 2 min. The ZrO_2 mold was peeled off easily and inverse patterned surfaces were obtained.

UV-NIL: UV-curable Norland Optical Adhesive (NOA60) was spin coated onto a PET substrate and the ZrO_2 mold was placed on the top of the coating. Then, UV-NIL was performed at RT under 365 nm UV light for 5-10 min using the Nanonex tool. The ZrO_2 mold was peeled off and inverse replicas were obtained.

Injection molding: Before polymer injection molding, the insert with nanopatterned ‘ZrO2' was coated with FDTS in order to reduce friction during demolding in the polymer

injection molding process. Acrylonitrile butadiene styrene (ABS) was dried for 2 h at 80°C before use. Parts were polymer injection molded in ABS (T_g = 105°C) with black dye in a 65 tons Battenfeld HM 65/350 machine using a constant temperature process. The mold temperature was set at 85°C and 70°C for the fixed and ejector side, respectively. A tool insert with nanopatterned 'ZrO2' was fitted on the fixed side. The melt temperature was 243°C. The injection time was 0.7 s at a 20 mm/s injection speed. Injection pressure reached 598 bar and holding pressure was 600 bar for 2 s. The mold was cooled for 10 s before the mold opened and the part was ejected. The cycle time was 15.2 s, and more than 114,000 parts were molded.

5.2.3 Characterization of ZrO_2 Dispersion, Mold and Polymer Replicas

A diluted ZrO_2 dispersion was drop casted on carbon-coated copper grids and transmission electron microscopy (TEM) imaging was performed in bright fi eld imaging mode using a JEOL 2000 FX. The ligand concentration of ZrO_2 NPs was confirmed by thermogravimetric analysis (TGA, TA Instruments Q50) using the following temperature program under air: heating from room temperature to 800 °C, with a rate of 10 °C/min. Mechanical properties of the ZrO_2 films were determined using a Hysitron TriboIndenter (TI 950) by averaging 30 indentations obtained under rate control (10 μN/s) using a Berkovich tip (100 nm) for each film. Imprinted patterned surfaces were characterized by scanning electron microscopy (SEM) using an FEI Magellan 400 FESEM. 3D optical profilometry (Zygo, Nexview), cross-sectional SEM, and atomic force microscopy (AFM) were used to measure feature dimensions.

5.3 Results and Discussion

5.3.1 Fabrication of the ZrO_2 Master Mold

A ZrO_2 mold was imprinted by solvent-assisted NIL[26,27,30] and polymer nano/micropatterns were replicated using the ZrO_2 mold as a working stamp via thermal-NIL, UV-NIL, and injection molding (**Figure 5.1**). To imprint the ZrO_2 mold, ZrO_2 NPs must be well-dispersed and stabilized in a mixture of high and low volatility solvents. The highly volatile solvent provides fast film formation and the low volatility solvent gives sufficient time for the imprinting.[26] A stable dispersion of ZrO_2 NPs was obtained after diluting the 50 wt% ZrO_2 dispersion with EtOH (high volatile solvent) and 1,2 PD (low volatile solvent). A TEM image of the NPs is shown in **Figure 5.2a and 5.2b**. The average diameter of the NPs was determined to be 5.2 ± 0.3 nm. Dynamic light scattering (DLS) shows that the particle size distribution in EtOH/1,2 PD is between 5-20 nm, which indicates that the ZrO_2 NPs forms tiny clusters in the solvent system (**Figure 5.2c).** The ligands on the ZrO_2 NPs enabled to have stable NPs up to 50 wt% solid concentration, which enabled to imprint variety of structures from nano to micron features. The weight percentage of the ligands was determined to be 16 % in total solid and confirmed by thermogravimetric analysis (TGA) (**Figure 5.2d**).

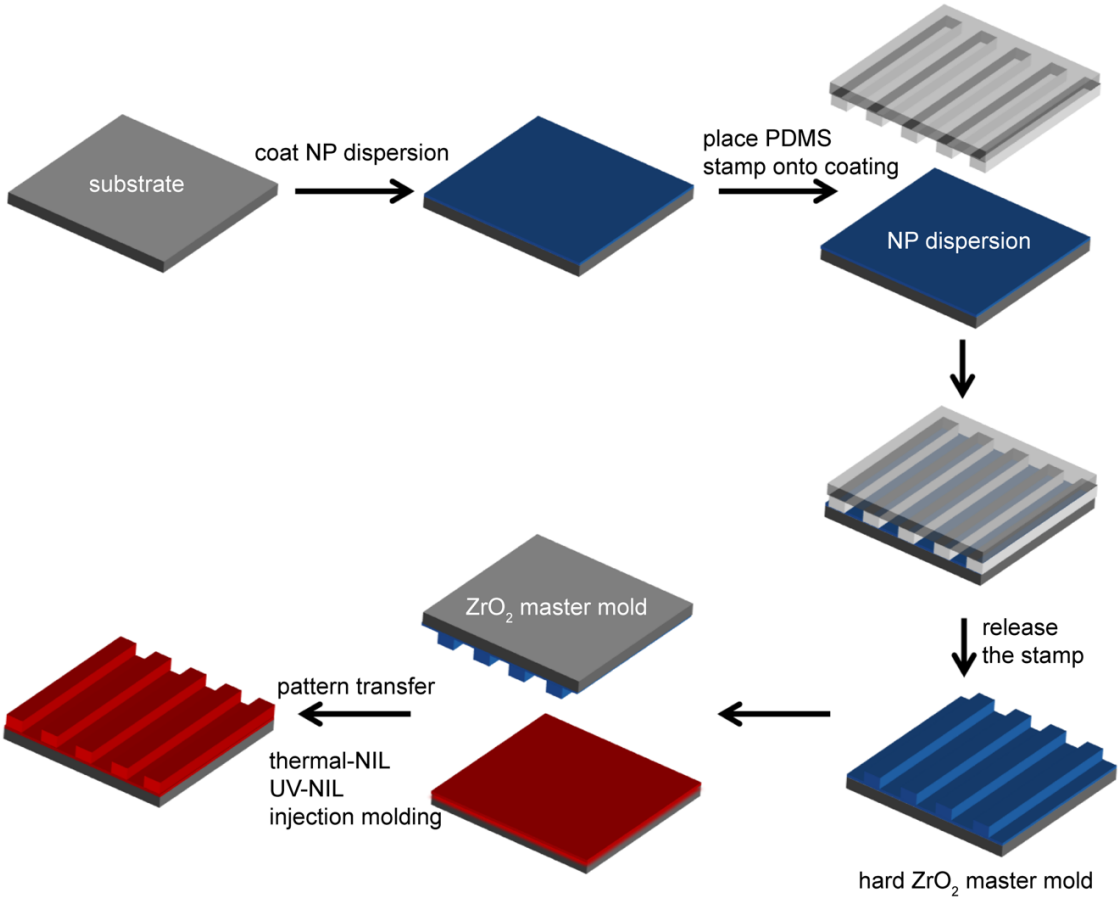

Figure 5.1. Schematic representation of patterning the hard ZrO_2 master mold and subsequent pattern transfer using the ZrO_2 mold.

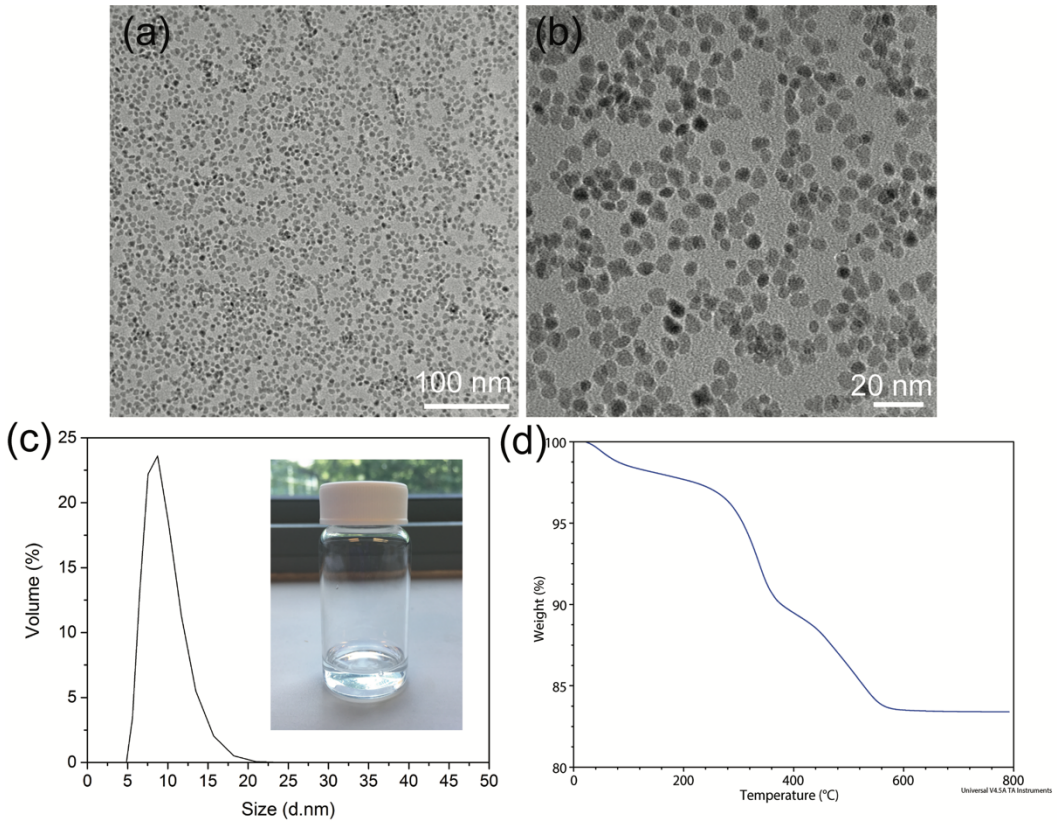

Figure 5.2. (a) TEM image of ZrO_2 NPs (drop casted from diluted ZrO_2 dispersion). (b) DLS measurement of ZrO_2 nanoparticles size distribution, digital image of the ZrO_2 ink. (c) TGA of ZrO_2 nanoparticles.

To increase the durability of the ZrO_2 mold, the ZrO_2 molds were annealed at various temperatures. As the annealing temperature increased from 300°C to 1000°C, hardness and reduced modulus values significantly increased (**Table 5.1**). Before annealing the ZrO_2 film, the hardness and modulus values were only 0.36 ± 0.02 GPa and 14 ± 2 GPa, respectively. After annealing the ZrO_2 film at 500°C, the hardness and modulus of the ZrO_2 coating significantly increased to 4.3 ± 0.6 GPa and 82 ± 6 GPa, respectively. Moreover, the hardness and modulus values increased significantly up to 11 ± 2 GPa and 120 ± 10 GPa, respectively, when sintered at 1000°C. The resulting high hardness and modulus values of the ZrO_2 mold suggest them to be durable and therefore suitable for high pressure

and rapid imprinting conditions. Denser films were obtained without any significant grain growth (**Figure 5.3**).

Table 5.1. Nanomechanical analysis of ZrO_2 as a function of annealed temperature. Standard deviation is displayed.

	As spun	300 °C	500 °C	750 °C	1000 °C
H (GPa)	0.36 ± 0.02	2.3 ± 0.2	4.3 ± 0.6	6.4 ± 0.7	11 ± 2
E_r (GPa)	14 ± 2	53 ± 8	82 ± 6	112 ± 6	120 ± 10

Direct NP patterning has several advantages compared to the imprinting of sol-gel precursors. Densification of sol-gel precursor causes a high amount of shrinkage (~60-80%), leading to cracks and defects upon calcination.[23,31] Previously, we demonstrated that direct imprinting of NPs demonstrated only 10-30% shrinkage, which enabled successful imprinting of a variety of geometries.[30] Another advantage of using ZrO_2 NPs as a mold is that the surface of the metal oxides can be easily modified with anti-sticking materials, unlike the steel and Nickel mold surfaces. The low surface energy of the fluorinated master molds prevents the adhesion of polymer materials on the mold surface. Moreover, the ZrO_2 mold can be used at high temperatures for embossing up to several thousand degrees.

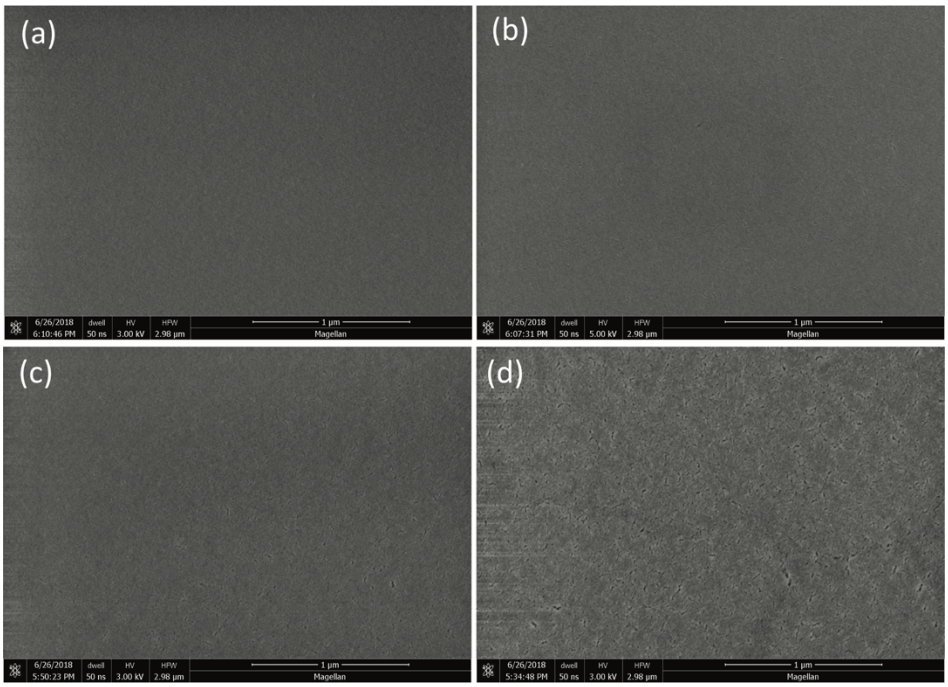

Figure 5.3. SEM micrographs of sintered ZrO_2 films at 300°C, 500°C, 750°C, and 1000°C for 2h under air.

5.3.2 Thermal Imprint using ZrO_2 Mold

A soft PDMS stamp was replicated from a structural-color patterned Si master mold (250 nm in height, **Figure 5.4a**) and a ZrO_2 mold (140 nm in height, **Figure 5.4b**) was imprinted using the PDMS mold on a Si wafer. After post-annealing of the ZrO_2 mold, thermal-NIL was conducted using the ZrO_2 mold and replicated structural colors in PMMA were obtained (**Figure 5.4c and Figure 5.5**). The beautiful colors are due to diffraction of light, which is well-known as structural colors that are inspired from nature (e.g., butterfly wings).[32] Thus, colorful surfaces and objects can be obtained without using any pigments or dye at low-cost. The same spot on the ZrO_2 mold was imaged in the SEM after imprinting ZrO_2 NPs, after 15 consecutive imprints, and after 30 consecutive imprints (**Figure 5.6**). There was no measurable difference in the quality of the obtained inverse nanostructure and also the ZrO_2 master mold after 30 consecutive imprints using the same ZrO_2 master mold.

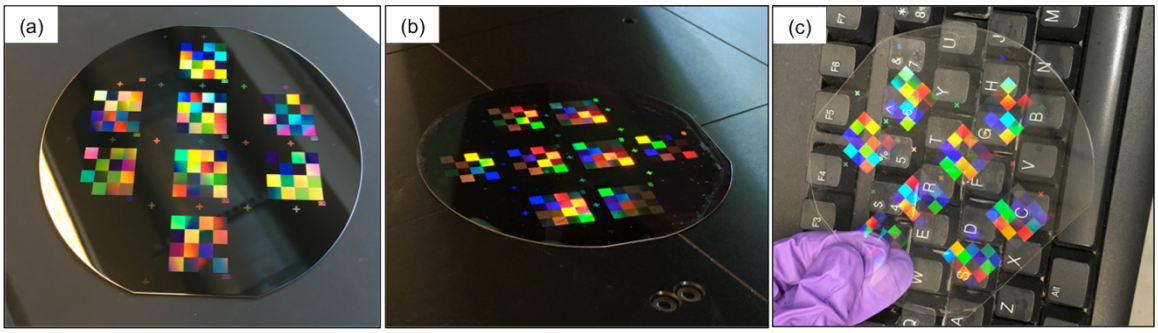

Figure 5.4. Images of (a) Si master mold. (b) ZrO_2 mold on a Si wafer. (c) PMMA inverse structures of the ZrO_2 master on a PET substrate.

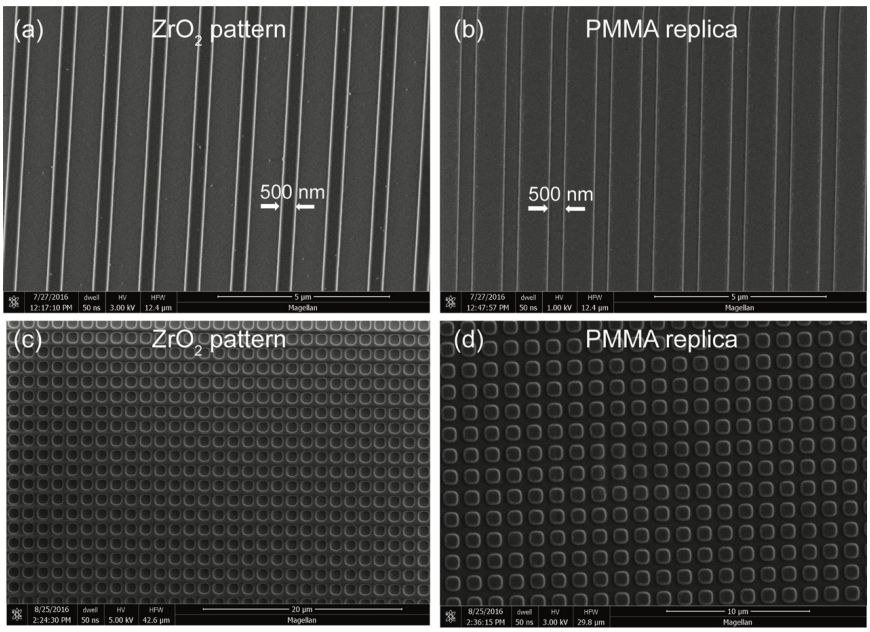

Figure 5.5. SEM micrographs of (a) imprinted ZrO_2 line pattern (width: 500 nm, pitch: 1300 nm), (b) PMMA replica of the ZrO_2 line pattern, (c) imprinted ZrO_2 hole pattern, (d) PMMA replica of the ZrO_2 hole pattern. Thermal-NIL was conducted to obtain PMMA replicas.

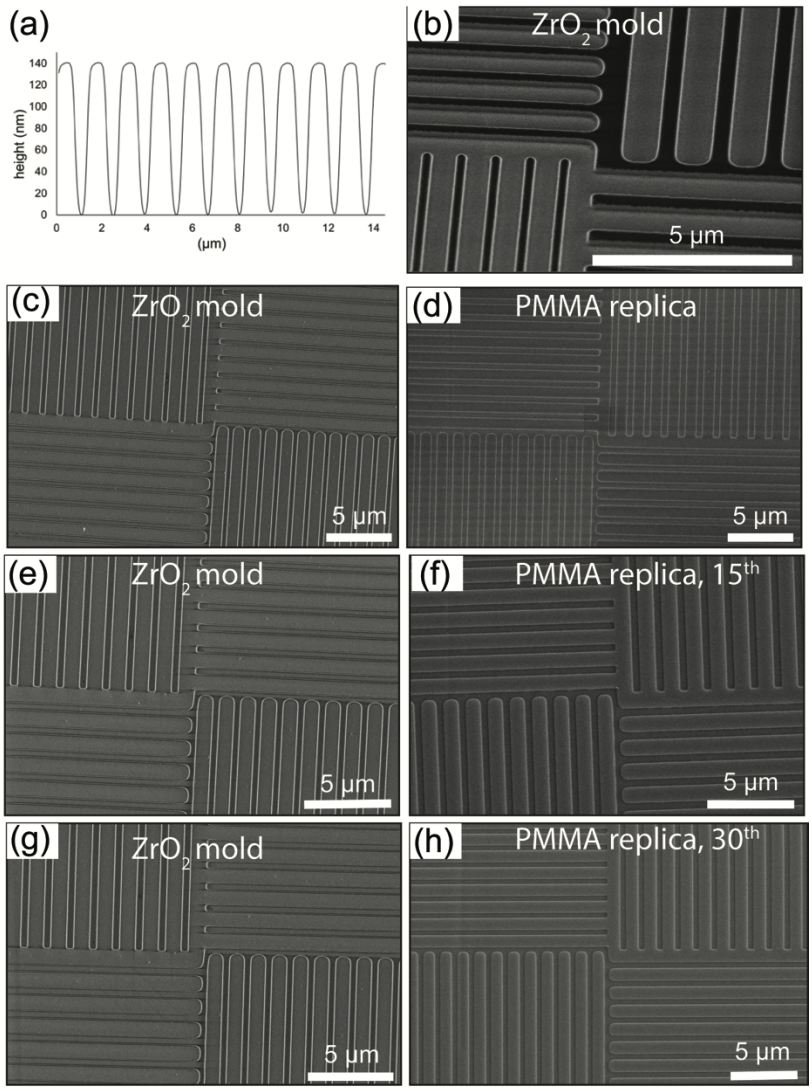

Figure 5.6. (a) Height profile of the ZrO_2 mold. SEM micrographs of (b) patterned ZrO_2 nanoparticles on Si wafer using solvent-assisted soft NIL, 45° tilted, (c) top view, (d) inverse PMMA structures using hard ZrO_2 mold via thermal NIL. (e) The same ZrO_2 mold after 15 consecutive imprints. (f) Inverse PMMA structures as the 15th replica. (g) The same ZrO_2 mold after 30 consecutive imprints. (g) Inverse PMMA structures as the 30th replica.

Sharklet AF^{TM} surfaces are one of the micropatterned antifouling surfaces which have been commercialized and applied on catheters to reduce bacterial attacment[33,34]. However, the primary challenge limiting the mass production of Sharklet AF^{TM} patterned surfaces is the short lifetime of the current nickel molds. To address this problem, ZrO_2

shark-skin patterns were imprinted on a rough steel substrate and annealed at 500°C to obtain a hard ZrO_2 mold which is used for the next imprints. Herein, ZrO_2 shark-skin-patterned surfaces (height: 2μm, width: 1μm, spacing: 3 μm) had only 33% shrinkage in height compared to the height of the Silicon master mold (height: 3 μm, width: 2μm, pitch: 2μm). **Figure 5.7** shows SEM images of a ZrO_2 shark-skin-patterned surface and a PMMA inverse shark-skin patterned surface fabricated using the ZrO_2 mold. The SEM images demonstrate the ability of the ZrO_2 mold to precisely replicate mold features ranging from μm to nm size scales. These results suggest that ZrO_2 structures have high strength and durability, making them ideal for using a master mold for thermal imprinting. Moreover, ZrO_2 can be patterned using the soft PDMS mold onto a variety of substrates including curved and flexible substrates, such as on the watch glass is shown in **Figure 5.7e**, and the Kapton film shown in **Figure 5.7f**.

To make NP-based imprints on curved surfaces, microtransfer molding (μTM)[7] is conducted. A soft PDMS mold was coated with ZrO_2 NP dispersion (5-25 wt% in PGMEA) and the ZrO_2 coated PDMS was placed conformally onto a curved glass. Pattern transfer was successfully made in less than a minute using only PGMEA (considered a highly volatile solvent) at room temperature. ZrO_2 structural color patterns on a curved glass are shown in **Figure 5.7e**. Imprinting time can be adjusted using a mixture of solvents or different coating techniques.

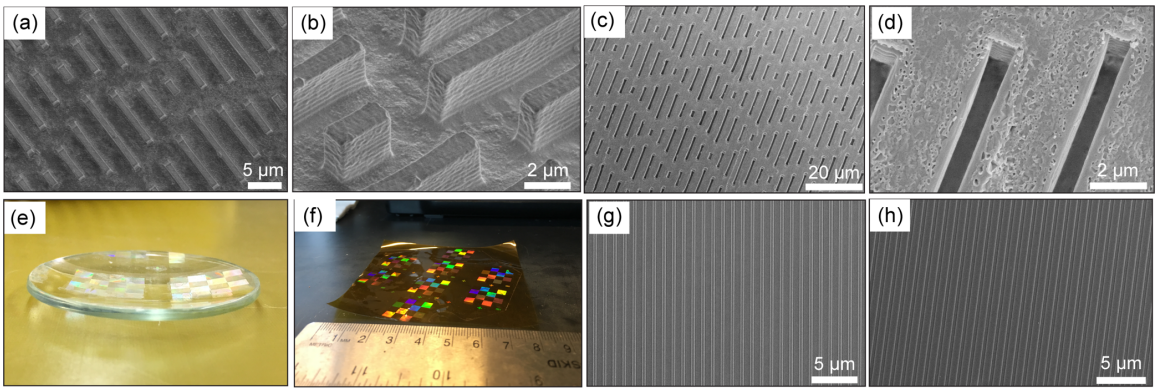

Figure 5.7. SEM images of (a) patterned ZrO_2 NPs on steel using solvent-assisted soft NIL, (b) higher magnification with 45° tilt, (c) inverse PMMA structures using hard ZrO_2 mold via thermal NIL, and (d) higher magnification. (f) Digital photos of ZrO_2 imprint on a curved watch glass (e) Digital photo of ZrO_2 master mold on Kapton film. SEM images of (g) patterned metal oxide nanoparticles on Kapton film, (h) and inverse PMMA structures using hard metal oxide mold via thermal NIL.

The high surface roughness of (commercially available) steel limits the imprinting of nanofeatures. To overcome this problem, planarization of the steel was conducted with the ZrO_2 dispersion using solution deposition planarization technique[35]. After each spin coating step, the coating was sintered before the next coating. A layer-by-layer coating was repeated until the surface roughness was reduced sufficiently. Therefore, crack-free NP-based thick coatings were fabricated with the thicknesses exceeding critical crack thicknesses.[36] The surface profile of the bare steel substrate and after each coating step are shown in **Figure 5.8**. The surface roughness of the steel was able to be decreased from 280 nm to 33 nm after 3-4 consecutive coatings (**Figure 5.9b**). Then, ZrO_2 nanopatterned lines were imprinted on the planarized steel and we obtained a hard, ZrO_2 nanopatterned mold on the steel substrate. Replicated PMMA nanopatterned lines were successfully obtained using the ZrO_2 mold on steel (**Figure 5.9d**).

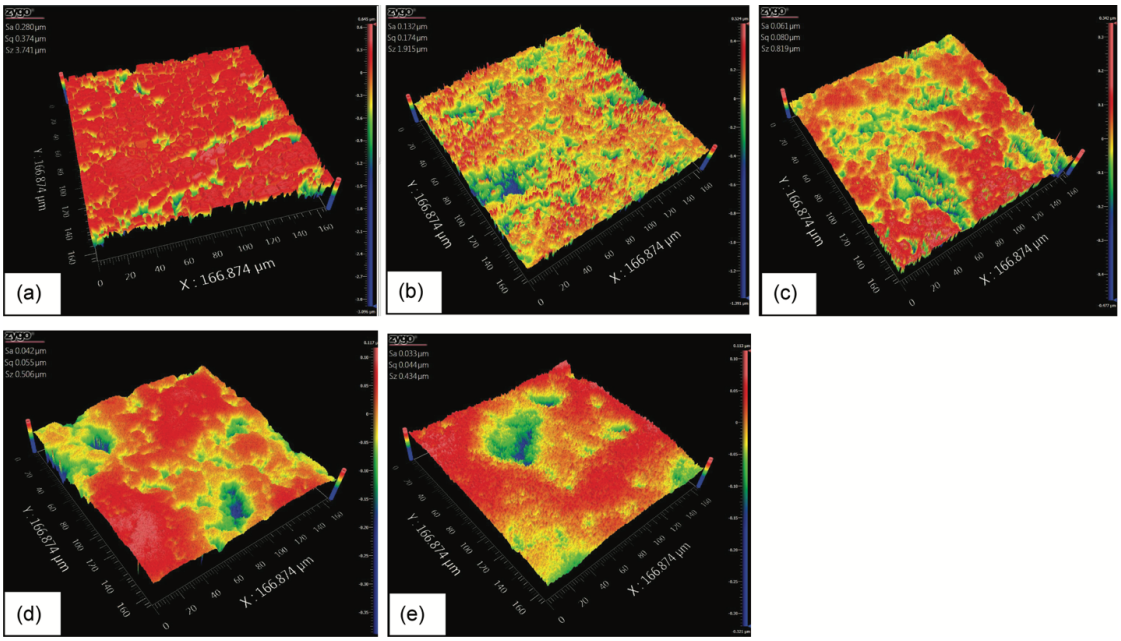

Figure 5.8. Surface profile images of (a) a bare steel surface. (b) After 1st coating layer on the steel. (c) After 2nd coating layer on the steel. (d) After 3rd coating layer on the steel. (e) After 4th coating layer on the steel.

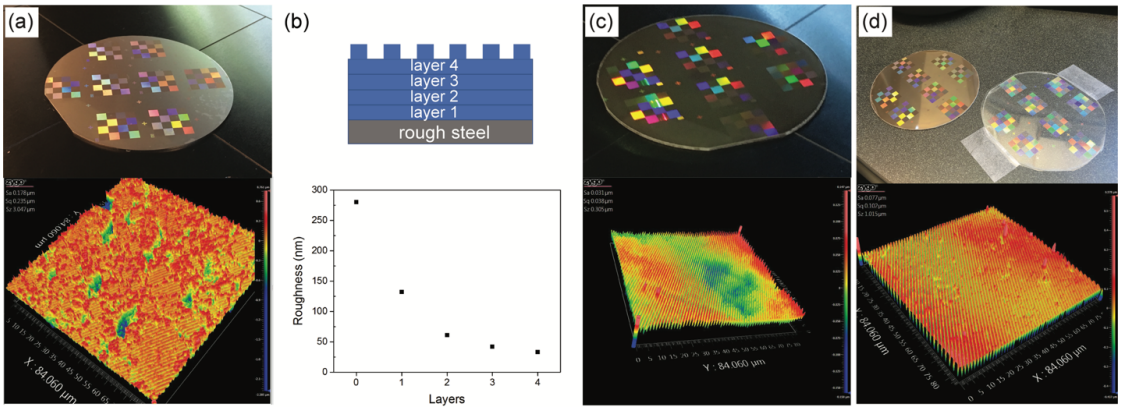

Figure 5.9. (a) Digital photo and optical profile of nanopatterned ZrO_2 on a rough steel substrate. (b) Roughness versus the number of planarizing coatings. (c) Digital photo and optical profile of nanopatterned ZrO_2 on the planarized steel substrate, and (d) A digital photo of nanopatterned ZrO_2 and polymer replica and optical profile of the polymer replica.

5.3.3 UV-NIL using ZrO_2 Mold

Current molds for UV-NIL lack durability mainly as a result of limited mechanical properties, which in turn limits the fast production of UV-curable, patterned surfaces. ZrO_2 is a transparent material in the UV spectrum and has a high hardness that makes it an ideal mold material for UV-NIL. ZrO_2 shark-skin patterns were imprinted on a glass substrate and annealed at 500°C. NOA, a UV-curable resist, was spin-coated on a PET substrate, the ZrO_2 mold was placed onto the coating, and UV-NIL was successfully conducted, resulting in a replica of the ZrO_2 mold (**Figure 5.10**). There was no visible delamination or contamination on the ZrO_2 mold. Thus, hard ZrO_2 patterns on flexible Kapton substrates can be easily used as molds for UV-NIL in the roll-to-roll NIL process.

Moreover, not only line or shark-skin patterns, but also any arbitrary geometry can be imprinted using the ZrO_2 NP dispersion. ZrO_2 ink concentration and coating conditions were adjusted to obtain the desired thickness for target pattern geometry. We have successfully imprinted pillars, meshes, microlenses, arbitrary shapes, and high aspect ratio structures in ZrO_2. Pattern dimensions were varied from ~100 nm to ~100μm (**Figure 5.11**). For example, **Figure 5.12** shows ZrO_2 imprinted structures with as 2:1, 4:1, and 6:1 aspect ratios, and using the ZrO_2 molds inverse replicated structures in NOA were fabricated via UV-NIL.

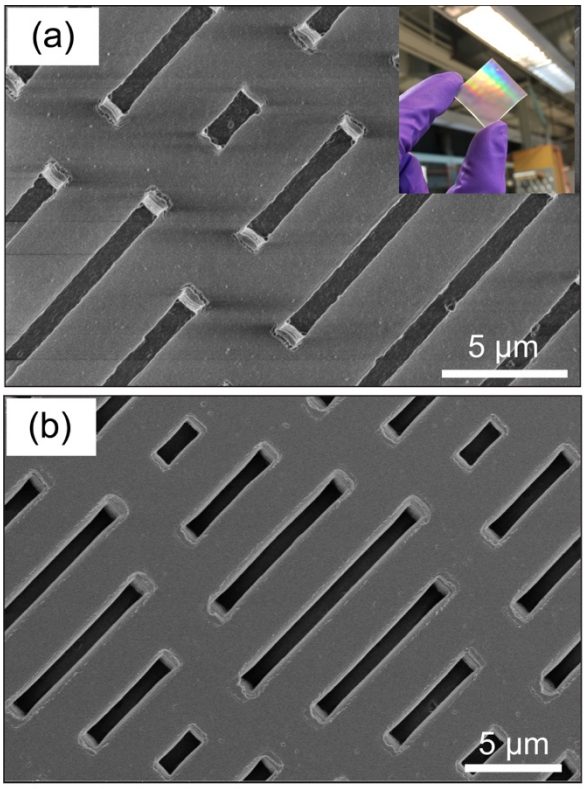

Figure 5.10. (a) SEM image of ZrO_2 shark-skin on glass using solvent-assisted soft NIL and a digital photo of ZrO_2 shark-skin mold on glass (b) SEM image of inverse NOA structures using hard ZrO_2 shark-skin mold via UV-NIL.

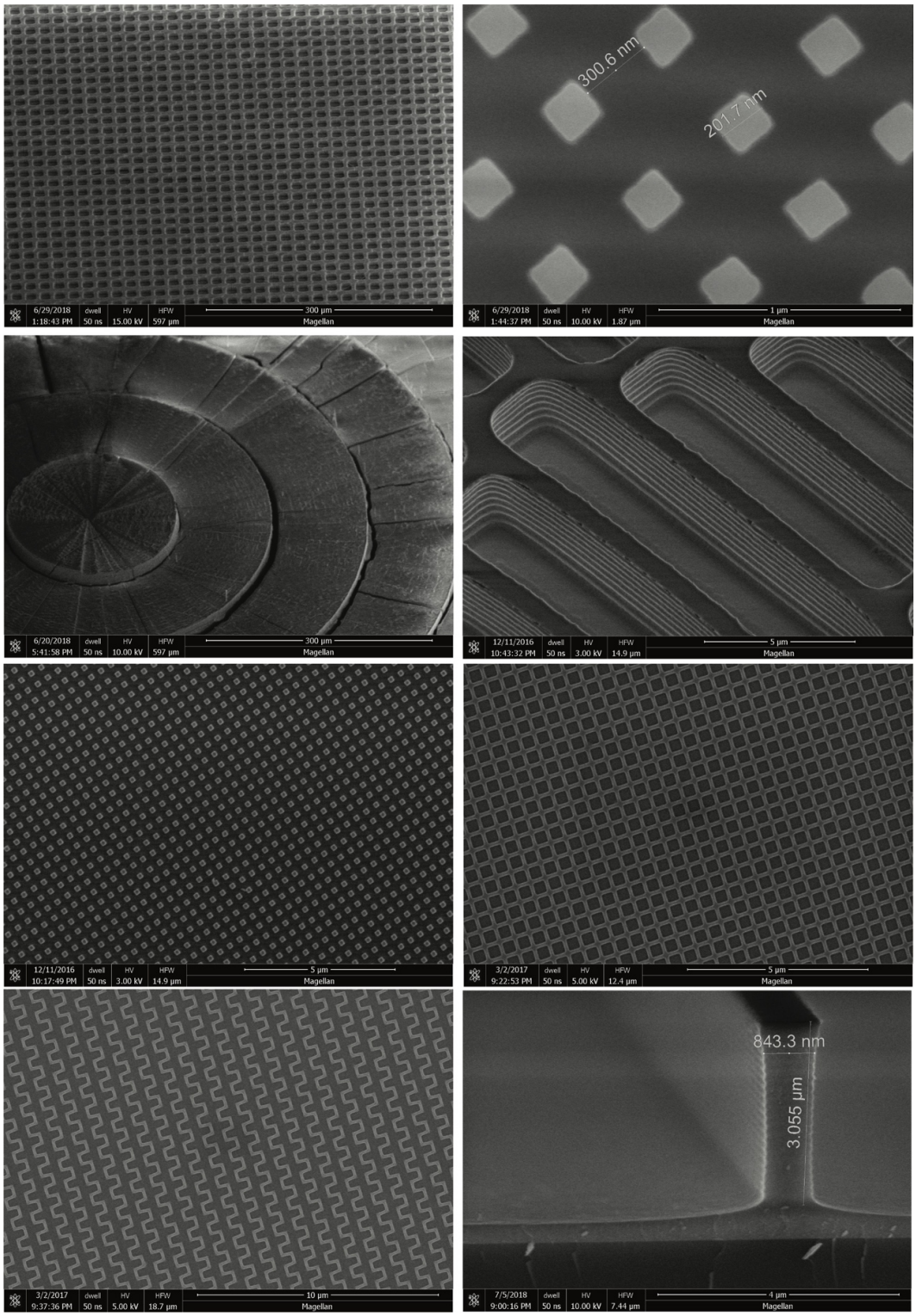

Figure 5.11. SEM micrographs of variety patterned nano/microstructures using ZrO_2 dispersion.

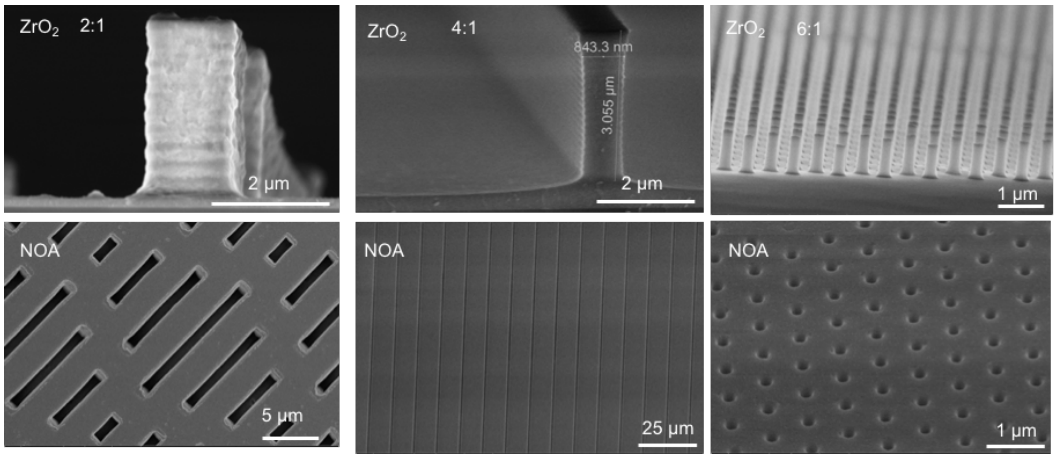

Figure 5.12. SEM micrographs of various aspect ratio structures (2:1, 4:1, and 6:1). Imprinted ZrO2 shark-skin, line pattern, and high aspect ratio pillars and corresponding NOA replicas of the ZrO2 shark-skin, line pattern, and high aspect ratio pillars. UV-NIL was conducted to obtain NOA replicas.

5.3.4 Injection Molding using ZrO_2 Mold

A polished steel block was successfully patterned with a ZrO_2 structural color pattern via solvent-assisted soft NIL. After successful imprinting of the ZrO_2 patterns, the ZrO_2-patterned steel block was post-annealed at 450°C for 2h. Discoloration of the steel block was observed after the post-annealing step due to the characteristics of the steel used in the experiment. To overcome discoloration of the steel, annealing can be done under an inert environment or different grades of steel can be used.

Injection molding was conducted using the ZrO_2-patterned steel insert to fabricate 114,965 replicas with 15.2 s cycle time. Crack generation and delamination can often occur due to defects in the mold. There was no measurable delamination even near the defect sites (**Figure 5.13)**. This result is due to the great anti-wear characteristics of ZrO_2, which result from its high hardness and modulus. An SEM image of the ZrO_2 mold insert after 114,965 cycles is shown in **Figure 5.13c**. There was no line breakage or contamination. In such a repeatable and fast process, some degree of crystallization of ZrO_2 might have occurred; however, a more uniform ZrO_2 imprint on a steel insert would exhibit a uniform

crystallization and better optical impression. Successfully replicated patterned ABS polymers are also shown in **Figure 5.13d-g**. The line height of the ZrO_2 patterned steel insert and molded ABS patterned replica was measured in AFM and the height was determined to be ~170 nm (**Figure 5.14**). A defect in the patterned ABS was imaged in the optical microscope at 28,751st, 50,990th, 87,380th, and 114,965th replica and there were no measurable differences. The successful results exhibit that ZrO_2 patterned steel inserts can be a low-cost and durable mold for the injection molding process.

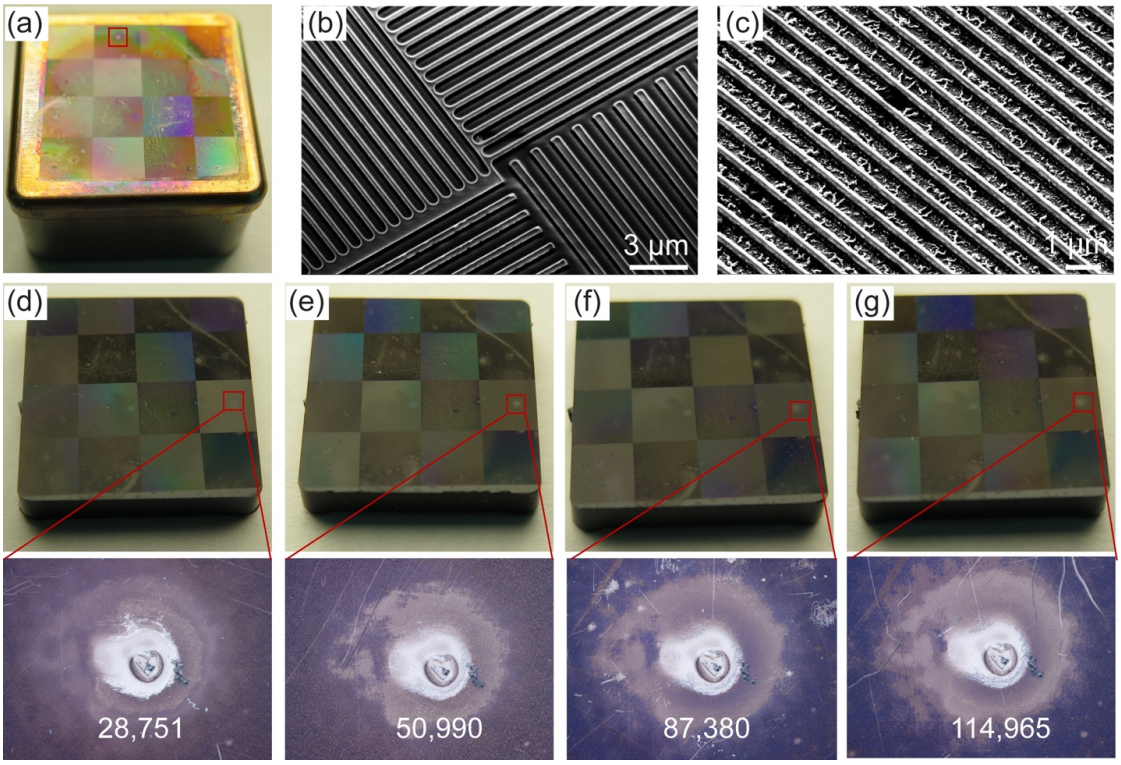

Figure 5.13. (a) Digital photo of patterned ZrO_2 nanoparticles on a steel block using solvent-assisted soft NIL. SEM micrographs of patterned ZrO_2 nanoparticles on a steel block (b) before injection molding (c) after 114,965 injection molding cycles. Digital photos and optical micrographs of nanopatterned polymer replicas (d) after 28,751 cycles, (e) after 50,990 cycles, (f) after 87,380 cycles, and (g) after 114,965 cycles.

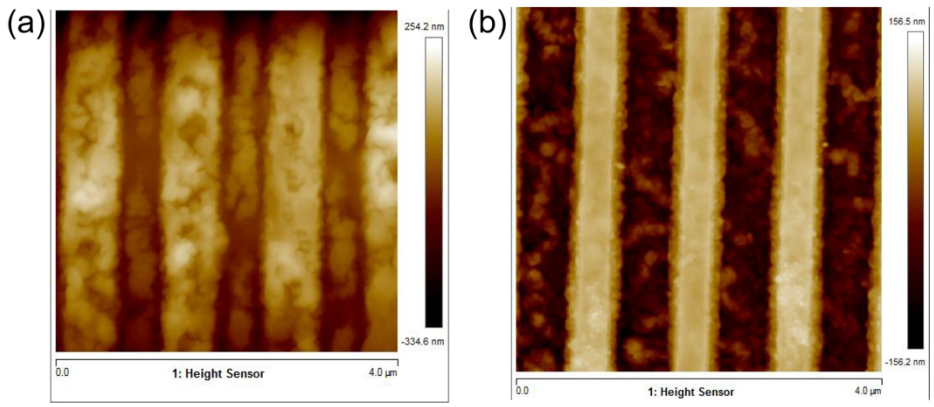

Figure 5.14. AFM height profile of (a) ZrO_2 patterned steel insert, (b) a molded ABS polymer. The height was determined to be ~170 nm for both ZrO_2 mold and replicated polymer.

5.4 Conclusions

Hard and durable micro/nano-patterned ZrO_2 molds were fabricated using a cost-effective and straightforward solvent-assisted soft NIL method. The hardness and reduced modulus of the ZrO_2 films were increased up to 11 GPa and 120 GPa, respectively. Solution deposition planarization was conducted to reduce the roughness of the steel from 280 nm to 33 nm. Thus, nanopatterned surfaces were obtained on the planarized steel surfaces. A hard transparent ZrO_2 mold was successfully replicated using thermal-NIL and UV-NIL; initial roll-to-roll (R2R) results indicate excellent potential for R2R-NIL processing for high volume production. Moreover, the ZrO_2 patterned steel insert was successfully used for injection molding to produce 115,000 polymer replicas without any deformation. Our technique is solution processable, can be applied to any surfaces from flat to curved as well as from smooth to rough substrates, and can be used for many nano-replication technologies.

5.5 References

(1) Guo, L. J. Recent Progress in Nanoimprint Technology and Its Applications. *J. Phys. D. Appl. Phys.* **2004**, *37* (11).

(2) Kane, R. S.; Takayama, S.; Ostuni, E.; Ingber, D. E.; Whitesides, G. M. Patterning Proteins and Cells Using Soft Lithography. *Biomaterials* **1999**, *20* (23), 2363–2376.

(3) Genevet, P.; Capasso, F.; Aieta, F.; Khorasaninejad, M.; Devlin, R. Recent Advances in Planar Optics: From Plasmonic to Dielectric Metasurfaces. *Optica* **2017**, *4* (1), 139.

(4) Zhao, N.; Wang, Z.; Cai, C.; Shen, H.; Liang, F.; Wang, D.; Wang, C.; Zhu, T.; Guo, J.; Wang, Y.; Liu, X.; Duan, C.; Wang, H.; Mao, Y.; Jia, X.; Dong, H.; Zhang, X.; Xu, J. Bioinspired Materials: From Low to High Dimensional Structure. *Adv. Mater.* **2014**, *26* (41), 6994–7017.

(5) Nie, Z.; Kumacheva, E. Patterning Surfaces with Functional Polymers. *Nat. Mater.* **2008**, *7* (4), 277–290.

(6) van Assenbergh, P.; Meinders, E.; Geraedts, J.; Dodou, D. Nanostructure and Microstructure Fabrication: From Desired Properties to Suitable Processes. *Small* **2018**, *1703401*, 1703401.

(7) Xia, Y. N.; Whitesides, G. M. Soft Lithography. *Annu. Rev. Mater. Sci.* **1998**, *37* (5), 551–575.

(8) Ahn, S. H.; Guo, L. J. Large-Area Roll-to-Roll and Roll-to-Plate Nanoimprint Lithography: A Step toward High-Throughput Application of Continuous Nanoimprinting. *ACS Nano* **2009**, *3* (8), 2304–2310.

(9) Stormonth-Darling, J. M.; Gadegaard, N. Injection Moulding Difficult Nanopatterns with Hybrid Polymer Inlays. *Macromol. Mater. Eng.* **2012**, *297* (11), 1075–1080.

(10) Højlund-Nielsen, E.; Clausen, J.; Mäkela, T.; Thamdrup, L. H.; Zalkovskij, M.; Nielsen, T.; Li Pira, N.; Ahopelto, J.; Mortensen, N. A.; Kristensen, A. Plasmonic Colors: Toward Mass Production of Metasurfaces. *Adv. Mater. Technol.* **2016**, *1* (7), 1–8.

(11) Schift, H. Nanoimprint Lithography: An Old Story in Modern Times? A Review. *J. Vac. Sci. Technol. B Microelectron. Nanom. Struct.* **2008**, *26* (2), 458.

(12) Guo, L. J. Nanoimprint Lithography: Methods and Material Requirements. *Adv. Mater.* **2007**, *19* (4), 495–513.

(13) Kwon, B.; Kim, J. H. Importance of Molds for Nanoimprint Lithography : Hard , Soft , and Hybrid Molds. **2016**, *2016*.

(14) Schift, H.; Urwyler, P.; Kristiansen, P. M.; Gobrecht, J. Nanoimprint Lithography Process Chains for the Fabrication of Micro- and Nanodevices. *J. Micro/Nanolithography, MEMS, MOEMS* **2014**, *13* (3), 031303.

(15) Zhang, N.; Srivastava, A.; Kirwan, B.; Byrne, R.; Fang, F.; Browne, D. J.; Gilchrist, M. D. Manufacturing Microstructured Tool Inserts for the Production of Polymeric Microfluidic Devices. *J. Micromechanics Microengineering* **2015**, *25* (9), 095005.

(16) Zhang, N.; Srivastava, A. P.; Browne, D. J.; Gilchrist, M. D. Performance of Nickel and Bulk Metallic Glass as Tool Inserts for the Microinjection Molding of Polymeric Microfluidic Devices. *J. Mater. Process. Technol.* **2016**, *231*, 288–300.

(17) Tosello, G.; Hansen, H. N.; Gasparin, S.; Albajez, J. A.; Esmoris, J. I. Surface Wear of TiN Coated Nickel Tool during the Injection Moulding of Polymer Micro Fresnel Lenses. *CIRP Ann. - Manuf. Technol.* **2012**, *61* (1), 535–538.

(18) Kumar, G.; Tang, H. X.; Schroers, J. Nanomoulding with Amorphous Metals. *Nature* **2009**, *457* (7231), 868–872.

(19) Hobæk, T. C.; Matschuk, M.; Kafka, J.; Pranov, H. J.; Larsen, N. B. Hydrogen Silsesquioxane Mold Coatings for Improved Replication of Nanopatterns by Injection Molding. *J. Micromechanics Microengineering* **2015**, *25* (3), 035018.

(20) Zhang, N.; Byrne, C. J.; Browne, D. J.; Gilchrist, M. D. Towards Nano-Injection Molding. *Mater. Today* **2012**, *15* (5), 216–221.

(21) Saleem, M. R. Hydrogen Silsesquioxane Resist Stamp for Replication of Nanophotonic Components in Polymers. *J. Micro/Nanolithography, MEMS, MOEMS* **2012**, *11* (1), 013007.

(22) Park, H. H.; Zhang, X.; Lee, S. W.; Kim, K. D.; Choi, D. G.; Choi, J. H.; Lee, J. Y.; Lee, E. S.; Park, H. H.; Hill, R. H.; Jeong, J. H. Facile Nanopatterning of Zirconium Dioxide Films via Direct Ultraviolet-Assisted Nanoimprint Lithography. *J. Mater. Chem.* **2011**, *21* (3), 657–662.

(23) Ganesan, R.; Dumond, J.; Saifullah, M. S. M.; Lim, S. H.; Hussain, H.; Low, H. Y. Direct Patterning of TiO2 Using Step-and-Flash Imprint Lithography. *ACS Nano* **2012**, *6* (2), 1494–1502.

(24) Zhang, N.; Chu, J. S.; Byrne, C. J.; Browne, D. J.; Gilchrist, M. D. Replication of Micro/Nano-Scale Features by Micro Injection Molding with a Bulk Metallic Glass Mold Insert. *J. Micromechanics Microengineering* **2012**, *22* (6).

(25) Mehner, A.; Zoch, H.-W.; Datchary, W.; Pongs, G.; Kunzmann, H. Sol-Gel Coatings for High Precision Optical Molds. *CIRP Ann. - Manuf. Technol.* **2006**, *55* (1), 589–592.

(26) Arisoy, F. D.; Kolewe, K. W.; Homyak, B.; Kurtz, I. S.; Schi, J. D.; Watkins, J. J. Bioinspired Photocatalytic Shark-Skin Surfaces with Antibacterial and Antifouling

Activity via Nanoimprint Lithography. *ACS Appl. Mater. Interfaces* **2018,** 10 (23), 20055–20063.

(27) Li, W.; Zhou, Y.; Howell, I. R.; Gai, Y.; Naik, A. R.; Li, S.; Carter, K. R.; Watkins, J. J. Direct Imprinting of Scalable , High-Performance Woodpile Electrodes for Three-Dimensional Lithium-Ion Nanobatteries. *ACS Appl. Mater. Interfaces* **2018**, *10* (6), 5447–5454.

(28) Li, W.; Christiansen, T. L.; Li, C.; Zhou, Y.; Fei, H.; Mamakhel, A.; Iversen, B. B.; Watkins, J. J. High-Power Lithium-Ion Microbatteries from Imprinted 3D Electrodes of Sub-10 Nm LiMn2O4/Li4Ti5O12 Nanocrystals and a Copolymer Gel Electrolyte. *Nano Energy* **2018**, 52, 431–440.

(29) Beaulieu, M. R.; Hendricks, N. R.; Watkins, J. J. Large-Area Printing of Optical Gratings and 3D Photonic Crystals Using Solution-Processable Nanoparticle/Polymer Composites. *ACS Photonics* **2014**, *1* (9), 799–805.

(30) Kothari, R.; Beaulieu, M. R.; Hendricks, N. R.; Li, S.; Watkins, J. J. Direct Patterning of Robust 1-D, 2-D and 3-D Crystalline Metal Oxide Nanostructures Using Imprint Lithography and Nanoparticle Dispersion Inks. *Chem. Mater.* **2017**, *29*, 3908−3918.

(31) Hampton, M. J.; Williams, S. S.; Zhou, Z.; Nunes, J.; Ko, D. H.; Templeton, J. L.; Samulski, E. T.; DeSimone, J. M. The Patterning of Sub-500 Nm Inorganic Oxide Structures. *Adv. Mater.* **2008**, *20* (14), 2667–2673.

(32) Gu, Y.; Zhang, L.; Yang, J. K. W.; Yeo, S. P.; Qiu, C. W. Color Generation via Subwavelength Plasmonic Nanostructures. *Nanoscale* **2015**, *7* (15), 6409–6419.

(33) Chung, K. K.; Schumacher, J. F.; Sampson, E. M.; Burne, R. a; Antonelli, P. J.; Brennan, A. B. Impact of Engineered Surface Microtopography on Biofilm Formation of Staphylococcus Aureus. *Biointerphases* **2007**, *2* (2), 89–94.

(34) May, R. M.; Hoffman, M. G.; Sogo, M. J.; Parker, A. E.; O'Toole, G. a; Brennan, A. B.; Reddy, S. T. Micro-Patterned Surfaces Reduce Bacterial Colonization and Biofilm Formation in Vitro: Potential for Enhancing Endotracheal Tube Designs. *Clin. Transl. Med.* **2014**, *3* (1), 8.

(35) Zhou, H.; Chai, F.; Fang, J. Highly Efficient Colloid – Solution Deposition Planarization of Hastelloy Substrate for IBAD-MgO Film. *Res. Chem. Intermed.* **2016**, *42* (5), 4751–4758.

(36) Prosser, J. H.; Brugarolas, T.; Lee, S.; Nolte, A. J.; Lee, D. Avoiding Cracks in Nanoparticle Films. *Nano Lett.* **2012**, *12* (10), 5287–5291.

CHAPTER 6

NANOPATTERNING OF STEEL VIA HARD ZIRCONIA MOLD

6.1 Introduction

Stainless steel (SS), such as 304 and 316, is used in many industrial applications including food processing and pharmaceutical plants because of its strength, wear-resistance, and relatively low-cost. However, fouling of SS surfaces, resulting from bacterial contamination and organic residues, is the biggest threat for product safety, resulting in millions of dollars in costs dedicated to cleaning the SS tanks and pipes in plants daily. The typical cleaning procedure is often referred to as clean-in-place (CIP), which generates a tremendous volume of wastewater.[1] Reducing the amount of wastewater discharge and preventing contamination of foulants is essential instead of treating the contamination.

Variety types of self-cleaning or antifouling surfaces have been fabricated using many different methods, including femtosecond laser ablation[2,3], deposition[4,5], electrochemical etching[8], and therefore micro/nanopatterned surfaces, spray coated, and slippery liquid-infused porous surfaces (SLIPS)[6,7] were obtained. Antifouling coatings, notably polyethylene glycol (PEG) and poly(tetrafluoroethylene) (PTFE), are undesired due to lacking long-term durability and the potential release of toxic chemicals, respectively. For example, Pei et al. reported that SS-PEG substrate could not prevent biofilm formation despite being resistant to protein adsorption.[9] Zhao et al. demonstrated that PTFE coatings, which possess low surface energy, reduced the E. coli attachment by 90% after a 5 h incubation period compared to bare SS 304.[10] However, it has been shown that perfluorochemicals are harmful and accumulate in the body, which limits the use of

fluoro-based chemical in practical applications.[11] There are only a few SLIPS on SS reported for food processing which were fabricated using femtosecond laser ablation and impregnated with lubricating oil. Despite their effectiveness to prevent bacterial contamination and easy cleanability, SLIPS have several disadvantages.[12] First, a shear force for cleaning can remove all the lubricants, subsequently leaving the porous surface open for contamination. Second, the laser ablation fabrication of porous SS surfaces is not practical over a large area.

Bioinspired hierarchical micro/nanopatterned surfaces have been shown to be potential antifouling (e.g., Sharklet AF^{TM}) and self-cleaning (e.g., lotus leaf) surfaces.[13] Antifouling behavior is a result of the structure-property relationship. The fabrication of nanopatterned surfaces in SS has been conducted via several techniques such as pulsed electron beam irradiation, femtosecond laser ablation, and ion-beam etching. However, expensive and long fabrication times make these non-ideal for any large area patterning applications. Alternative, low-cost SS patterning techniques including microextrusion, microforming, and coining/embossing have been reported, but have only demonstrated low resolution features, with a minimum feature size of 10 μm.[14] Moreover, the fabrication of current molds (e.g., diamond and silicon carbide (SiC)) to make patterned steel surfaces is also an expensive and time-consuming process.[15,16] Thus, it is extremely desirable to develop a scalable method to fabricate high resolution, micro/nanopatterned SS surfaces at a low cost.

We present a straightforward and cost-effective SS patterning technique using a hard micro/nanopatterned zirconium dioxide (ZrO_2) mold. A ZrO_2 patterned mold was fabricated via a solvent-assisted imprinting technique using a ZrO_2 nanoparticle (NP)-based ink on a zirconia substrate, and then annealed to obtain a super-hard ceramic

patterned-mold. The ZrO_2 patterned mold was pressed into a 304 SS substrate using a hydraulic press and replicated patterns were obtained in the SS. As expected, restorative stress from residual elastic stress in the SS substrate lessened replication fidelity; however, we demonstrated that hard patterned ZrO_2 molds offer low-cost nanofabrication of hard steel sheets with up to 25% pattern transfer yield at room temperature.

6.2 Experimental Section

6.2.1 Materials

All materials were used as-received without further purification. Zirconium dioxide (ZrO_2 50wt% in ethanol (EtOH)) nanoparticles (NPs) (5 nm in diameter) were purchased from Pixelligent (Baltimore, MD). Poly(tetrafluoroethylene) (PTFE) filters (0.45 μm) and EtOH were purchased from Fisher Scientific (Hampton, NH). ZrO_2 substrates (3.5mol.% YSZ, 10x10x0.5 mm, one side polished) were purchased from MTI corporation (Richmond, CA). Stainless steel sheets (304 (#8 polished, 0.4 mm in thickness) and 316L (#8 polished, 1.02 mm) were purchased from Stainlesssupply (Monroe, NC). SUS304 (polished, 0.02 mm in thickness) was purchased from TDC Corporation (Miyagi, Japan). Heptadecafluoro-1,1,2,2-tetrahydrodecyl) dimethylchlorosilane was acquired from Gelest (Morrisville, PA). Sylgard 184 silicone elastomer kit (polydimethylsiloxane (PDMS)) was purchased from Dow Corning (Midland, MI). 1,2 propanediol and propylene glycol monomethyl ether acetate (PGMEA) were purchased from Sigma-Aldrich (St. Louis, MO).

6.2.2 Methods

6.2.2.1 ZrO_2 Ink Formulation and ZrO_2 Master Mold Fabrication

To prepare PDMS molds, Sylgard 184 was mixed in a 1:10 ratio of curing agent to base, then poured onto various silicon/nickel master molds and placed into an oven to be crosslinked at 70^{o}C for 3 h. The 50wt% ZrO_2 dispersion was diluted with ethanol and 1,2 propanediol down to 25-10 wt%. The mixture was sonicated for 15 min and a stable dispersion was obtained. Substrates were cleaned with hexane, acetone, and IPA respectively and then treated with O_2 plasma for 5-10 min. The ZrO_2 dispersion was spin coated onto the substrate, and then a PDMS mold was placed onto the top of the coating. The stamp/coating assembly was placed on a hot plate (50°C) for a few minutes to remove all residual solvent. Then, the PDMS mold was peeled off and the patterned structure was obtained on the substrate. The patterned surfaces were annealed at 300^{o}C - 1000^{o}C for 2 hours. The annealed patterned surface was then fluorinated achieve a non-stick surface, to be suitable for the subsequent imprints. The same procedure was conducted on various types of substrates such as steel, ceramics, and tungsten carbide. The annealing temperature was limited based on the substrate material.

6.2.2.1 Patterning of A Steel Using the ZrO_2 Mold

A hydraulic press was used for patterning steel. A piece of rubber was placed under the steel sheet (SS 304), and a ZrO_2 patterned mold was placed onto the steel. Pattern transfer into the steel was conducted under 2000 PSI (with up to 5 s hold, at a constant pressure rate). Using the same ZrO_2 mold, 3-4 additional pattern transfers were conducted. All the pattern transfers into the steel were performed at room temperature (20°C).

6.2.3 Characterization

A diluted ZrO_2 dispersion was drop casted on carbon-coated copper grids and transmission electron microscopy (TEM) imaging was performed in bright field imaging mode using a JEOL 2000 FX. Mechanical properties of the ZrO_2 films were determined using a Hysitron TriboIndenter (TI 950) by averaging 30 indentations obtained under rate control (10 μN/s) using a Berkovich tip (100 nm) for each film. Imprinted patterned surfaces were characterized by scanning electron microscopy (SEM) using an FEI Magellan 400 FESEM. 3D optical profilometry (Zygo, Nexview) was used to measure feature dimensions.

6.3 Results and Discussion

ZrO_2 NPs were imprinted via a solvent-assisted patterning technique using inks comprised of ZrO_2 nanoparticles (NPs). The schematic process of the solvent-assisted imprinting technique is shown in **Figure 1a.** Imprinted patterns were annealed at 1000°C for 2h to obtain a hard and durable mold. Direct imprinting of ZrO_2 NPs in a variable geometry has been shown in the previous chapter (Chapter 5), where NP characteristics and imprinting conditions were discussed in detail. The hardness and modulus values of annealed ZrO_2 were determined to be 11 ± 2 GPa and 120 ± 10 GPa, respectively. As an example, the shark-skin pattern was imprinted in ZrO_2 on a ceramic substrate, and used as a mold for the pattern transfer.

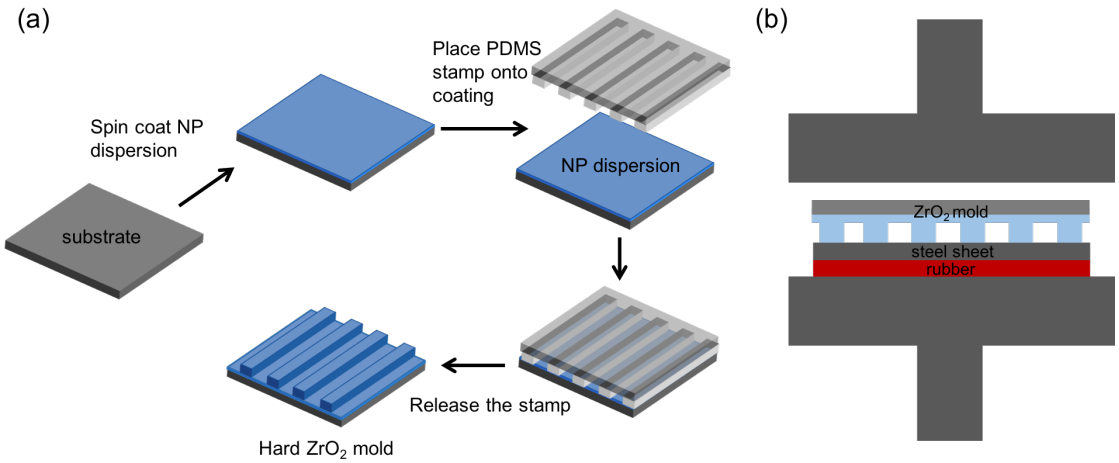

Figure 6.1. Schematic representation of the fabrication process of (a) ZrO_2 patterned mold using soft PDMS stamp, (b) patterned steel using the hard ZrO_2 patterned mold.

The pattern transfer into an SS304 steel substrate was conducted using a hydraulic press at room temperature (20°C). A scheme of the embossing process is shown in **Figure 1b,** in which a thin rubber sheet was placed between the steel substrate and press surface to ensure conformal contact between the ZrO_2 mold and the steel substrate. A ZrO_2 shark-skin-patterned mold was pressed into the steel substrate and the single mold was able to be used more than 3 times without noticeable damage. Digital images of the ZrO_2 shark-skin-patterned mold and consecutive pattern transfers into the steel substrates are shown in **Figure 2**.

SEM micrographs and the feature dimensions of the ZrO_2 shark-skin-patterned surfaces are shown in **Figure 3a and b**. The features were successfully replicated uniformly in size and shape. The height of the ZrO_2 features was determined to be 2 µm. **Figure 3c and d** shows that patterned steel had an approximately 500 nm depth after pressing at 2000 PSI at 20°C. This lessened replication fidelity at room temperature was expected due to characteristics of the steel and pressing conditions. Full replication was

constrained because of many influences including springback, which is caused by elastic recovery of the steel. Moreover, the flow of the steel depends on the geometry of the pattern, hardness and grain size of the steel being used, pressing pressure, and pressing rate.[14] Microforming of steel has been discussed in detail recently; however, there is no definitive study on sub- micron feature deformation in steel.[14]

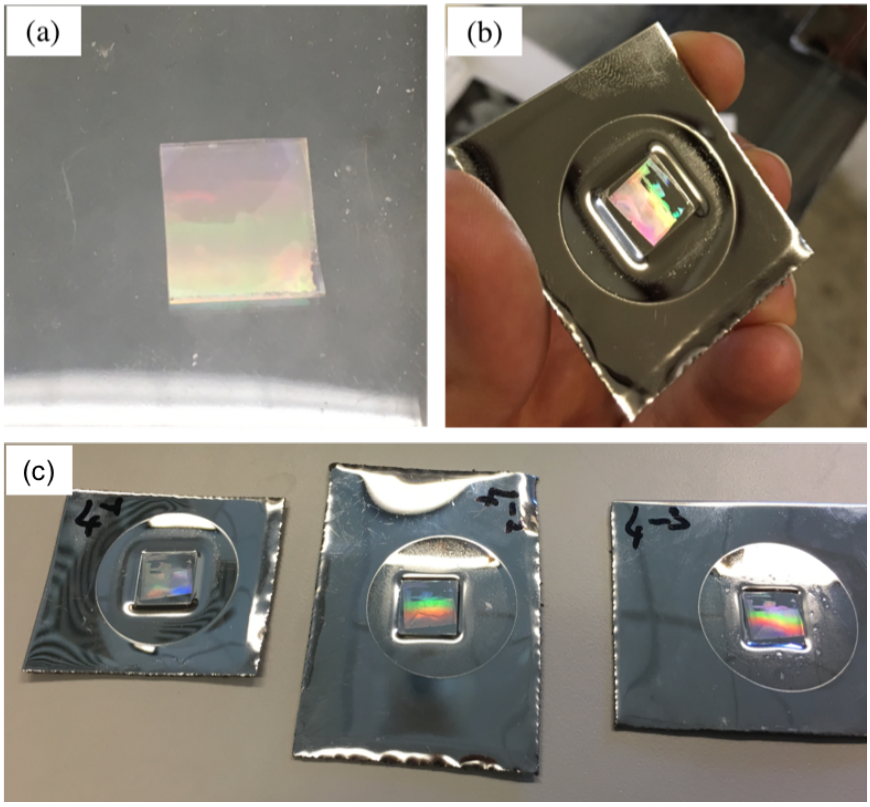

Figure 6.2. Digital images of (a) ZrO_2 patterned mold, (b) steel patterned surface, (c) subsequent patterning of the steels using the single ZrO_2 patterned mold.

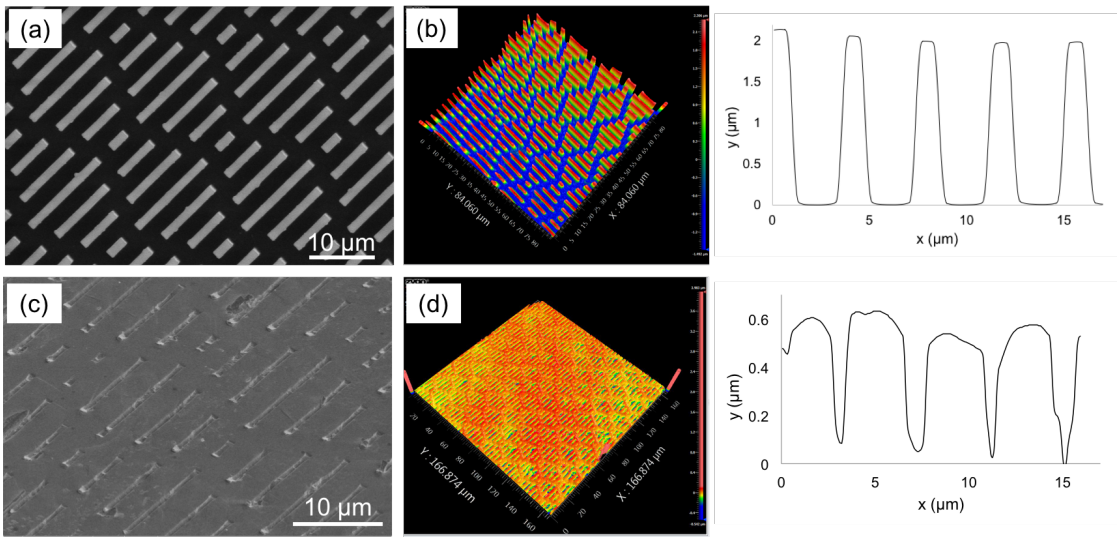

Figure 6.3. SEM micrographs, optical and height profilometry of the (a,b) ZrO_2 patterned mold, (c.d) patterned steel substrates using the ZrO_2 mold.

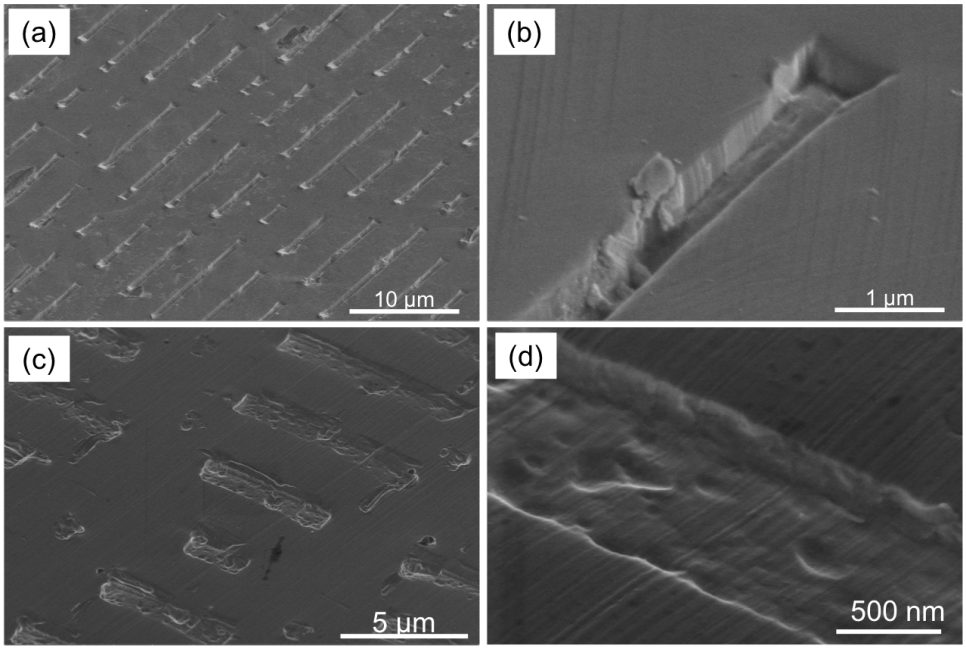

Figure 6.4. SEM micrographs of patterned steel surfaces from different spots (a,c) low mag, (b.d) high mag.

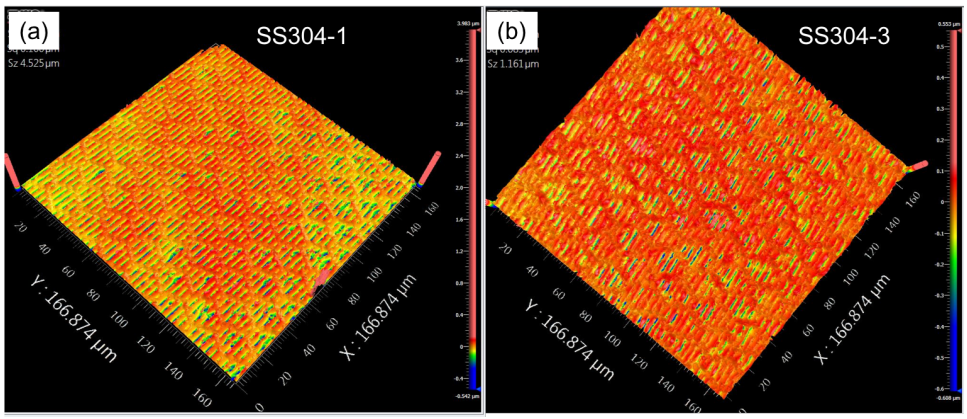

Figure 6.5. Optical profilometry of the patterned steel surfaces using a single ZrO_2 patterned mold. (a) The first patterned steel, SS304-1, (b) The third patterned steel, SS304-3

Springback is affected by the thickness of the steel substrate.[17] To further study this effect, we compared the pattern transfer quality of the two steel substrates with different thicknesses, SS304 (0.4 mm) and SUS304 (0.02 mm). **Figure 6** shows the optical profilometry of SS304 and SUS304 after pattern transfer under the same embossing conditions. The height of the features in SUS304 was determined to be approximately 200-400 nm, whereas the height of the features in SS304 was ~500-600 nm. This result suggested that as the thickness of the steel is decreased, the amount of the springback increases. Diehl et al. reported that above a thickness of 0.2 mm, there is a positive correlation between springback and thickness due to the increasing share of surface grains; however, below 0.2 mm thickness, springback increases with decreasing the thickness due to increased strain gradient.[18]

In order to gain greater insight into the effect of thickness of steel during pressing, we conducted a nanoindentation test on SS304 and SUS304. Load versus displacements curves of SS304 and SUS304 were compared under the same conditions (load: 2000µN and rate: 200 µN/s). Contact depth in SUS304 was only approximately 60 nm, while SS304

had a contact depth of approximately 100 nm. Thus, nanomechanical analysis of SS304 and SUS304 confirmed that the flow of steel identical loading conditions are highly dependent on the thickness of the steel substrates. Moreover, nanoindentation hardness values of SS304 and SUS304 were determined to be 3.9 ± 0.3 GPa and 6.1 ± 0.7 GPa, respectively, which were significantly less than the hardness value of the ZrO_2 mold (11 ± 2 GPa).

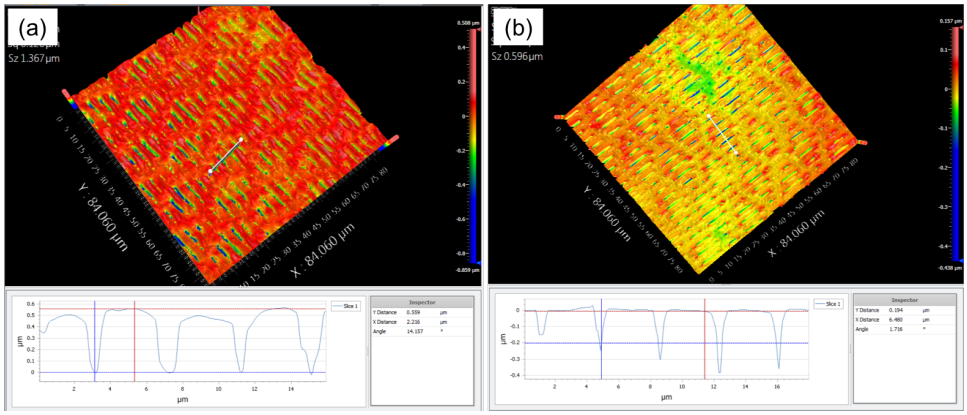

Figure 6.6. Comparison of steel sheet thicknesses under the same pressing conditions. Height profiles of steel surfaces (a) patterned SS304, (b) patterned SUS 304.

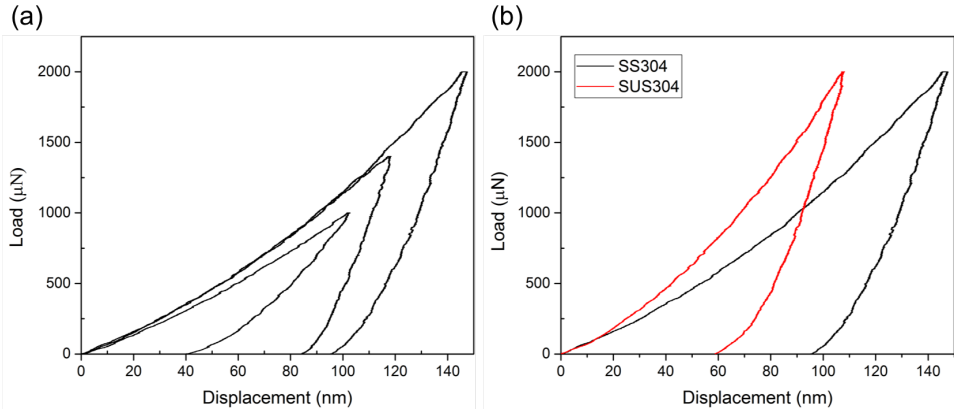

Figure 6.7. Load versus displacement curves of (a) SS304 under rate control (200 µN/s), (b) SS304 versus SUS304.

Lastly, uneven pressure distribution during pressing may be the cause of non-uniform pattern transfer into the steel. The resulting frictional stress during nanopattern

transfer is much higher compared to embossing of features with micron or larger sizes, and could be decreased by using a lubricant.[19] In the future, compression/embossing tests into steel can be conducted using heat-assisted embossing or compression. At elevated temperatures such as at 680°C, the springback effect can be decreased, and a better replication quality can be obtained in the steel.[20] In summary, this study demonstrates that by using a hard ZrO_2 mold, nanopatterning of steel is feasible at low-cost. We believe that this research will attract significant attention in scientific and commercial areas.

6.4 Conclusions

To the best of our knowledge, this work represents the first reported scalable method for fabricating nanopatterned steel surfaces at room temperature. The hard micro/nanopatterned ZrO_2 mold enabled deformation of the steel substrate/surface, and we were therefore able to obtain micro/nanopatterned steel surfaces. The results indicated that the thickness of steel substrates is as critical as the characteristics of the steel, embossing temperature, and pattern geometry. Our hard ZrO_2 mold and technique offer the possibility of large-area, low-cost patterning of steel and can be used for many applications including self-cleaning and antifouling stainless steel surfaces, which would be of specific interest to the food processing and pharmaceutical industries.

6.5 References

(1) Simeone, A.; Woolley, E.; Rodriguez, A. Z.; Rahimifard, S. Eco-Intelligent Monitoring for Fouling Detection in Clean-in-Place. *Procedia CIRP* **2017**, *62* (4), 500–505.

(2) Vorobyev, A. Y.; Guo, C. Direct Femtosecond Laser Surface Nano/Microstructuring and Its Applications. *Laser Photonics Rev.* **2013**, *7* (3), 385–407.

(3) Wu, B.; Zhou, M.; Li, J.; Ye, X.; Li, G.; Cai, L. Superhydrophobic Surfaces Fabricated by Microstructuring of Stainless Steel Using a Femtosecond Laser. *Appl. Surf. Sci.* **2009**, *256* (1), 61–66.

(4) Lu, Y.; Sathasivan, S.; Song, J.; Crick, C.; Carmalt, C.; Parkin, I. Robust Self-Celaning Surfaces That Function When Exposed to Either Air or Oil. *Science* **2015**, *347* (6226), 1132–1133.

(5) Ogihara, H.; Xie, J.; Okagaki, J.; Saji, T. Simple Method for Preparing Superhydrophobic Paper: Spray-Deposited Hydrophobic Silica Nanoparticle Coatings Exhibit High Water-Repellency and Transparency. *Langmuir* **2012**, *28* (10), 4605–4608.

(6) Wong, T.-S.; Kang, S. H.; Tang, S. K. Y.; Smythe, E. J.; Hatton, B. D.; Grinthal, A.; Aizenberg, J. Bioinspired Self-Repairing Slippery Surfaces with Pressure-Stable Omniphobicity. *Nature* **2011**, *477* (7365), 443–447.

(7) Zouaghi, S.; Six, T.; Bellayer, S.; Moradi, S.; Hatzikiriakos, S. G.; Dargent, T.; Thomy, V.; Coffinier, Y.; André, C.; Delaplace, G.; Jimenez, M. Antifouling Biomimetic Liquid-Infused Stainless Steel: Application to Dairy Industrial Processing. *ACS Appl. Mater. Interfaces* **2017**, *9* (31), 26565–26573.

(8) Hwang, B. J.; Lee, S. H. Study on Micro Fabricated Stainless Steel Surface to Anti-Biofouling Using Electrochemical Fabrication. *Micro Nano Syst. Lett.* **2017**, *5* (1), 16.

(9) Wei, J.; Ravn, D. B.; Gram, L.; Kingshott, P. Stainless Steel Modified with Poly(Ethylene Glycol) Can Prevent Protein Adsorption but Not Bacterial Adhesion. *Colloids Surfaces B Biointerfaces* **2003**, *32* (4), 275–291.

(10) Zhao, Q.; Liu, Y. Modification of Stainless Steel Surfaces by Electroless Ni-P and Small Amount of PTFE to Minimize Bacterial Adhesion. *J. Food Eng.* **2006**, *72* (3), 266–272.

(11) Kannan, K.; Corsolini, S.; Falandysz, J.; Fillmann, G.; Kumar, K. S.; Loganathan, B. G.; Mohd, M. A.; Olivero, J.; Van Wouwe, N.; Yang, J. H.; Aldous, K. M. Perfluorooctanesulfonate and Related Fluorochemicals in Human Blood from Several Countries. *Environ. Sci. Technol.* **2004**, *38* (17), 4489–4495.

(12) Awad, T. S.; Asker, D.; Hatton, B. D. Food-Safe Modification of Stainless Steel Food-Processing Surfaces to Reduce Bacterial Biofilms. *ACS Appl. Mater. Interfaces* **2018**, *10* (27), 22902–22912.

(13) Damodaran, V. B.; Murthy, S. N. Bio-Inspired Strategies for Designing Antifouling Biomaterials. *Biomater. Res.* **2016**, *20* (1), 1–11.

(14) Fu, M. W.; Chan, W. L. A Review on the State-of-the-Art Microforming Technologies. *Int. J. Adv. Manuf. Technol.* **2013**, *67* (9–12), 2411–2437.

(15) Lister, K. A.; Thoms, S.; Macintyre, D. S.; Wilkinson, C. D. W.; Weaver, J. M. R.; Casey, B. G. Direct Imprint of Sub-10 Nm Features into Metal Using Diamond and SiC Stamps. *J. Vac. Sci. Technol. B Microelectron. Nanom. Struct.* **2004**, *22* (6), 3257.

(16) Taniguchi, J.; Tokano, Y.; Miyamoto, I.; Komuro, M.; Hiroshima, H. Diamond Nanoimprint Lithography. *Nanotechnology* **2002**, *13* (5), 592–596.

(17) Kim, G.-Y.; Koç, M.; Ni, J. Experimental and Numerical Investigations on Microcoining of Stainless Steel 304. *J. Manuf. Sci. Eng.* **2008**, *130* (4), 41017–410176.

(18) Diehl, A.; Engel, U.; Geiger, M. Influence of Microstructure on the Mechanical Properties and the Forming Behaviour of Very Thin Metal Foils. *Int. J. Adv. Manuf. Technol.* **2010**, *47* (1–4), 53–61.

(19) Ike, H. Surface Deformation vs. Bulk Plastic Deformation - A Key for Microscopic Control of Surfaces in Metal Forming. *J. Mater. Process. Technol.* **2003**, *138* (1–3), 250–255.

(20) Trzepieciński, T.; Pieja, T.; Malinowski, T.; Smusz, R.; Motyka, M. Investigation of 17-4PH Steel Microstructure and Conditions of Elevated Temperature Forming of Turbine Engine Strut. *J. Mater. Process. Technol.* **2018**, *252* (September 2017), 191–200.

CHAPTER 7

INNOVATION CORPS PROJECT

7.1 Project Aim

The aim of National Science Foundation (NSF) Innovation Corps (I-Corps) project was to understand market opportunity for a technology that was developed in our laboratory. Our technology (Chapter 5) enables cost-efficient production of micro/nanopatterns that can be used for functional surfaces such as antimicrobial, self-cleaning, structural color, high-performance optical coatings and so on. At the beginning, our primary aim was to find the right market for such variety of applications. To conduct market research, at least 100 potential customer interviews were targeted as a requirement of NSF I-Corps program. Those interviews were arranged to test the value propositions for each customer segments. The major focus in the customer discoveries was to learn their current needs and problems, and understand if our technology can fit for their problems. The next goal was to figure out how our technology will fit for the market.

Another aim of the project was to train the Ph.D. student (myself) as an entrepreneur and improve my entrepreneurship skills.

7.2 Major Activities and Results

We interviewed more than 100 people (at least: 74 in person, 27 phone interviews). At the beginning, we thought our technology can be interested by several different customer segments; optical product designer, antimicrobial product designer, and structural color product designer (**Figure 7.1**). The value proposition was cost efficient, higher performance and no toxicity for kids, respectively for each customer segments. Due

to restricted time of the project, we had to focus on one specific customer segment instead of being in all over the area. Thus as a team, we decided to continue with the antimicrobial product designer segment, specifically for food service industry. Bacterial contamination is a big risk in the food industry that can easily harm their prestige such as seen for Chipotle. The value proposition was to reduce the risk and fear of bacterial contamination. However, after conducting interviews we learned that even they have antimicrobial coatings, they had to continue regular cleaning/disinfectant protocols, for example, employees still had to wash their hands. All the response was nice to have antimicrobial coatings but was not truly impactful and exciting.

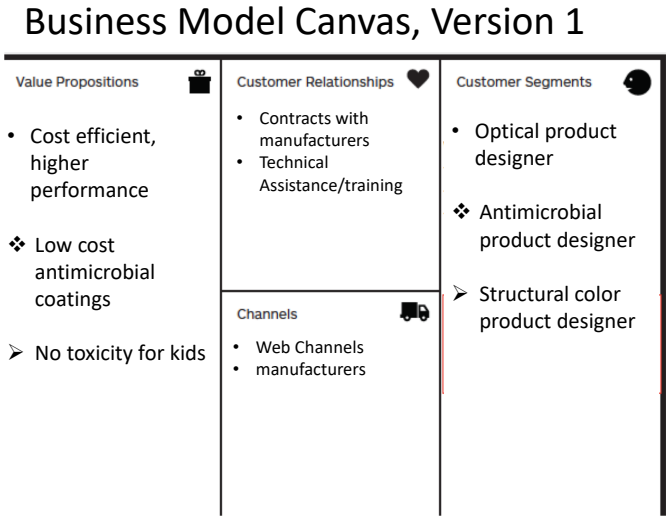

Figure 7.1: First business canvas model at the beginning of the project.

Next step was to test our hypothesis for food processors where heavily food production happens. The value proposition was to reduce the risk and fear of bacterial contamination and also reduce cleaning time and water consumption. Not only food processors but also brewers were our potential customer segment. During the interviews, we learned that amount of the cleaning time and wastewater were the major problems rather

than the risk and fear of bacterial contamination (**Figure 7.2**). For example, a microbrewer told us that he spends 14-16 hours for cleaning of a fermenter tank. An intermediate size brewer (Independent Fermentations) said that they spend 6-8 hours cleaning per tank. Moreover, we learned that Rodney Strong achieved 40% water savings and time with polished stainless steel tanks. Upon all these interviews, our customer segment was determined to be the food processors/brewers, and the value proposition was determined to be "reduced cleaning time and water consumption". One of the biggest excitement was when a quality director from a small size food processor told us they spend 130,000 gallons for cleaning per plant, which costs $13,000/per day. They cannot discharge excess amount of wastewater, and it affects their production as well. Only 10% saving of water makes them save $1.5M in 3 years (ROI: 3 years), which they were ready to pay. We also conducted interviews with tank and steel manufacturers as potential partners to figure out market fit (**Figure 7.3**).

Figure 7.2: Food processor visit. (From left to right: microbiologist, project engineer, quality director, and entrepreneur lead.

The value proposition has been significantly changed. We thought that it was "reduced the risk and fear of bacterial contamination" while we learned that it is "reduced wastewater" for food processors/brewers. Our final proposition was "Provide an antifouling, easy to clean surface in stainless steel for food processors and microbreweries providing 40-50% reduced water usage resulting in compelling ROI from significantly reduced operating costs". Therefore, as a result of interviews, we figured out our value proposition for the right market (**Figure 7.4**).

The product design had to be significantly changed according to interviews. We understood that a product that can satisfy the target customer needs should be made in steel (same material with tanks). We learned that technology/product needs to be changed according to customer needs rather than only trying to find a right customer for a specific product. A more detail study can be found in Chapter 6 which was a result of this NSF I-Corps project.

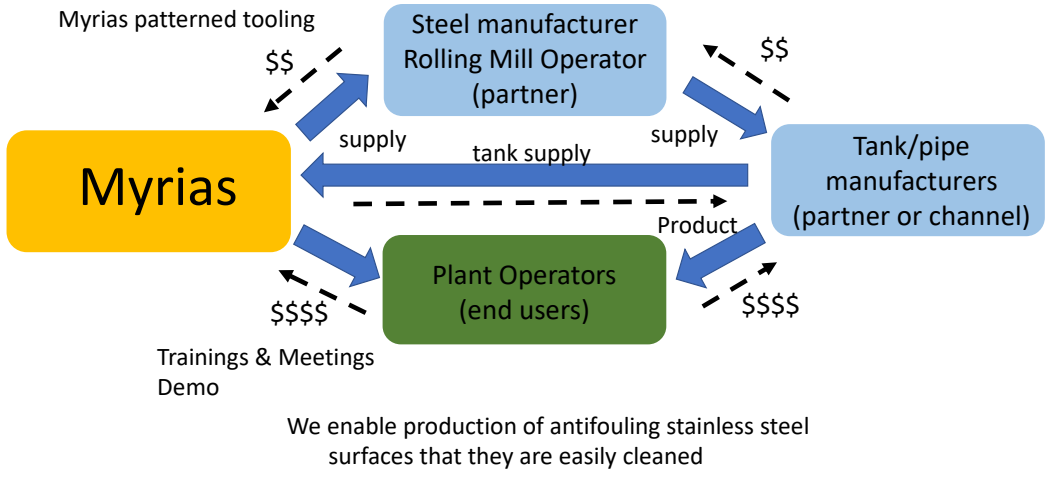

Figure 7.3: Distribution channel diagram as a result after conducting more than 100 customer interviews.

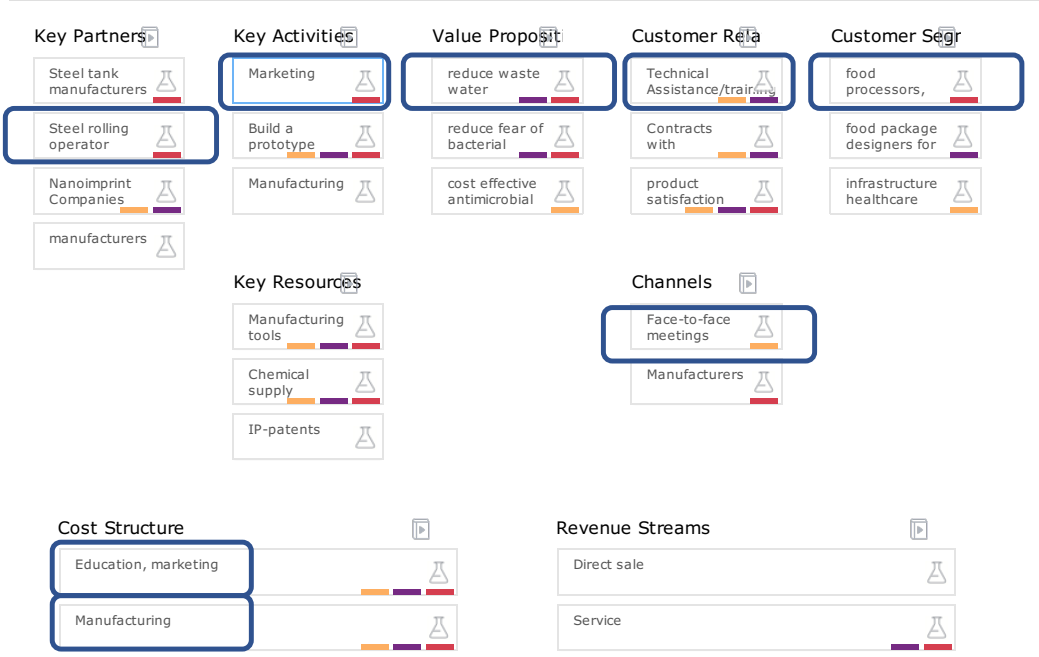

Figure 7.4: Final business canvas model at the end of the 5 weeks training program.

During the customer interviews, we found out that one of the huge interest of nanopatterned surfaces is in high-performance optical lenses. We expanded the project towards to optical area. For example, we started to work with one of the fortune 500 companies soon after the training term. In a short time, we developed a different product (high refractive index slanted structures) that is likely to be commercialized by next year. We filed several more intellectual property disclosures upon our findings/experiments as a result of the project and prepared a few manuscripts to be shared with scientific community.

CHAPTER 8

FUTURE WORK

Patterned surfaces are very useful in many applications whereas smooth surfaces cannot have performance high enough comparing to patterned surfaces as it is discussed in this dissertation. There are a number of directions for future work to conduct. For example, while the shark skin pattern has been studied as an antifouling surface in the past, this dissertation demonstrated that shark skin pattern can be effectively used in a multifunctional application by combining antifouling and sensing characteristics on a single surface. The industrial and scientific communities have been developing multifunctional devices, but there is not a simple characterization technique that can serve as an easy and fast tool to evaluate the long-term performance of multifunctional devices. Future work should focus on how to develop effective characterization methods for multifunctional devices/surfaces.

We have shown that a variety of materials can be imprinted on a variety of surfaces including a curved substrate. Further study is still needed to demonstrate the feasibility of patterned structures on complex surfaces to use these patterns on the existing tools such as current injection molding tools.

Moreover, we have demonstrated that a ZrO_2 master mold can be used to obtain nanopatterned steel surfaces (Chapter 6), but additional work needs to be done to illustrate the functionality of patterned steel surfaces. Even though most of the current studies are focused on how to make patterned steel surfaces, there is not much work done on the application of patterned steel surfaces. One of the reasons for this might be the fabrication techniques which is quite expensive. Our low-cost steel patterning technique will enable

and foster the study of variety of patterned steel or glass surfaces for different applications including self-cleaning and antifogging surfaces.

BIBLIOGRAPHY

Ahn, S. H., & Guo, L. J. (2009). Large-area roll-to-roll and roll-to-plate Nanoimprint Lithography: A step toward high-throughput application of continuous nanoimprinting. *ACS Nano*, *3*(8), 2304–2310.

Alexander, M. R., & Williams, P. (2017). Water contact angle is not a good predictor of biological responses to materials. *Biointerphases*, *12*(2), 02C201.

Anselme, K., Davidson, P., Popa, A. M., Giazzon, M., Liley, M., & Ploux, L. (2010). The interaction of cells and bacteria with surfaces structured at the nanometre scale. *Acta Biomaterialia*, *6*(10), 3824–3846.

Arisoy, F. D., Kolewe, K. W., Homyak, B., Kurtz, I. S., Schi, J. D., & Watkins, J. J. (2018). Bioinspired Photocatalytic Shark-Skin Surfaces with Antibacterial and Antifouling Activity via Nanoimprint Lithography. *ACS Applied Materials & Interfaces*, *10*(23), 20055–20063.

Awad, T. S., Asker, D., & Hatton, B. D. (2018). Food-Safe Modification of Stainless Steel Food-Processing Surfaces to Reduce Bacterial Biofilms. *ACS Applied Materials and Interfaces*, *10*(27), 22902–22912.

Ball, P. (1999). Shark skin and other solutions. *Nature: Engineering*, *400*(6744), 507–508.

Banerjee, I., Pangule, R. C., & Kane, R. S. (2011). Antifouling coatings: Recent developments in the design of surfaces that prevent fouling by proteins, bacteria, and marine organisms. *Advanced Materials*, *23*(6), 690–718.

Baxamusa, S. H., Montero, L., Dubach, J. M., Clark, H. A., Borros, S., & Gleason, K. K. (2008). Protection of sensors for biological applications by photoinitiated chemical vapor deposition of hydrogel thin films. *Biomacromolecules*, *9*(10), 2857–2862.

Beaulieu, M., Hendricks, N., & Watkins, J. (2014). Large Area Printing of Optical Gratings and 3-D Photonic Crystals using Solution Processable Nanoparticle/Polymer Composites. *ACS Photonics*, *1*(9), 799–805.

Beaulieu, M. R., Hendricks, N. R., & Watkins, J. J. (2014). Large-Area Printing of Optical Gratings and 3D Photonic Crystals Using Solution-Processable Nanoparticle/Polymer Composites. *ACS Photonics*, *1*(9), 799–805.

Bechert, D. W., Bruse, M., & Hage, W. (2000). Experiments with three-dimensional riblets as an idealized model of shark skin. *Experiments in Fluids*, *28*(5), 403–412.

Benabbou, A. K., Derriche, Z., Felix, C., Lejeune, P., & Guillard, C. (2007). Photocatalytic inactivation of Escherischia coli. Effect of concentration of TiO_2 and microorganism, nature, and intensity of UV irradiation. *Applied Catalysis B: Environmental*, *76*(3–4), 257–263.

Bhushan, B. (2009). Biomimetics: lessons from nature-an overview. *Philosophical Transactions of the Royal Society A: Mathematical, Physical and Engineering Sciences*, *367*(1893), 1445–1486.

Bixler, G. D., & Bhushan, B. (2013). Fluid drag reduction with shark-skin riblet inspired microstructured surfaces. *Advanced Functional Materials*, *23*(36), 4507–4528.

Boyce, J. M., Havill, N. L., Otter, J. A., & Adams, N. M. T. (2007). Widespread Environmental Contamination Associated With Patients With Diarrhea and Methicillin-Resistant Staphylococcus aureus Colonization of the Gastrointestinal Tract. *Infection Control & Hospital Epidemiology*, *28*(10), 1142–1147.

Carling, P. C., Briggs, J., Hylander, D., & Perkins, J. (2006). An evaluation of patient area cleaning in 3 hospitals using a novel targeting methodology. *American Journal of Infection Control*, *34*(8), 513–519.

Carman, M. L., Estes, T. G., Feinberg, A. W., Schumacher, J. F., Wilkerson, W., Wilson, L. H., … Brennan, A. B. (2006). Engineered antifouling microtopographies--correlating wettability with cell attachment. *Biofouling*, *22*(1–2), 11–21.

Carp, O., Huisman, C. L., & Reller, A. (2004). Photoinduced reactivity of titanium dioxide. *Progress in Solid State Chemistry*, *32*(1–2), 33–177.

Castner, D. G., & Ratner, B. D. (2002). *Biomedical surface science: Foundations to frontiers*. *Surface Science*, 500(1-3), 28–60.

CDC. (2013). *Antibiotic resistance threats in the United States, 2013*. *Current*. Retrieved from http://www.cdc.gov/drugresistance/threat-report-2013/index.html

Chen, X., Sun, J., & Shen, J. (2009). Patterning of layer-by-layer assembled organic-inorganic hybrid films: Imprinting versus lift-off. *Langmuir*, *25*(5), 3316–3320.

Chou, S. Y., Krauss, P. R., & Renstrom, P. J. (1995). Imprint of sub-25 nm vias and trenches in polymers. *Applied Physics Letters*, *67*(1995), 3114.

Chung, K. K., Schumacher, J. F., Sampson, E. M., Burne, R. a, Antonelli, P. J., & Brennan, A. B. (2007a). Impact of engineered surface microtopography on biofilm formation of Staphylococcus aureus. *Biointerphases*, *2*(2), 89–94.

Costerton, J. W., Stewart, P. S., & Greenberg, E. P. (1999). Bacterial Biofilms: A Common Cause of Persistent Infections. *Science* , *284*(5418), 1318–1322.

Damodaran, V. B., & Murthy, S. N. (2016). Bio-inspired strategies for designing antifouling biomaterials. *Biomaterials Research*, *20*(1), 1–11.

Dang, H., & Lovell, C. R. (2016). Microbial Surface Colonization and Biofilm Development in Marine Environments, *80*(1), 91–138.

Desai, N. P., & Hubbell, J. A. (1991). Solution technique to incorporate polyethylene oxide and other water-soluble polymers into surfaces of polymeric biomaterials. *Biomaterials*, *12*(2), 144–153.

Diehl, A., Engel, U., & Geiger, M. (2010). Influence of microstructure on the mechanical properties and the forming behaviour of very thin metal foils. *International Journal of Advanced Manufacturing Technology*, *47*(1–4), 53–61.

Díez-Pascual, A. M., & Díez-Vicente, A. L. (2015). Nano-TiO2 reinforced PEEK/PEI blends as biomaterials for load-bearing implant applications. *ACS Applied Materials and Interfaces*, *7*(9), 5561–5573.

Dobosz, K. M., Kolewe, K. W., & Schiffman, J. D. (2015). Green materials science and engineering reduces biofouling: Approaches for medical and membrane-based technologies. *Frontiers in Microbiology*, *6*(MAR), 1–8.

Doll, K., Fadeeva, E., Stumpp, N. S., Grade, S., Chichkov, B. N., & Stiesch, M. (2016). Reduced bacterial adhesion on titanium surfaces micro-structured by ultra-short pulsed laser ablation. *BioNanoMaterials*, *17*(1–2), 53–57.

Dou, X. Q., Zhang, D., Feng, C., & Jiang, L. (2015). Bioinspired Hierarchical Surface Structures with Tunable Wettability for Regulating Bacteria Adhesion. *ACS Nano*, *9*(11), 10664–10672.

Drelich, J., & Chibowski, E. (2010). Superhydrophilic and superwetting surfaces: Definition and mechanisms of control. *Langmuir*, *26*(24), 18621–18623.

Drelich, J., Chibowski, E., Meng, D. D., & Terpilowski, K. (2011). Hydrophilic and superhydrophilic surfaces and materials. *Soft Matter*, *7*(21), 9804.

Foster, H. a., Ditta, I. B., Varghese, S., & Steele, A. (2011). Photocatalytic disinfection using titanium dioxide: Spectrum and mechanism of antimicrobial activity. *Applied Microbiology and Biotechnology*, *90*(6), 1847–1868.

French, G. L., Otter, J. A., Shannon, K. P., Adams, N. M. T., Watling, D., & Parks, M. J. (2018). Tackling contamination of the hospital environment by methicillin-resistant Staphylococcus aureus (MRSA): a comparison between conventional terminal cleaning and hydrogen peroxide vapour decontamination. *Journal of Hospital Infection*, *57*(1), 31–37.

Fu, G., Vary, P. S., & Lin, C.-T. (2005). Anatase TiO2 nanocomposites for antimicrobial coatings. *The Journal of Physical Chemistry B*, *109*(18), 8889–8898.

Fu, M. W., & Chan, W. L. (2013). A review on the state-of-the-art microforming technologies. *International Journal of Advanced Manufacturing Technology*, *67*(9–12), 2411–2437.

Fujishima, A., & Honda, K. (1972). Electrochemical photolysis of water at a semiconductor electrode. *Nature*, *238*(5358), 37–38.

Fujishima, A., Rao, T. N., & Tryk, D. A. (2000). Titanium dioxide photocatalysis. *Journal of Photochemistry and Photobiology C: Photochemistry Reviews*, *1*(1), 1–21.

Fujishima, A., Zhang, X., & Tryk, D. A. (2008). TiO_2 photocatalysis and related surface phenomena. *Surface Science Reports*, *63*(12), 515–582.

Ganesan, R., Dumond, J., Saifullah, M. S. M., Lim, S. H., Hussain, H., & Low, H. Y. (2012). Direct Patterning of TiO2 Using Step-and-Flash Imprint Lithography. *ACS Nano*, *6*(2), 1494–1502.

Gao, L., & McCarthy, T. J. (2006). Contact angle hysteresis explained. *Langmuir : The ACS Journal of Surfaces and Colloids*, *22*(14), 6234–6237.

Gates, B. D., Xu, Q., Stewart, M., Ryan, D., Willson, C. G., & Whitesides, G. M. (2005). New approaches to nanofabrication: Molding, printing, and other techniques. *Chemical Reviews*, *105*(4), 1171–1196.

Genevet, P., Capasso, F., Aieta, F., Khorasaninejad, M., & Devlin, R. (2017). Recent advances in planar optics: from plasmonic to dielectric metasurfaces. *Optica*, *4*(1), 139.

Genzer, J., & Efimenko, K. (2006). Recent developments in superhydrophobic surfaces and their relevance to marine fouling: a review. *Biofouling*, *22*(5–6), 339–360.

Gorbet, M. B., & Sefton, M. V. (2006). Biomaterial-associated thrombosis: Roles of coagulation factors, complement, platelets and leukocytes. *The Biomaterials: Silver Jubilee Compendium*, *25*, 219–241.

Graham, M., & Cady, N. (2014). Nano and Microscale Topographies for the Prevention of Bacterial Surface Fouling. *Coatings*, *4*(1), 37–59.

Gu, Y., Zhang, L., Yang, J. K. W., Yeo, S. P., & Qiu, C. W. (2015). Color generation via subwavelength plasmonic nanostructures. *Nanoscale*, *7*(15), 6409–6419.

Guo, L. J. (2004). Recent progress in nanoimprint technology and its applications. *Journal of Physics D: Applied Physics*, *37*(11).

Guo, L. J. (2007). Nanoimprint lithography: Methods and material requirements. *Advanced Materials*, *19*(4), 495–513.

Hampton, M. J., Williams, S. S., Zhou, Z., Nunes, J., Ko, D. H., Templeton, J. L., Samulski, E. T., DeSimone, J. M. (2008). The patterning of sub-500 nm inorganic oxide structures. *Advanced Materials*, *20*(14), 2667–2673.

Hanaor, D. A. H., & Sorrell, C. C. (2011). Review of the anatase to rutile phase transformation. *Journal of Materials Science*, *46*(4), 855–874.

Hartleb, W., Saar, J. S., Zou, P., & Lienkamp, K. (2016). Just Antimicrobial is not Enough: Toward Bifunctional Polymer Surfaces with Dual Antimicrobial and Protein-Repellent Functionality. *Macromolecular Chemistry and Physics*, *217*(2), 225–231.

Hasan, J., & Chatterjee, K. (2015). Recent advances in engineering topography mediated antibacterial surfaces. *Nanoscale*, *7*(38), 15568–15575.

Hasan, J., Crawford, R. J., & Ivanova, E. P. (2013). Antibacterial surfaces: The quest for a new generation of biomaterials. *Trends in Biotechnology*, *31*(5), 295–304.

Hashimoto, K., Irie, H., & Fujishima, A. (2007). A Historical Overview and Future Prospects. *AAPPS Bulletin*, *17*(6), 12–28.

Hobæk, T. C., Matschuk, M., Kafka, J., Pranov, H. J., & Larsen, N. B. (2015). Hydrogen silsesquioxane mold coatings for improved replication of nanopatterns by injection molding. *Journal of Micromechanics and Microengineering*, *25*(3), 035018.

Højlund-Nielsen, E., Clausen, J., Mäkela, T., Thamdrup, L. H., Zalkovskij, M., Nielsen, T., Kristensen, A. (2016). Plasmonic Colors: Toward Mass Production of Metasurfaces. *Advanced Materials Technologies*, *1*(7), 1–8.

Hooper, K., Carnie, M., Charbonneau, C., & Watson, T. (2014). Near Infrared Radiation as a Rapid Heating Technique for TiO $_2$ Films on Glass Mounted Dye-Sensitized Solar Cells. *International Journal of Photoenergy*, *2014*(1), 1–8.

Howell, I. R., Giroire, B., Garcia, A., Li, S., Aymonier, C., & Watkins, J. J. (2018). Fabrication of plasmonic TiN nanostructures by nitridation of nanoimprinted TiO2 nanoparticles. *Journal of Materials Chemistry C*, *6*(6), 1399–1406.

Hurum, D. C., Agrios, A. G., Gray, K. A., Rajh, T., & Thurnauer, M. C. (2003). Explaining the Enhanced Photocatalytic Activity of Degussa P25 Mixed-Phase TiO2 Using EPR. *The Journal of Physical Chemistry B*, *107*(19), 4545–4549.

Hwang, B. J., & Lee, S. H. (2017). Study on micro fabricated stainless steel surface to anti-biofouling using electrochemical fabrication. *Micro and Nano Systems Letters*, *5*(1), 16.

Ike, H. (2003). Surface deformation vs. bulk plastic deformation - A key for microscopic control of surfaces in metal forming. *Journal of Materials Processing Technology*, *138*(1–3), 250–255.

Jeevanandam, P., Mulukutla, R. S., Phillips, M., Chaudhuri, S., Erickson, L. E., & Klabunde, K. J. (2007). Near infrared reflectance properties of metal oxide nanoparticles. *Journal of Physical Chemistry C*, *111*(5), 1912–1918.

Jiao, X., Song, H., Zhao, H., Bai, W., Zhang, L., & Lv, Y. (2012). Well-redispersed ceria nanoparticles: Promising peroxidase mimetics for H 2O 2 and glucose detection. *Analytical Methods*, *4*(10), 3261–3267.

Kuhn, K. P., Chaberny, I. F., Massholder, K., Stickler, M., Benz, V. W., Sonntag, H. G., & Erdinger, L. (2003). Disinfection of surfaces by photocatalytic oxidation with titanium dioxide and UVA light. *Chemosphere*, *53*(1), 71–77.

Kane, R. S., Takayama, S., Ostuni, E., Ingber, D. E., & Whitesides, G. M. (1999). Patterning proteins and cells using soft lithography. *Biomaterials*, *20*(23), 2363–2376.

Kannan, K., Corsolini, S., Falandysz, J., Fillmann, G., Kumar, K. S., Loganathan, B. G., Mohd, M. A., Olivero, J., Wouwe, N. V., Aldous, K. M. (2004). Perfluorooctanesulfonate and related fluorochemicals in human blood from several countries. *Environmental Science and Technology*, *38*(17), 4489–4495.

Karakoti, A. S., Kuchibhatla, S. V. N. T., Babu, K. S., & Seal, S. (2007). Direct synthesis of nanoceria in aqueous polyhydroxyl solutions. *Journal of Physical Chemistry C*, *111*(46), 17232–17240.

Kim, B. J., & Meng, E. (2016). Micromachining of Parylene C for bioMEMS. *Polymers for Advanced Technologies*, *27*(5), 564–576.

Kim, G.-Y., Koç, M., & Ni, J. (2008). Experimental and Numerical Investigations on Microcoining of Stainless Steel 304. *Journal of Manufacturing Science and Engineering*, *130*(4), 41017–410176.

Kolewe, K. W., Peyton, S. R., & Schiffman, J. D. (2015). Fewer Bacteria Adhere to Softer Hydrogels. *ACS Applied Materials and Interfaces*, *7*(35), 19562–19569.

Korsvik, C., Patil, S., Seal, S., & Self, W. T. (2007). Superoxide dismutase mimetic properties exhibited by vacancy engineered ceria nanoparticles. *Chemical Communications*, (10), 1056–1058.

Kothari, R., Beaulieu, M. R., Hendricks, N. R., Li, S., & Watkins, J. J. (2017). Direct Patterning of Robust 1-D, 2-D and 3-D Crystalline Metal Oxide Nanostructures using Imprint Lithography and Nanoparticle Dispersion Inks. *Chemistry of Materials*, *29*, 3908−3918.

Krishnan, S., Wang, N., Ober, C. K., Finlay, J. A., Callow, M. E., Callow, J. A., … Fischer, D. A. (2006). Comparison of the fouling release properties of hydrophobic fluorinated and hydrophilic PEGylated block copolymer surfaces: Attachment strength of the diatom Navicula and the green alga Ulva. *Biomacromolecules*, *7*(5), 1449–1462.

Krishnan, S., Weinman, C. J., & Ober, C. K. (2008). Advances in polymers for anti-biofouling surfaces. *J. Mater. Chem.*, *18*(29), 3405–3413.

Kubacka, A., Diez, M. S., Rojo, D., Bargiela, R., Ciordia, S., Zapico, I., Albar, J. P., Barbas, C., Santos, A. A. P., Fernandez-Garcia, M., Ferrer, M. (2014). Understanding the antimicrobial mechanism of TiO_2-based nanocomposite films in a pathogenic bacterium. *Sci. Rep.*, *4*.

Kubacka, A., Serrano, C., Ferrer, M., Lnsdorf, H., Bielecki, P., Cerrada, M. L., Fernandez-Garcia, M., Fernandez-Gracia, M. (2007). High-Performance Dual-Action Polymer −TiO_2 Nanocomposite Films via Melting Processing. *Nano Lett.*, 7(8), 2529–2534.

Kumar, G., Tang, H. X., & Schroers, J. (2009). Nanomoulding with amorphous metals. *Nature*, *457*(7231), 868–872.

Kwon, B., & Kim, J. H. (2016). Importance of Molds for Nanoimprint Lithography : Hard , Soft , and Hybrid Molds, *Journal of Nanoscience, 2016.*

Leyland, N. S., Podporska-Carroll, J., Browne, J., Hinder, S. J., Quilty, B., & Pillai, S. C. (2016). Highly Efficient F, Cu doped TiO2 anti-bacterial visible light active photocatalytic coatings to combat hospital-acquired infections. *Scientific Reports*, *6*(April), 24770.

Li, C., Colella, N. S., & Watkins, J. J. (2015). Low-Temperature Fabrication of Mesoporous Titanium Dioxide Thin Films with Tunable Refractive Indices for One-Dimensional Photonic Crystals and Sensors on Rigid and Flexible Substrates. *ACS Applied Materials and Interfaces*, *7*(24), 13180–13188.

Li, L., Chen, S., Zheng, J., Ratner, B. D., & Jiang, S. (2005). Protein adsorption on oligo(ethylene glycol)-terminated alkanethiolate self-assembled monolayers: The molecular basis for nonfouling behavior. *Journal of Physical Chemistry B*, *109*(7), 2934–2941.

Li, M., Tan, H., Chen, L., Wang, J., & Chou, S. Y. (2003). Large area direct nanoimprinting of SiO_2–TiO_2 gel gratings for optical applications. *Journal of Vacuum Science & Technology B: Microelectronics and Nanometer Structures*, *21*(2), 660–663.

Li, S., Kazemi-moridani, A., Zhou, Y., Howell, I. R., Kothari, R., Lee, J., & Watkins, J. J. (2018). Wavelength-Selective Three-Dimensional Thermal Emitters via Imprint Lithography and Conformal Metallization.

Li, W., Christiansen, T. L., Li, C., Zhou, Y., Fei, H., Mamakhel, A., Iversen, B. B., Watkins, J. J. (2018). High-power lithium-ion microbatteries from imprinted 3D electrodes of sub-10 nm $LiMn_2O_4$/$Li_4Ti_5O_{12}$ nanocrystals and a copolymer gel electrolyte. *Nano Energy*, *52*, 431–440.

Li, W., Zhou, Y., Howell, I. R., Gai, Y., Naik, A. R., Li, S., Carter, K. R., Watkins, J. J. (2018). Direct Imprinting of Scalable , High-Performance Woodpile Electrodes for Three-Dimensional Lithium-Ion Nanobatteries. *ACS Appl. Mater. Interfaces*, *10*(6), 5447–5454.

Li, Y., Zhang, W., Niu, J., & Chen, Y. (2012). Mechanism of photogenerated reactive oxygen species and correlation with the antibacterial properties of engineered metal-oxide nanoparticles. *ACS Nano*, *6*(6), 5164–5173.

Lichter, J. A., Thompson, M. T., Delgadillo, M., Nishikawa, T., Rubner, M. F., & Van Vliet, K. J. (2008). Substrata mechanical stiffness can regulate adhesion of viable bacteria. *Biomacromolecules*, *9*(6), 1571–1578.

Lister, K. A., Thoms, S., Macintyre, D. S., Wilkinson, C. D. W., Weaver, J. M. R., & Casey, B. G. (2004). Direct imprint of sub-10 nm features into metal using diamond and SiC stamps. *Journal of Vacuum Science & Technology B: Microelectronics and Nanometer Structures*, *22*(6), 3257.

Liu, K., & Jiang, L. (2012a). Bio-Inspired Self-Cleaning Surfaces. *Annual Review of Materials Research*, *42*(1), 231–263.

Long, C. J., Schumacher, J. F., & Brennan, A. B. (2009). Potential for Tunable Static and Dynamic Contact Angle Anisotropy on Gradient Microscale Patterned Topographies, *25*(9), 12982–12989.

Lu, Y., Sathasivan, S., Song, J., Crick, C., Carmalt, C., & Parkin, I. (2015). Robust self-celaning surfaces that fucntion when exposed to either air or oil. *Science (New York, N.Y.)*, *347*(6226), 1132–1133.

Lu, Y., Yue, Z., Wang, W., & Cao, Z. (2015). Strategies on designing multifunctional surfaces to prevent biofilm formation. *Frontiers of Chemical Science and Engineering*, *9*(3), 324–335.

Ma, P., Xu, Z., Wang, M., Lu, L., Yin, M., Chen, X., … Ren, W. (2017). Fast fabrication of TiO2hard stamps for nanoimprint lithography. *Materials Research Bulletin*, *90*, 253–259.

Matsunaga, T., Tomoda, R., Nakajima, T., & Wake, H. (1985). Photoelectrochemical sterilization of microbial cells by semiconductor powders. *FEMS Microbiology Letters*, *29*(1–2), 211–214.

May, R. M., Hoffman, M. G., Sogo, M. J., Parker, A. E., O'Toole, G. a, Brennan, A. B., & Reddy, S. T. (2014). Micro-patterned surfaces reduce bacterial colonization and biofilm formation in vitro: Potential for enhancing endotracheal tube designs. *Clinical and Translational Medicine*, *3*(1), 8.

May, R. M., Magin, C. M., Mann, E. E., Drinker, M. C., Fraser, J. C., Siedlecki, C. A., Brennan, A. B., Reddy, S. T. (2015). An engineered micropattern to reduce bacterial colonization, platelet adhesion and fibrin sheath formation for improved biocompatibility of central venous catheters. *Clinical and Translational Medicine*, *4*(1), 9.

Mehner, A., Zoch, H.-W., Datchary, W., Pongs, G., & Kunzmann, H. (2006). Sol-Gel Coatings for High Precision Optical Molds. *CIRP Annals - Manufacturing Technology*, *55*(1), 589–592.

Mehta, A., Patil, S., Bang, H., Cho, H. J., & Seal, S. (2007). A novel multivalent nanomaterial based hydrogen peroxide sensor. *Sensors and Actuators, A: Physical*, *134*(1), 146–151.

Montero, L., Gabriel, G., Guimerà, A., Villa, R., Gleason, K. K., & Borrós, S. (2012). Increasing biosensor response through hydrogel thin film deposition: Influence of hydrogel thickness. *Vacuum*, *86*(12), 2102–2104.

Moran, I. W., Briseno, A. L., Loser, S., & Carter, K. R. (2008). Device Fabrication by Easy Soft Imprint Nano-Lithography. *Chem. Mater.*, *20*(14), 4595–4601.

Neal, C. J., Gupta, A., Barkam, S., Saraf, S., Das, S., & Hyoung, J. (2017). Picomolar Detection of Hydrogen Peroxide using Enzyme-free Inorganic Nanoparticle-based Sensor. *Scientific Reports*, 1–10.

Nie, Z., & Kumacheva, E. (2008). Patterning surfaces with functional polymers. *Nature Materials*, *7*(4), 277–290.

Ogihara, H., Xie, J., Okagaki, J., & Saji, T. (2012). Simple method for preparing superhydrophobic paper: Spray-deposited hydrophobic silica nanoparticle coatings exhibit high water-repellency and transparency. *Langmuir*, *28*(10), 4605–4608.

Oliver, C., & Pharr, M. (1992). An improved technique for determining hardness and elastic modulus using load and displacement sensing indentation experiments. *Journal of Materials Research*.

Oliver, W. C., & Pharr, G. M. (2004). Measurement of hardness and elastic modulus by instrumented indentation: Advances in understanding and refinements to methodology. *Journal of Materials Research*, *19*(01), 3–20.

Onaizi, S. A., & Leong, S. S. J. (2011). Tethering antimicrobial peptides: Current status and potential challenges. *Biotechnology Advances*, *29*(1), 67–74.

Ostuni, E., Chapman, R. G., Holmlin, R. E., Takayama, S., & Whitesides, G. M. (2001). A Survey of Structure - Property Relationships of Surfaces that Resist the Adsorption of Protein, *17*(9), 5605–5620.

Ostuni, E., Chapman, R. G., Liang, M. N., Meluleni, G., Pier, G., Ingber, D. E., & Whitesides, G. M. (2001). Self-assembled monolayers that resist the adsorption of proteins and the adhesion of bacterial and mammalian cells. *Langmuir*, *17*(20), 6336–6343.

Ozkan, E., Crick, C. C., Taylor, A., Allan, E., & Parkin, I. P. (2016). Copper-based water repellent and antibacterial coatings by aerosol assisted chemical vapour deposition. *Chem. Sci.*, *7*(8), 5126–5131.

Page, K., Wilson, M., Parkin, I. P. (2009). Antimicrobial surfaces and their potential in reducing the role of the inanimate environment in the incidence of hospital-acquired infections. *J. Mater. Chem., 19*, 3819–3831.

Parashar, U. K., Kumar, V., Bera, T., Saxena, P. S., Nath, G., Srivastava, S. K., Giri, R., Srivastava, A. (2011). Study of mechanism of enhanced antibacterial activity by green synthesis of silver nanoparticles. *Nanotechnology*, *22*(41).

Park, H. H., Zhang, X., Lee, S. W., Kim, K. D., Choi, D. G., Choi, J. H., Lee, J., Lee, E., Park, H., Hill, R. H., Jeong, J. H. (2011). Facile nanopatterning of zirconium dioxide films via direct ultraviolet-assisted nanoimprint lithography. *Journal of Materials Chemistry*, *21*(3), 657–662.

Patil, S., Sandberg, A., Heckert, E., Self, W., & Seal, S. (2007). Protein adsorption and cellular uptake of cerium oxide nanoparticles as a function of zeta potential. *Biomaterials*, *28*(31), 4600–4607.

Perni, S., & Prokopovich, P. (2013). Micropatterning with conical features can control bacterial adhesion on silicone. *Soft Matter*, *9*(6), 1844–1851.

Piner, R. D., Zhu, J., Xu, F., Hong, S., & Mirkin, C. A. (1999). "Dip-pen" nanolithography. *Science*, *283*(5402), 661–663.

Pogorzelska-Maziarz, M., Carter, E. J., Manning, M. L., & Larson, E. L. (2016). State Health Department Requirements for Reporting of Antibiotic-Resistant Infections by Providers, United States, 2013 and 2015. *Public Health Reports*, *132*(1), 32–36.

Prosser, J. H., Brugarolas, T., Lee, S., Nolte, A. J., & Lee, D. (2012). Avoiding cracks in nanoparticle films. *Nano Letters*, *12*(10), 5287–5291.

Reddy, M. C. C. G. S., & Nadagouda, M. N. (2017). Antimicrobial and anticorrosive efficacy of inorganic nanoporous surfaces. *Clean Technologies and Environmental Policy*, *19*(3), 845–857. http://doi.org/10.1007/s10098-016-1272-2

Reddy, S. T., Chung, K. K., McDaniel, C. J., Darouiche, R. O., Landman, J., & Brennan, A. B. (2011). Micropatterned Surfaces for Reducing the Risk of Catheter-Associated Urinary Tract Infection: An *In Vitro* Study on the Effect of Sharklet Micropatterned Surfaces to Inhibit Bacterial Colonization and Migration of Uropathogenic Escherichia coli. *Journal of Endourology*, *25*(9), 1547–1552.

Reed, K., Cormack, A., Kulkarni, A., Mayton, M., Sayle, D., Klaessig, F., & Stadler, B. (2014). Exploring the properties and applications of nanoceria: Is there still plenty of room at the bottom? *Environmental Science: Nano*, *1*(5), 390–405.

Rieger, K. A., Cho, H. J., Yeung, H. F., Fan, W., & Schi, J. D. (2016). Antimicrobial Activity of Silver Ions Released from Zeolites Immobilized on Cellulose Nano fi ber Mats. *ACS Appl. Mater. Interfaces, 8* (5), 3032–3040.

Rodriguez-Emmenegger, C., Brynda, E., Riedel, T., Houska, M., Šubr, V., Alles, A. B., Hasan, E., Gautrot, J. E., Huck, W. T. S. (2011). Polymer brushes showing non-fouling in blood plasma challenge the currently accepted design of protein resistant surfaces. *Macromolecular Rapid Communications*, *32*(13), 952–957.

Sae-Ung, P., Kolewe, K. W., Bai, Y., Rice, E. W., Schiffman, J. D., Emrick, T., & Hoven, V. P. (2017). Antifouling Stripes Prepared from Clickable Zwitterionic Copolymers. *Langmuir*, *33*(28), 7028–7035.

Saleem, M. R. (2012). Hydrogen silsesquioxane resist stamp for replication of nanophotonic components in polymers. *Journal of Micro/Nanolithography, MEMS, and MOEMS*, *11*(1), 013007.

Sanpo, N., Ang, S. M., Cheang, P., & Khor, K. a. (2009). Antibacterial property of cold sprayed chitosan-cu/al coating. *Journal of Thermal Spray Technology*, *18*, 600–608.

Scardino, A. J., & de Nys, R. (2011). Mini review: Biomimetic models and bioinspired surfaces for fouling control. *Biofouling*, *27*(1), 73–86.

Schift, H. (2008). Nanoimprint lithography: An old story in modern times? A review. *Journal of Vacuum Science & Technology B: Microelectronics and Nanometer Structures*, *26*(2), 458.

Schift, H., Urwyler, P., Kristiansen, P. M., & Gobrecht, J. (2014). Nanoimprint lithography process chains for the fabrication of micro- and nanodevices. *Journal of Micro/Nanolithography, MEMS, and MOEMS*, *13*(3), 031303.

Schumacher, J. F., Aldred, N., Callow, M. E., Finlay, J. a, Callow, J. a, Clare, A. S., & Brennan, A. B. (2007). Species-specific engineered antifouling topographies: correlations between the settlement of algal zoospores and barnacle cyprids. *Biofouling*, *23*(5–6), 307–17.

Schumacher, J. F., Carman, M. L., Estes, T. G., Feinberg, A. W., Wilson, L. H., Callow, M. E., Brennan, A. B. (2007). Engineered antifouling microtopographies - effect of feature size, geometry, and roughness on settlement of zoospores of the green alga Ulva. *Biofouling*, *23*(1–2), 55–62.

Schumacher, J. F., Long, C. J., Callow, M. E., Finlay, J. a., Callow, J. a., & Brennan, A. B. (2008). Engineered nanoforce gradients for inhibition of settlement (attachment) of swimming algal spores. *Langmuir*, *24*(9), 4931–4937.

Sena, L. A., Chandel, N. S. (2012). Physiological roles of mitochondrial reactive oxygen species. *Molecular Cell*, *48*(2), 158–166.

Simeone, A., Woolley, E., Rodriguez, A. Z., & Rahimifard, S. (2017). Eco-intelligent Monitoring for Fouling Detection in Clean-in-place. *Procedia CIRP*, *62*(4), 500–505.

Song, F., Koo, H., & Ren, D. (2015a). Effects of Material Properties on Bacterial Adhesion and Biofilm Formation. *J Dent Res*, *94*(8), 1027–1034.

Song, F., Koo, H., & Ren, D. (2015b). Effects of Material Properties on Bacterial Adhesion and Biofilm Formation. *J Dent Res*, *94*(8), 1027–1034.

Stewart, P. S., Costerton, J. W. (2001). Antibiotic resistance of bacteria in biofilms. *Lancet*, *358*(9276), 135–138.

Stormonth-Darling, J. M., Gadegaard, N. (2012). Injection moulding difficult nanopatterns with hybrid polymer inlays. *Macromolecular Materials and Engineering*, *297*(11), 1075–1080.

Su, B., Tian, Y., Jiang, L. (2016). Bioinspired Interfaces with Superwettability: From Materials to Chemistry. *Journal of the American Chemical Society*, 138(6), 1727–1748.

Tanaka, M., Mochizuki, A., Ishii, N., Motomura, T., & Hatakeyama, T. (2002). Study of blood compatibility with poly(2-methoxyethyl acrylate). Relationship between water structure and platelet compatibility in poly(2-methoxyethylacrylate-co-2-hydroxyethylmethacrylate). *Biomacromolecules*, *3*(1), 36–41.

Taniguchi, J., Tokano, Y., Miyamoto, I., Komuro, M., Hiroshima, H. (2002). Diamond nanoimprint lithography. *Nanotechnology*, *13*(5), 592–596.

Thallinger, B., Prasetyo, E. N., Nyanhongo, G. S., Guebitz, G. M. (2013). Antimicrobial enzymes: An emerging strategy to fight microbes and microbial biofilms. *Biotechnology Journal*, *8*(1), 97–109.

Tosello, G., Hansen, H. N., Gasparin, S., Albajez, J. A., & Esmoris, J. I. (2012). Surface wear of TiN coated nickel tool during the injection moulding of polymer micro Fresnel lenses. *CIRP Annals - Manufacturing Technology*, *61*(1), 535–538.

Trzepieciński, T., Pieja, T., Malinowski, T., Smusz, R., & Motyka, M. (2018). Investigation of 17-4PH steel microstructure and conditions of elevated temperature forming of turbine engine strut. *Journal of Materials Processing Technology*, *252*, 191–200.

Ucar, I. O., Cansoy, C. E., Erbil, H. Y., Pettitt, M. E., Callow, M. E., Callow, J. A. (2010). Effect of contact angle hysteresis on the removal of the sporelings of the green alga *Ulva* from the fouling-release coatings synthesized from polyolefin polymers. *Biointerphases*, *5*(3), 75–84.

Ujjain, S. K., Das, A., Srivastava, G., Ahuja, P., Roy, M., Arya, A., Singh, S. K., Sharma, R. K., Das, M. (2014). Nanoceria based electrochemical sensor for hydrogen peroxide detection. *Biointerphases*, *9*(3), 031011.

Assenbergh, P.V., Meinders, E., Geraedts, J., & Dodou, D. (2018). Nanostructure and Microstructure Fabrication: From Desired Properties to Suitable Processes. *Small*, 14 (20), 1703401.

Vorobyev, A. Y., & Guo, C. (2013). Direct femtosecond laser surface nano/microstructuring and its applications. *Laser and Photonics Reviews*, *7*(3), 385–407.

Watson, T., Mabbett, I., Hongxia, W., & Worsley, D. (2010). Ultrafast near infrared sintering of TiO_2 layers on metal substrates for dye-sensitized solar cells. *Prog. Photovolt: Res. Appl.*, *19*, 482–486.

Weber, D. J., Rutala, W. A., Miller, M. B., Huslage, K., & Sickbert-Bennett, E. (2010). Role of hospital surfaces in the transmission of emerging health care-associated pathogens: Norovirus, Clostridium difficile, and Acinetobacter species. *American Journal of Infection Control*, *38*(5 SUPPL.), S25–S33.

Wei, J., Ravn, D. B., Gram, L., & Kingshott, P. (2003). Stainless steel modified with poly(ethylene glycol) can prevent protein adsorption but not bacterial adhesion. *Colloids and Surfaces B: Biointerfaces*, *32*(4), 275–291.

Whitehead, K. A., Colligon, J., & Verran, J. (2005). Retention of microbial cells in substratum surface features of micrometer and sub-micrometer dimensions. *Colloids and Surfaces B: Biointerfaces*, *41*(2–3), 129–138.

Wisniewski, N., & Reichert, M. (2000). Methods for reducing biosensor membrane biofouling. *Colloids and Surfaces B: Biointerfaces*, *18*(3–4), 197–219.

Wong, T.-S., Kang, S. H., Tang, S. K. Y., Smythe, E. J., Hatton, B. D., Grinthal, A., & Aizenberg, J. (2011). Bioinspired self-repairing slippery surfaces with pressure-stable omniphobicity. *Nature*, *477*(7365), 443–447.

Wu, B., Zhou, M., Li, J., Ye, X., Li, G., & Cai, L. (2009). Superhydrophobic surfaces fabricated by microstructuring of stainless steel using a femtosecond laser. *Applied Surface Science*, *256*(1), 61–66.

Xia, Y. N., & Whitesides, G. M. (1998). Soft lithography. *Annual Review Of Materials Science*, *37*(5), 551–575.

Yague, J. L., & Gleason, K. K. (2012). Systematic control of mesh size in hydrogels by initiated chemical vapor deposition. *Soft Matter*, *8*(10), 2890–2894.

Youngblood, J. P., & McCarthy, T. J. (1999). Ultrahydrophobic polymer surfaces prepared by simultaneous ablation of polypropylene and sputtering of poly(tetrafluoroethylene) using radio frequency plasma. *American Chemical Society, Polymer Preprints, Division of Polymer Chemistry*, *40*(2), 563–564.

Yu, Q., Wu, Z., & Chen, H. (2015). Dual-function antibacterial surfaces for biomedical applications. *Acta Biomaterialia*, *16*(1), 1–13.

Yu, Z. J., Kang, E. T., & Neoh, K. G. (2002). Electroless plating of copper on polyimide films modified by surface grafting of tertiary and quaternary amines polymers. *Polymer*, *43*(15), 4137–4146.

Zhang, N., Byrne, C. J., Browne, D. J., & Gilchrist, M. D. (2012). Towards nano-injection molding. *Materials Today*, *15*(5), 216–221.

Zhang, N., Chu, J. S., Byrne, C. J., Browne, D. J., & Gilchrist, M. D. (2012). Replication of micro/nano-scale features by micro injection molding with a bulk metallic glass mold insert. *Journal of Micromechanics and Microengineering*, *22*(6).

Zhang, N., Srivastava, A., Kirwan, B., Byrne, R., Fang, F., Browne, D. J., Gilchrist, M. D. (2015). Manufacturing microstructured tool inserts for the production of polymeric microfluidic devices. *Journal of Micromechanics and Microengineering*, *25*(9), 095005.

Zhang, N., Srivastava, A. P., Browne, D. J., Gilchrist, M. D. (2016). Performance of nickel and bulk metallic glass as tool inserts for the microinjection molding of polymeric microfluidic devices. *Journal of Materials Processing Technology*, *231*, 288–300.

Zhang, P., Lin, L., Zang, D., Guo, X., & Liu, M. (2016). Designing Bioinspired Anti-Biofouling Surfaces based on a Superwettability Strategy. *Small*, *13*(4), 1–9.

Zhang, W., Ji, G., Bu, A., & Zhang, B. (2015). Corrosion and Tribological Behavior of ZrO2 Films Prepared on Stainless Steel Surface by the Sol-Gel Method. *ACS Applied Materials and Interfaces*, *7*(51), 28264–28272.

Zhao, N., Wang, Z., Cai, C., Shen, H., Liang, F., Wang, D., Xu, J. (2014). Bioinspired materials: from low to high dimensional structure. *Advanced Materials*, *26*(41), 6994–7017.

Zhao, Q., & Liu, Y. (2006). Modification of stainless steel surfaces by electroless Ni-P and small amount of PTFE to minimize bacterial adhesion. *Journal of Food Engineering*, *72*(3), 266–272.

Zhou, H., Chai, F., & Fang, J. (2016). Highly efficient colloid – solution deposition planarization of Hastelloy substrate for IBAD-MgO film. *Research on Chemical Intermediates*, *42*(5), 4751–4758.

Zouaghi, S., Six, T., Bellayer, S., Moradi, S., Hatzikiriakos, S. G., Dargent, T., Jimenez, M. (2017). Antifouling Biomimetic Liquid-Infused Stainless Steel: Application to Dairy Industrial Processing. *ACS Applied Materials and Interfaces*, *9*(31), 26565–26573.